UNIVERSITY OF OSLO
Department of Geosciences

Eddies in the Subarctic seas - on their characteristics and generation mechanism

Master thesis in Geosciences
Meteorology and oceanography

Marta Trodahl

15 June 2015

Abstract

The advent of satelitte observations revolutionalized Oceanography, an it has unveiled a turbulent ocean circulation dominated by mesoscale eddies (10-100km). Eddies represent an important aspect of the flow, and understanding them is essential to advance our perception of numerous ocean processes. Gaining knowledge of eddies generation mechanisms, evolution and impacts has been at the heart oceanographic research during the last decades. In this study we aim to investigate the characteristics of eddies in the Subarctic seas, and also to examine one of their generations mechanisms, baroclinic instability. Baroclinic instability has greatly aided our knowlegde of atmospheric eddies, and is also believed to the key advocator for eddies in the Ocean. We put forth the hypothesis that it can be held resposible for the large eddy acticity in th Subartctic Seas. To adress this issue we perform a linear stability analysis, that provide characteristics of the most unstable wave growing at the expense of an unstable background flow. The unstable wave's spatial and time scales are compared to the estimates of a simpler model (Eady) of baroclinic instability. An eddy census is conducted from a ten year model simulation. Coherent vortices are extracted from the flow and tracked in time. Characteristics such as size, vorticity, lifetimes are recorded and analyzed. The scales of the linear waves and nonlinearly evolving eddies from the detection scheme are then compared. We do not anticipate that local baroclinic instability can account for all aspects of a fully turbulent field, but to what a degree it appears to be active in the initial stages of the eddies, is still possible to be traced.

Acknowledgements

I would like to start by expressing a huge gratitude to my main supervisor, Pål Erik Isachsen. Thank you for an interesting, and challenging journey, with several unforeseen turns. I have learned so much through your great guidance and knowlegde, and not the least, through all your patience along the way and for always taking time to answer any of my questions.

Great thanks to my co-supervisor, Lars Petter Røed for always freely sharing your enthusiasm and 'vast ocean' of knowledge whenever I came knocking on your door. I learned something new and exiting every time I did!

A special 'thank you' to Anne Claire Fouilloux, who has guided me through the Fortran jungle, and helped entangle every issue that seemed unmountable. I never thought such obstacles could turn out to be fun to figure out! You're the best!

I am forever grateful for Mari and Helle, and the friendship we have shared throughout these two years. Thanks for all the support and care, for all the great conversations, both about our subjects but also for sharing your lives. This journey would not have been the same without you two! Thanks to Henrik, Helle and Eivind for the good times we have had together at Metos. And, thanks Kristoffer, for all the interesting conversations and exampreparations we've shared. You have taught me a great deal!

Most of all, I would like to thank Ester, Stina and the girls back home! Thanks for always being so caring and 'cheering me on'.

Contents

1 Introduction **7**
- 1.1 Macroturbulence in the ocean . . . 7
- 1.2 Baroclinic instability . . . 9
- 1.3 Ocean circulation and eddies at high northern latitudes . . . 12
- 1.4 This study's contribution . . . 16

2 Our model 'data' **19**
- 2.1 The ROMS model . . . 19
- 2.2 The Arctic hindcast . . . 21
- 2.3 Comparison with observations . . . 22

3 Linear stability analysis **27**
- 3.1 Baroclinic instability explained . . . 27
  - 3.1.1 The basic mechanism . . . 27
- 3.2 The linearized problem . . . 29
- 3.3 Theory . . . 29
  - 3.3.1 The eigenvalue problem . . . 31
  - 3.3.2 Generalized QGPV . . . 33
  - 3.3.3 Neccesary conditions for instability . . . 33
  - 3.3.4 Stability in the N-layered case . . . 35
  - 3.3.5 Eady growthrate and lengthscale . . . 35
  - 3.3.6 Energy transfer . . . 37
- 3.4 Discretization and numerics . . . 37
  - 3.4.1 Discretizating . . . 37
  - 3.4.2 Numerics . . . 38
- 3.5 Results from the linear stability analysis . . . 38
  - 3.5.1 Growth rates of the most unstable wave . . . 39
  - 3.5.2 Lengthscales of the most unstable wave . . . 40
  - 3.5.3 Comparison with the Eady prediction . . . 42
  - 3.5.4 A closer look at the eigenvectors . . . 45

4 Statistics of the fully turbulent field **49**
- 4.1 Autmatized eddy detection . . . 50
- 4.2 Previous studies . . . 51
  - 4.2.1 Physically based methods . . . 52
  - 4.2.2 Geometrically based method . . . 53
- 4.3 A hybrid eddy detection method . . . 54
- 4.4 Results . . . 58

4.4.1 Geographical eddy density . . . 58
4.4.2 Eddy kinetic energy . . . 59
4.4.3 Eddy radius . . . 61
4.4.4 Cyclones versus anticyclones . . . 64
4.4.5 Eddy lifetimes . . . 69
4.4.6 Generation and termination of eddy trajectories . . . 70
4.4.7 Energy transfer . . . 72

5 Summary and discussion **75**
5.1 Summary . . . 75
5.2 Our results in light of previous studies . . . 75
5.2.1 Characteristics inferred from linear stability analysis . . . 75
5.2.2 'Observed' eddy characteristics . . . 80
5.3 The usefullness of the linear prediction . . . 83

Chapter 1

Introduction

> *The ocean is literally a sea full of eddies*
>
> Robinson, *1984*

1.1 Macroturbulence in the ocean

Our current understanding of the ocean has developed immensely during the last decades[1]. The emergence of satellite altimetry in the early 1990s marked the onset of a revolution in oceanography (Le Traon, 2013). Technical advances now provided the means of retrieving highly accurate large scale ocean observations from space. Global maps of sea surface height measurements yielded several new discoveries. It was revealed that the ocean circulation was infested by mesoscale variability. An abundance of mesoscale features, on the scale of 10-100 km, was observed throughout the world's ocean. This served to confirm similar, scattered findings from regional field programs in the 1970s (Chelton et al., 2011).

In 1909, Helland and Hansen described 'some puzzling waves' observed in hydrography from the Norwegian Sea. On the basis of their findings, they stated that: *"The knowledge of the exact nature and causes of these 'waves' and their movement would, in our opinion, be of signal importance to Oceanography, and as far as we can see, it is one of its greatest problems that most urgently calls for a solution."* It was not until 50 years later, ocean observational analysis gave proof that large parts of the ocean was populated by such waves, or eddies. Up until the early 1960s the general ocean circulation was perceived to be relatively steady, dominated by mean currents that are subject to little variability. Except for the known changes in surface currents brought by the variations in wind forcing, the deeper layers were believed to entail slow, and sluggish movements. This perception was later disproved (Crease, 1962). Knowledge about atmospheric weather systems, was well established at the time. However, the idea that the ocean possessed dynamically equivalent features, had still not surfaced. Just like the atmosphere, the ocean was later found to be filled with cyclones, anticyclones (low and high pressure systems) and fronts. Weather occurs in the ocean as well, and it should prove to be an essential ingredient in energy and tracer budgets. In fact, mesoscale eddies account for the peak of the oceanic kinetic energy spectrum (Chelton et al., 2007). Thus, eddies impacts the general circulation fundamentally.

The abundance of eddies in the ocean, brings with it a splendor of consequences on both large and small

[1] This introductory section is influenced by chapter 4 in Barton (1997)

scales. The ocean acts according to equilibrium balances, and the eddies contribute to uphold these balances through the supply of essential dynamical and material fluxes (Mcwilliams, 2008). The eddies transport momentum, and also large bodies of water, and consequently assist in the distribution of watermass characteristics (Gent et al., 1995). Fluid can get trapped inside the rotating core of the eddy. It may then be carried far from its generation region, and supply distant ambient waters with other characteristics (Wunsch, 1999). A considerable amount of heat and salt fluxes arise as consequences of eddies, making them carriers of so called active tracers(tracers that can affect the ocean's density). Additionally, eddies impact distributions of passive tracers, such as nutrients and vorticity (Griffies, 2004). Generally, the eddies aid in stirring these scalars properties (Griffies, 2004), but they also act to mix them. The latter, acts to reduce spatial gradients. Rather than a reversible transport, the mixing irreversibly homogenize tracer distributions.

Studying ocean eddies is a challenging task for several reasons. The largest limiting factor in the observational sampling of the eddy field. Though dynamically analogous, the atmospheric and oceanic weather systems are comprised by eddies of incompatible characteristics. The length scale of atmospheric eddies occurs at what is called the synoptic scale, which is on the order of 100-1000km in the atmosphere (Røed 2012). On the other hand, oceanic eddies occur on the order of 10-100 km. From a dynamical perspective, this could rightfully have been referred to as the ocean's synoptic scale (Røed 2012), in that it signifies motions governed by a low Rossby number[2] However, the storms in the ocean have rather been given the term mesoscale eddies, reflecting their spatial scales (Robinson et al., 1988).

Consequently, a prerequisite for investigating oceanic eddies is high resolution spatial data. Additionally, ocean eddies have substantially longer lifetimes than their atmospheric counterparts. The atmospheric storms have timescales of days to a week, while oceanic storms may evolve on timescales of weeks to months or to the most extreme, even years. So, ocean eddies are easier to capture from a timescale perspective, however, this relies on the capacity of the available observational technology.

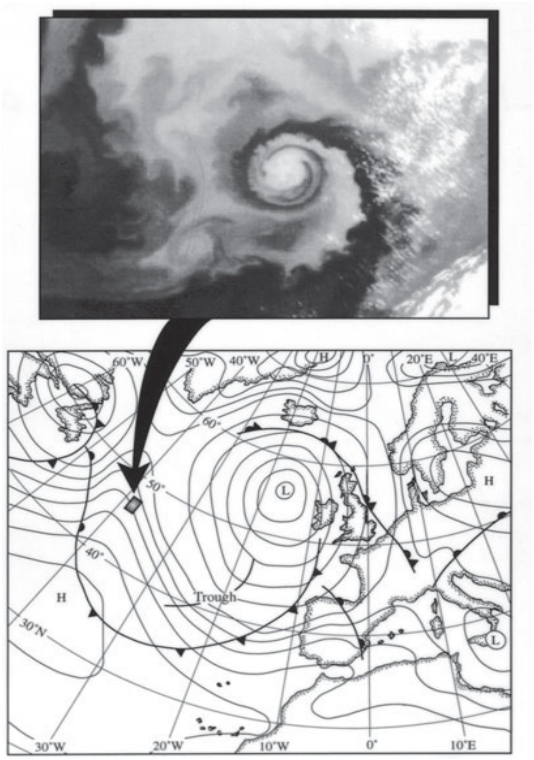

Figure 1.1: An illustration of two dynamical counterparts of vastly different spatial scales. An atmospheric low-pressure system is located west of Ireland, and the 'zoomed-in' area depict an oceanic cyclonic(counter-clockwise rotating) eddy, detected by a satelitte image of ocean temperature (Barton, 1997).

Such datase ts have not been attainable until recent years. Prior to the 50s and 60s, it had been nearly impossible to assemble a sufficient amount of measurements at the ocean surface, yet alone getting qualitative measurements below the surface. Through observations gathered by newly invented floats (John Swallow), deep currents were unveiled which possessed velocities comparable to moderate surface-currents. Following these findings, new regional investigations were conducted at the be-

[2]The Rossby number, U/fL, compares the flow's acceleration with the Coriolis force, and represents the ratio between the Earth's rotation time, $1/f$, and the flow's advective time scale L/U. It is a measure of the validity of the geostrophic approximation (Holton, 1973).

ginning of the 1970s and onward, amongst them the Mid Ocean Dynamics Experiment (MODE; 1971-1974), POLYGON (1970), and the Marginal Ice Zone Experiment (MIZEX; 1980s). A new era of exploration began, and the 70s have often been accredited as the "decade of the mecoscale" (LaTraon 2013). These investigations started to uncover the truth about the smaller scale ocean, and its turbulent nature.

In both the atmosphere and ocean, the large scales are strongly affected by the earth's rotation and a stable stratification. A balanced mean state in the horizontal is maintained between the earth's rotation and horizontal pressure gradients (geostrophic balance). Additionally, the vertical pressure gradient is balanced by the gravitational force (hydrostatic balance). These balances combined yield a thermal wind flow, which express the vertical shear of geostrophic currents. These motions are to a large degree confined to the horizontal plane, with much weaker vertical velocities. Thereby, the 'turbulence' at these scales is not isotropic as in 3D turbulence, but rather quasi-two dimensional. This kind of turbulence has been called geostrophic turbulence, due to the flow's near geostrophic balance, and *macroturbulence* signifying the large spatial extent of the flow (Vallis, 2006).

The slowly-varying large-scale ocean currents are often called the background ocean circulation. This background flow is often unstable to perturbations, and when instability occurs, smaller scale features spontaneously appear. At first, these features might initially evolve linearly in isolation, but as they grow, nonlinear effects facilitate interactions on a large range of scales (Vallis, 2006). Fluid parcels are merged, stretched, strained and rotated. From the chaotic and unpredictable nature of turbulence, one then might anticipate a disorganized flow field with no structure. However, an essential characteristic of this so-called 'macroturbulence' is the presence of rotating coherent vortices (Mcwilliams 1990). Studies have found such features, spontaneously emerging in all environments dominated by rotating, advective dynamics (Mcwilliams, 1990; Venaille et al., 2011). The distribution of vorticity(rotation) and strain in such flows is not arbitrary. Subtly, the flow organizes into coherent vortices with concentrated vorticity and energy, enclosed by regions of strain. In an early study of coherent vorticies McWilliams (1990) expresses: *"One can marvel at this manifestation of 'order within disorder' and be fascinated both by the beauty of the patterns and by the challenge such a phenomenon presents to dynamical theory."* Since the vortices make up an essential part of the flow, it is highly desirable to characterize their properties, and in some ways predict their generation mechanisms, evolution and impacts. A characterization of eddies is truly a demanding and challenging task. Gaining knowledge of eddies' life cycles and impacts has been at the heart oceanographic research during the last decades. Still, there is no theory accounting for their structure and statistics that is universally accepted (Venaille et al., 2011). Some of the questions that are still subject to intense research, and important to answer is: What advocates the existence of these features? What characteristics do the eddies take on as they evolve in time? What sets their equilibrated length scales, magnitudes and structures?

1.2 Baroclinic instability

Baroclinic instability represent a fundamental process in nature that applies for fluid motions affected by the earth's rotation. Horizontal density gradients act to set up a vertically sheared flow supported by tilted density surfaces (isopycnals). The nature's respond to these gradients is to attempt to reduce them. Via baroclinic instability, some of the potential energy stored in the tilted isopycnals is extracted, and converted it into kinetic energy which further feeds the process (Vallis 2006). The most familiar example of this process is probably the atmospheric jetstreams, highly susceptible to this kind of instability. Heating at low latitudes, and cooling at high latitudes, make isotherms slant

upwards toward the poles. This temperature difference induce a vertically sheared zonal flow, in thermal wind balance, which is the source for the jetstream. Eddies arise from the instability of the mean flow, and by transpoting heat poleward, they serve to diminish the equator-to-pole temperature gradients which otherwise would be very steep.

The theory of baroclinic instability has been indispensable for our understanding of eddies in the atmosphere and has also been suggested by many to be the primary underlying process for the production of the oceanic eddies (Gill et al., 1974; Pedlosky, 1982). This assumption is related to the amount of available kinetic energy compared to available potential energy. Gill et al. (1974) observed that locations of high eddy activity often occured where there were steep isopycnal slopes. Based on an energy analysis, they showed that the amount of available potential energy (APE) stored in the tilted isopycnals, exceeds the amount of kinetic energy available in the large-scale circulation by about a factor of 1000. They thereby argued that most oceanic eddies likely originate from baroclinic instability.

A common approach for investigating this claim is to compare characteristic space and time scales of baroclinic instability with actual observations or from model 'observations' (Smith, 2007; Tulloch et al., 2011). A way to obtain these properties is through linear baroclinic instability theory. If the properties from the linear predictions are found comparable to the observations, they can be used to characterize the observed field. GGS also computed growth rates from idealized linear stability analysis, and found them crudely close to the actual observed rates. Other studies have found a correlation between turbulent timescales, and growthrates provided by linear theory (Wunsch and Stammer, 1997; Chelton et al., 2007). A similar relationship between length scales of a fully nonlinear field and linear predictions have not been as successful.

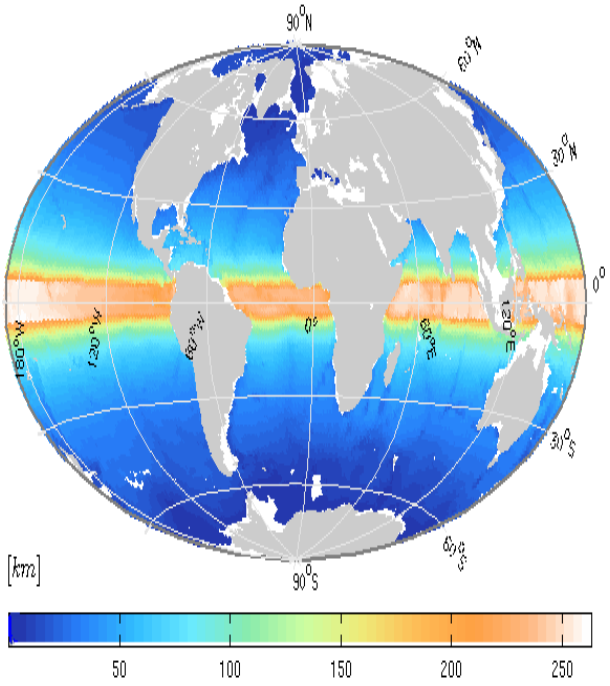

Figure 1.2: Global distribution of the Rossby deformation radius. Reproduced by Chelton's data from 1998 (data available at http://www-po.coas.oregonstate.edu/research/po/research/rossby_radius/).

Idealized models of baroclinic instability predict eddy length scales near the Rossby deformation radius,L_d. In the simplest model, known as the Eady model (Eady, 1949), L_d is the lengthscale of the fastest growing unstable wave. Hence, this is perceived as the canonical horizontal lengthscale for mesoscale features. This lengthscale signifies the competing effects of stratification and rotation, and is the scale where these two forces become commensurable (Thorpe, 2005). It varies considerably with latitude, and also is highly dependent on the fluid depth. Figure 1.2 show the L_d computed from a global climatological atlas, provided by (Chelton et al., 1998).

Assessing the relationship between observed eddy scales and L_d has been a focus of numerous studies (Wunsch and Stammer, 1997; Stammer et al., 2002; Le Traon et al., 1990; Le Traon and Minster, 1993). LaTraon et al. (1990) and Stammer and Boning (1992), reported strong geographical variations in eddy spatial scales from satelitte observations, and tied this to the variations in the L_d. They suggested

a linear relationship between the two lengthscales. Stammer(1997) found that zonally averaged eddy scales were larger than the L_d, but still linearly related. Prior to this, LaTraon (1993) had observed that eddy scales dropped by a factor of two, and L_d by a factor of 4, toward higher latitudes.

It is not obvious that the predictions from linear theory should be correlated with the length scales characterizing the nonlinear eddy field. Several studies have been inconclusive about the issue (Venaille et al., 2011, Vollmer and Eden 2013), and observations often deviate substantially from the linear predictions. As the turbulent interactions start to occur, the field evolves and the initial characteristics are modified. Eddy sizes seem most often to be larger than L_d, and the linear relationship is found by zonal averages, which neglects the details in the geographical distribution.

An important issue is the question of how the system's inherent energy is transferred across different length-scales[3]. The spectrum of sizes is bounded between two extremes. The flow will experience forcing at some larger scale, which sets the upper bound. In the ocean, the dominant large-scale forcing is supported by the sun and wind injecting heat and motion respectively into the upper layers, and by tides affecting entire water columns. Consequently, the system is continuously replenished with energy. The lower end of the size-spectrum, is set by the scales where molecular viscosity eventually kicks in to dissipate the energy into heat.

If one assume that energy is perpetually introduced at large scales, how then is an equilibrium attained? Kolmogorov showed that in 3D turbulence, there is a continous energy flux from larger to smaller scales. The general picture granted by 3D turbulence is a largescale flow which is unstable to smaller scale eddies. The eddies grow, and breaks up into succesively smaller eddies. The kinetic energy is thereby carried downscale, up until the eddies get affected by viscocity and dissipate into heat (Vallis 2006).

Processes on these scales are not effected by rotation, and thereby do not entail the balanced states exhibited on much larger scales (McWilliams 2008). 2D turbulence theory has also served as a platform for studying the evolution of energyflux, due to its analogue to geostrophic turbulence.
Figure 1.3 illustrates the classical view of energy transfer in 2D, similar in geostrophic turbulence (Vallis 2006)

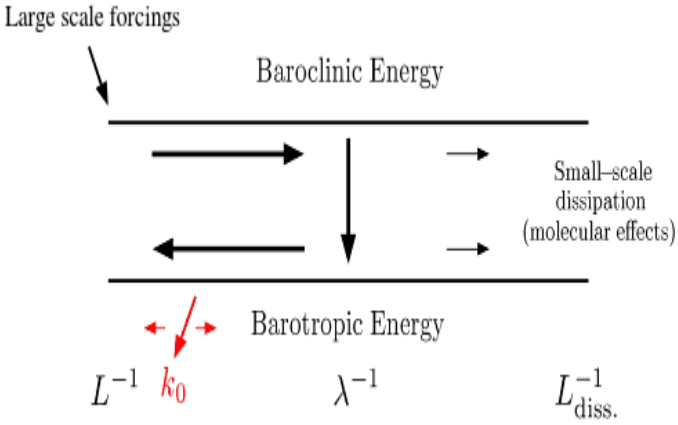

Figure 1.3: The 'dual' cacade of energy in geostrophical turbulence.

In figure 1.3, baroclinic energy is assumed supplied by large scale forcings (solar heating, tidal motions, winds), and energy transverses down toward L_d (denoted in the figure as the invers wavenumber, λ^{-1}). At scales of about L_d, energy is transferred into the barotropic mode by eddies, and from there it cascades *upscale*, aided by nonlinear interactions occuring across scales. Nonlinearity becomes important as soon as the wave grows to an amplitude which cannot be considered minor relative to the mean flow (Hoskins and Simmons, 1978). The nonlinear terms neglected in linear predictions then becomes significant. The eddies undergo a so-called barotropization, and the energy is eventually taken out by large-scale dissipation such as bottom friction (Held and Larichev, 1996). We see that most of the energy joins in this inverse cascade, albeit some of the energy also goes to smaller scales.

Estimated eddy length scales from observations have promoted the possibility of an inverse cascade

[3]The rest of this section is strongly influenced by Chapter 8 and 9 in Vallis (2006)

in the ocean (Scott and Wang, 2005). Observed eddy scales are, as previously noted, typically found to be larger than the scale at which they initially emerge, presumably around L_d (Smith 2007; Tulloch et al. 2011). The source of this gap between the predictions from linear theory and observations is commonly attributed to a turbulent inverse cascade (Smith 2007). Scott and Wang (2005) presented, for the first time, observational evidence for such a cascade in the ocean from satelitte retrievals. Their findings challenges the classical view of the inverse cascade, by suggesting that it occurs mainly in the baroclinic mode. Nonetheless, an energy cascade toward larger scales provide an explanation for the discrepancies between linear thoery and observations. Studies that incorporate non-linear effects in baroclinic growth have implied the existence of such a cascade, yield much greater scales than linear growth. Smith (2007) states that, *"...a nonlinear cascade of energy seems necessary to explain the observed eddy statistics."*

k_0 in figure 1.3 denote the wave number at which the inverse cascade reaches. This upper limit, where the cascade is referred to as 'arrested', is a an unclear issue. Scott and Wang (2005) describe the arrest as mysterious. We will not venture into this topic, but merely reinforce that a comparison between linear predictions and a statistical fully nonlinear field is not anticipated to be trivial. Koszalka et al. (2009) remarked that *"One question that remains open is the limits and range of applicability of the results obtained with simpler 2-D and QG models of ocean mesoscale turbulence."* Our main incentive in this study will be look into this question. Initially, we will approach this question by the means of a linear stability analysis, yielding unstable wave properties. Thenceforth, we examine the comparability between these properties and eddy characteristics from the fully turbulent field, by implementing an eddy detection algorithm.

Prior to our analysis, it is apt to take a look at the main elements of the circulation in our study domain. In the following section, we thereby revise the mean circulation, and mention some of the mesoscale variability observed in the different regions.

1.3 Ocean circulation and eddies at high northern latitudes

The area of the Arctic Ocean and it's surrounding Seas amount to a small fraction of the Earth's area. The significance of these regions in regards to the global climate is however huge. The interchange of watermasses between them is claimed to be the *"most dramatic water mass conversions in the world's oceans"* (Beszczynska-Moller et al., 2012). The polar and subpolar regions thus serve as important moderators of our climate. Relatively warm water, saline originating in the North Atlantic (and North Pacific) are brougth up to higher latitudes. Atlantic Water is carried through the Nordic Seas into the Barents Sea and the Arctic Ocean. Simultaneously, colder, fresher surface-water runs southward out of the Arctic, along the Greenland coast. At depth, an overflow of dense deepwater is present, and another overflow also occurs on the east side of Iceland, both destined equatorward. This export contains a large portion of the Arctic Ocean's freshwater supply from precipitation and river runoff, as well as transformed AW. Upon leaving the high latitudes, the Atlantic Watermass has been subject to a tremendous transformation (McCartney and Mauritzen, 2001). During the transformation, both the fresh, cold shallow waters and ice are produced, as well as dense, saline deep waters (Beszczynska-Moller et al., 2012). Consequently, the area we are studying here is of huge importance to the ocean's density-driven circulation. The earlier perception that watermass transformations took place merely at a few particular locations, i.e. in the Greenland and Labrador Sea, is now claimed to also happen along the inflowing branches of warm waters (Isachsen et al., 2007). Eddies are believed to be present along all the segments and participate actively in several of the transformation processes. (Lilly et al., 2003).

We will now look into the key features of the circulation in our study area. Figure depict the main Seas, basins and ridges, and figure 1.5 entails the major elements of the circulation.

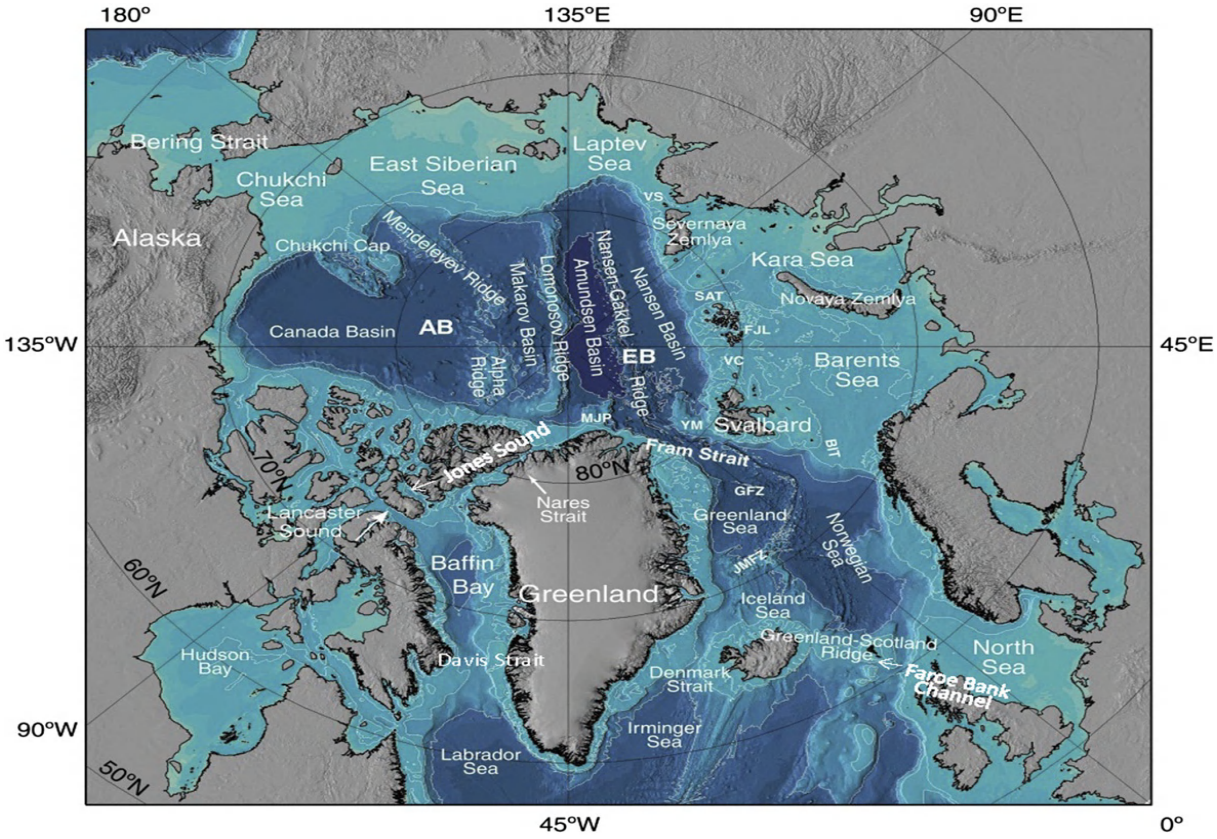

Figure 1.4: Arctic ocean and neighboring seas. Blue colors represent the bottom-depth, darker colors deote deeper waters. We note the shallow straits, Barents Sea, the shelf seas in contrast to the steep declines basinward. Topography exerts a major control on the circulation in this domain.

Temperate, saline Atlantic Water (AW) enters the Subarctic Seas mainly through three branches (McCartney and Mauritzen, 2001). A large branch of the North Atlantic Current, formerly constituting the Gulf Stream, splits up as it flows over the mid-Atlantic Ridge. It is largely introduced to the Nordic Seas via the Faroe Channels inflow. It finds its way polewards on each side of the Faroe Islands, between Iceland and Scotland, and on the west side of Iceland (Beszczynska-Moller et al. (2012). Having passed the Greenland.Scotland Ridge, the NAC is deemed the Norwegian Atlantic Current.

The AW is carried northward along the Norwegian coast in several branches, tens of kilometer wide (Rodinov 2003). The NwAC has a two-branch structure that follow the topography (Poulain et al., 1996). The part furthest west is an extension of the Faroe Current, which follows the 2000m isobath, and becomes particularly evident as it flows along the Vøring Plateau. Most of this water flows northwest into the Greenland Basin, while some continues to follow the isobath, and turns northeast into the Lofoten Basin (Rodionov et al.,2003).

The AW flowing along the slope between Faroe and Shetland continues north along the Norwegian continental slope. Paralell to the two NwAC branches is a third northbound current, the Norwegian Coastal Current (NCC). The NCC is buoyancy-driven, and contains Norwegian Coastal waters formed by freshwater runoff and the Baltic (Orvik et al., 2001). Mixing between the saline Atlantic Water, the low-saline coastal water and the North Sea watermass occurs, which act to reduce the AW signature.

These currents supplement two major frontal zones, the North Polar Frontal Zone(NPZF) situated at the Mohn Ridge and the Norwegian Coastal Current frontal zone (Rodionov et al., 2003). The former seperates the colder, fresher waters residing on the

west side of the Nordic Seas, and the warm inflow of AW on the east side. The latter seperates the fresher coastal waters from the saline AW. These fronts frequently depart from their mean positions, and exhibit large meanders. The potential energy associated with the frontal zones is a strong advocator for mesoscale eddies (Poulain et al., 1996). Between the NwAC branches, there is a wide belt of highly variable flow, has been called 'the zone of intermittence', often heavily populated by eddy structures (Rodionov et al.,2003). Some of the eddies originating along the coast are advected with the mean flow, but a considerable amount is also believed to escape the current and propagate seaward. A large,persistent anticyclone in the Lofoten basin show up in decadal-long mean fields. Several studies have concluded that its climatic nature is due to smaller anticyclonic eddies departing from the NCC, merging with it, and recurrently providing new energy for its survival (Sø iland and Rossby, 2013) The seaward destined eddies are suspected to be responsible for a lot of the cross-shelf heat-exchange (Straneo 2015). They thereby supply the colder waters offshore with heat, and warmer shelf-waters with cold, nutrition-rich water.

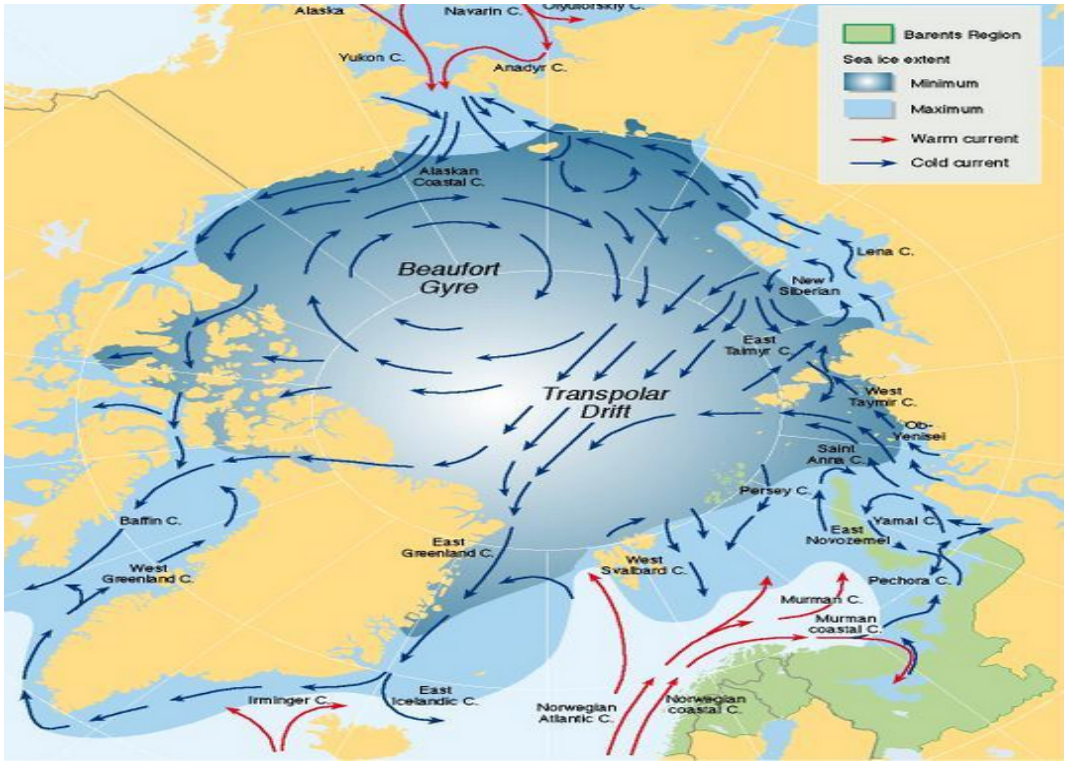

Figure 1.5: The general circulation in the study domain. The dark and ligth blue colors denote a minimum and a maximum sea-ice cover, repsectively. The color of the arrows denote cold (blue) and warm (red) currents.

Cyclonic large-scale gyres that are tied to the local topography exist in 4 regions of the Nordic Seas (Poulain et al., 1996a). The gyres are centrally located in the Greenland, Norwegian and Lofoten Basins, and near the Icelandic Plateau. They all entail a mean circulation, that mainly follows the topography (Nø st and Isachsen, 2003)

North of the Lofoten Basin, one part of the NwAC is steered toward the Fram Strait by the curve of the shelf-edge, as the West-Spitsbergen Current (Beszczynska-Moller et al., 2012). The other branch continues its path along the coast, parallell to the NCC, and enters the Barents Sea as the North Cape Current.

The Barents Sea is a shallow sea with a partial sea-ice extent, and devoid extensive river run-offs supplying fresher waters. There are periods of salinity-changes still, provided by ice-melting supplementing the Sea with fresh water, while occurrences of freezing makes the waters more saline. A large portion of the northernmost NwAC ventures into the Barents Sea, bringing temperate and saline AW. The Polar Front here, seperats the southern warm,salty waters from the cold, fresh Polar Water. The AW is further modified by commodious cooling from air-sea interactions, and thereby aquires a higher density. As AW departs the Barents Sea, primarily through the St.Anna through, it has been cooled to about 0° (Beszczynska-Moller et al., 2012). It does therefore not contribute much to heat to the Arctic Ocean.

The AW's major gateway and exit region to the Arctic is however the Fram Strait (Mauritzen, 2012). At the inflow the AW dives under the ice-cover as it ventures into the Arctic Ocean. The waters have not been cooled as much as in the Barents Sea, and is still relatively warm upon its arrival. Some of this AW recirulates, and again, sinks beneath the lighter Polar Water(PW) at the surface, and joins the East Greenland Current (EGC) south. A former perception was that both these sinking episodes occurred smoothly, but it seems rather to be a pumping phenomena realized by baroclinic eddies (Isachsen (2015)). Eddies shed from the WSC, translating westward in the Fram Strait are found in several studies (Johannessen et al., 1987). This suggests that a large fraction of the recirculating Atlantic water is comprised of eddies.

The part of the AW continuing into the Arctic Ocean, then constitutes a rim current, the Arctic Ocean Boundary Current(AOBC). Initially it flows cyclonically along the boundary of the deep Eurasia Basin (denoted as EB in fig.). The current separates into two major parts as it reaches the Lomonosov Ridge (Woodgate, R. A., K. Aagaard, R. D. Muench, J. Gunn, G. Bjork, B. Rudels, A. T. Roach and Schauer, 2001). One branch follows the ridge toward the Fram Strait again, and the other further continues its journey deep into the Arctic Ocean by entering the Marakov Basin. As observations are limited, the rest of the AW's circulation is a bit more uncertain. However, it is believed to flow around the Chucki cap and flow cyclonically along the rim of the Canada Basin. The upper layers in the Arctic there are characterized by the fresher Pacific Water (PW). PW enters through the Bering Strait, and is carried into the Arctic by several processes happening in the Chucki Shelf Sea. It takes part in the large anticyclonic Beaufort gyre, and is carried to its final destination, by the transpolar drift cutting across the Arctic Ocean. Some of the PW also exits through the Canadian Archipelago. Eddies have frequently been observed in the Canada Basin (Timmermans, Timmermans). Some believe these eddies originate mostly from the Chucki Seas, and from there propagate basinward.

A large volume of both PW and AW then exits the Arctic Ocean via the Fram Strait. A lot of this outflow joins the southward flowing EGC. An ice-cover resides along the coast throughout the year, and the border between the edge of ice-covered water and the open water is called the Marginal Ice Zone (MIZ hereafter) (Horn, 1987). The MIZ thereby consists of a transition from open ocean to pack ice. Eddies are often observed near the MIZ here, and interactions commonly occur between eddies and the ice-edge (Horn, 1987). Eddies might advect, melt or break up sea-ice, and generally make Arctic water and AW converge (Ikeda et al., 1989). The EGC enters the Irminger Sea which covers a transition zone between warm, saline AW and cold, fresh PW. The current carry the warmer waters from the south, most of the western branch turns cyclonically at 65° and merges with the EGC along the coast of Greenland (Cuny et al., 2002). The EGC then enters the Labrador Sea, which lies between Canada and the south-western part of Greenland (Lilly et al., 2003), and becomes the West Greenland Current (WGC). The WGC is a part of the strong cyclonic boundary-current system encirculating the basin (Lavender, 2000). The WGC merges with the Labrador Current when it reaches the Canadian coast.

This basin is responsible for an essential component of the North Atlantic overturning circulation, i.e. the formation of upper North-Atlantic deep-water (Lilly et al. 2003). Winter-convection homogenize

a large patch of water which can get over 2 km deep. This allows the sinking of cold, fresh water (Marshall and Schott, 1999) that is distributed out at middepth. The Labrador Sea hosts three particular types of eddies distinguished according to their characteristics, the Irminger Rings or Irminger Current Anticyclones, Irminger Current Cyclones and convectively formed anticyclones (Lilly 2003). The convective eddies (CEs) are believed play a major role in the restratification process after the convection (Femke de Jong,Furey, Heather H., M. Valdes, James R.Bower, 2013).

1.4 This study's contribution

This study aims to contribute to the present knowledge of eddies in the SubArctic Seas, and to investigate a potentially dominant eddy-generating mechanism, namely baroclinic instability. Many studies have focused on particular regions of this domain, but it is to the author's knowlegde no eddy census study encompassing the entire domain.

Our goals are to test the hypothesis that baroclinic instability accounts for most of the eddy activity in the study region. We relate the eddy length and time scales provided by linear predictions with statistics of the fully-developed macroturbulent field. Initially we perform a linear stability analysis on mean fields from a 10 year model simulation. The normal mode computation is done following the procedure of Smith (2007). The analysis yield characteristics of baroclinically unstable waves. The most unstable mode will be the wave emerging first in an unstable mean state, and is believed to continue to dominate with time. We will discuss the growth rates and associated length scales of fastest growing waves. Furthermore the most pronounced growth regions are identified and we see whether simple Eady dynamics can act account for the growth we see, or if more complexs dynamics is needed to be invoked. The linear theory is valid only in the initial stages of growth when the perturbed amplitudes are small. As the waves grow, nonlinear processes take over the evolution. The statistics of the fully turbulent field is obtained by implementing an eddy detection procedure, and recording the characteristics of the identified eddies.

The quasigeostrophic setting is utilized in the linear analysis, which is valid for length scales near L_d and a low Rossby number. Since the ocean models utilize the full (hydrostatic) primitive equations, there exists a gap between the idealized quasigeostrophic predictions and the numerical simulations. Observations and model simulations indicate that the equilibrated scales differ substantially from Ld, being larger at high latitudes and smaller at low latitudes. It is beneficial to further examine this issue, and look for potential discrepancies or resemblances between the these two scale estimates.

Many parameterization schemes of eddy transport in climate models, builds on the notion that eddies originate via baroclinic instability. Specifically, the parameterizations rely on the characteristics of the most unstable wave in the simplest model of this process, the Eady model. The Eady model does not take into account the influence of topography or changes in the Coriolis force, β. Still, it is a common to use since it is easy to implement numerically with a low computational cost. Mesoscale eddy scales vary strongly with latitude, reaching 200km at the equator plunging to 5-10km in the polar- and subpolar regions. Hence, this put a constraint on the horizontal grid-spacing in a model in order to represent them. Any deficienies in coarse model parameterizations is thereby most alarming at high latitudes, and it is likely that instabilities in these regions are more dependent on topography than β (Isachsen et al., 2003; Nøst and Isachsen, 2003). By comparing the Eady growthrate with the growthrate from a full linear stability analysis, we can point to possible shortcomings in the Eady model. The Eady model has been reported to produce reasonable rates (Smith 2007), however, it does neglect important dynamical aspects. It is highly desireable to not only get corrects values, but to attain them

for the right reasons. We therefore inspect the linear stability analysis at some locations in detail, to see whether the results there resemble an "Eady-type" instability.

There are ambigious issues related to the pre-processing of raw altimetry data. Chelton (2011) remark that the smoothing applied when gridding the data, leaves out features which are smaller than roughly 40 km. As a result, the amplitude of smaller-scaled eddies is strongly reduced (Jong et al., 2013). This is especially a concern for studies at high latitudes. Jong et al (2013) compared observations of eddies in the Labrador sea from mooring measurements, with the maps of SLA used in Chelton et al. (2011). On only one occasion, did an eddy-track in the altimetry dataset approximately match the location of the mooring. However, this track was found 16 km away form the mooring, and the timing did not agree with any of the 33 eddies observed at the mooring. Neither did the properties of this eddy have typical values, with a radius of 60km, an amplitude of 5 cm, and a rotational velocity of 10 cm/s. Jong et al. (2013) report that the estimated eddy-characteristics in the Labrador Sea made by Chelton et al.(2011), do not compare well to what is inferred by observational studies. A similar comparison was made by (Prater, 2002). In this study data from unfiltered along-track altimetry, with a resolution of 7 km, and estimates of SLA from floats were juxtaposed. Again, only one eddy in the satelitte observations had a corresponding track as the eddies tracked by floats. These results imply that altimetry data is not apt for studies in Polar regions.

The basis for utilizing a model simulation in this study, instead of for instance satelitte data, is grounded in several reasons. The model provides closely gridded datapoints, and complete spatial and temporal coverage. Utilizing model thus meets the need for data with a relative high resolution.

Chapter 2

Our model 'data'

2.1 The ROMS model

In this study we analyze data from a Regional Ocean Modeling System (ROMS; (Haidvogel and Beckmann, 1999; Shchepetkin and McWilliams, 2005) hindcast run. Figure 2.1 depict the model domain. Shown the depth averaged 10 year mean velocity field (the magnitude).

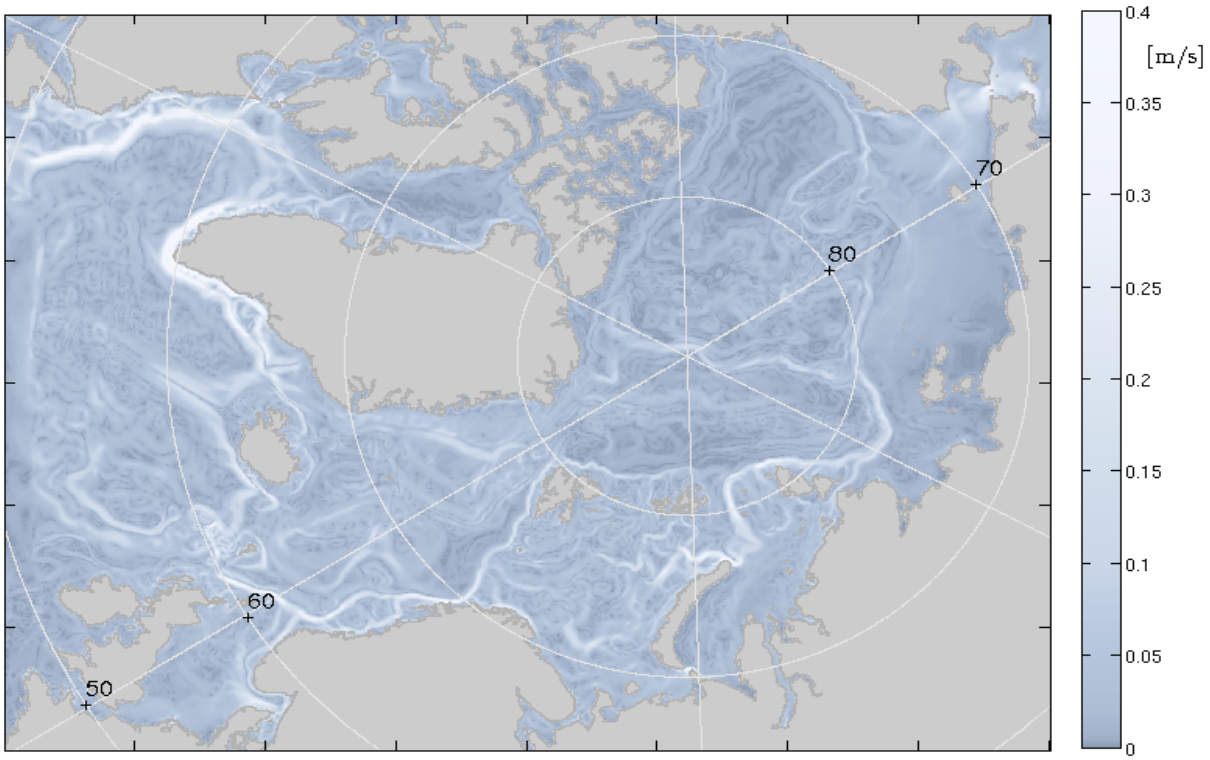

Figure 2.1: Study domain with superimposed 10 year mean, depth averaged velocities.

ROMS is a 3D, free-surface, state-of-the-art ocean model. The ROMS-code is open-source code. The model relies mainly on Fortan90-code for the computation. A terrain-following σ-coordinate is used

in the vertical, expressed as

$$\sigma = \frac{z-\eta}{H+\eta},\ -1 \leq \sigma \leq 0,$$

where the depth at the bottom is denoted by z=-H(x,y), and $\eta(x,y)$. Some of the merits with this coordinate is that it smoothly overlays the bathymetry and can be stretched to attain better resolution in areas needed.

The governing equations for the ocean dynamics and thermodynamics are non-linear differential equations[1]. There are 7 unknown parameters needed to be solved for in order to have a closed system. The model solves a set of mean field primitive equations under a Boussinesq approximation. The horizontal momentum equations take the form:

$$\partial_t \mathbf{u} + \mathbf{u} \cdot \bigtriangledown_h \mathbf{u} + f\mathbf{k} \times \mathbf{u} \ = -\frac{1}{\rho_0} \bigtriangledown_h p - \frac{1}{\rho_0}\frac{\partial \tau}{\partial z} - \bigtriangledown_h \cdot \boldsymbol{\mathcal{F}}_h, \tag{2.1}$$

where $\mathbf{u}$, are the horizontal velocity components, and $\bigtriangledown_h = (\partial_x, \partial_y)$. The first term signifies acceleration of velocities in the horizontal directions. $f\mathbf{k} \times \mathbf{v}$ is the vertical component of Coriolis force, which arise from the Earth rotating around its own axis. $f = 2\omega \sin \Phi$, where ω is the Earth's rotation rate, and Φ the latitude. τ signifies the vertical mixing of momentum, and $\boldsymbol{\mathcal{F}}_h$ denotes the horizontal mixing of momentum.

Furthermore, the model is based on the assumption of a hydrostatic balance in the vertical. Assuming that there exist a dominant balance between the pressure gradient and buoyancy reduces the vertical momentum equation to

$$\frac{\partial p}{\partial z} = -\rho g. \tag{2.2}$$

This approximation is valid for a state where the horizontal scales of the motion are a lot larger than the vertical scales, and is typically utilized in ocean models not aiming to resolve convection or small-scale turbulence.

The density is determined in the empirically developed equation of state expressed as,

$$\rho = \rho(p_0, \theta, S), \tag{2.3}$$

where ρ is potential density, θ is potential temperature, S salinity and p_0 is a reference pressure. A new equation of state was provided by McDougall in 2010, the socalled thermodynamical seawater state, (TEOS10). It is now implemented in most ROMS-models. In our simulation the equation of state from 1985 (EOS85) was used.

The Boussinesq approximation entails a constant reference density in all products, except when multiplied with the Earth's gravitational constant (see appendix for details about how the set of equations is attained). A justification for this is that the oceans density's fluctuations are merely of a few percent from the reference value. The major consequence of such an approximation is reflected in the continuity equation

$$\partial_t \rho + \bigtriangledown \cdot \mathbf{v}\rho = 0, \tag{2.4}$$

which by setting $\rho = \rho_0$ amounts to

$$\bigtriangledown \cdot \mathbf{v} = 0. \tag{2.5}$$

A Bousinessq ocean is thereby not conserving mass, but volume.

Finally, a tracer conservation equations for solving, e.g salinity concentrations and potential temperature is expressed as follow

$$\partial_t C_i \bigtriangledown \cdot C_i \mathbf{v} = - \bigtriangledown_h \cdot \boldsymbol{\mathcal{F}} \ + S_i, \tag{2.6}$$

S_i denote the i'th source-term, C_i tracer concentration, and $\boldsymbol{\mathcal{F}}$ both vertical and horizontal fluxes due to turbulent mixing.

The variables are computed on an Arakawa C-grid (Arakawa.A, 1977), staggered in the vertical and horizontal, as shown in figures 2.1 and 2.2. The vertical and horizontal location of variables on the grid is depicted in figures 2.1 and 2.2, respectively.

[1]The following theory is based on Lecture Notes by Rø ed (2014)

The staggering is a normal procedure to limit the degrees freedom and the number of prescribed integration constants (initial/boundary values).

Griffies(2004) argues that *"the choice of vertical coordinate represents the most fundamental choice that can be made when designing an ocean model"*. The best choice for a vertical coordinate in oceans model is not an obvious one. There are three general classes of ocean models distinguished by their type of vertical coordinate, z-coordinate models (the earliest ones) based on the ocean depth, isopycnal-, utilizing layers of constant density, and sigma- or terrain following coordinates. The benefits of each choice is inevitably at the expense of other aspects of the numerical scheme. The Arctic4 model relics both the benefits and drawbacks of being a sigma-coordinate model.

A wellknown problem in sigma-coordinate models is the representation of the horizontal pressure gradient force. We compute the pressure gradient in the transformed sigma-coordinate system, (Griffies 2004) using the expression

$$\frac{1}{\rho_0} \bigtriangledown_z \, p = \frac{1}{\rho_0}(- \bigtriangledown_s + \partial_z \cdot \bigtriangledown_s)p. \qquad (2.7)$$

Pressure gradient errors (PGEs) arise due to errors related to the discretization, the non-orthogonality of the coordinate system, and complicated by the vertical stretching schemes frequently applied (Shchepeting and McWilliams, 2005).

Another limitation to the σ-coordinate is a so-called spurious diapycnal mixing associated with steep vertical coordinate slopes (Marchesiello 2010). Most part of the mixing of (both material and dynamical) tracers, happens laterally, i.e. along the isopycnals. However, when using upwind schemes in σ-coordinates, artificial mixing of tracers can occur across the isopycnals (Marchesiello 2010).

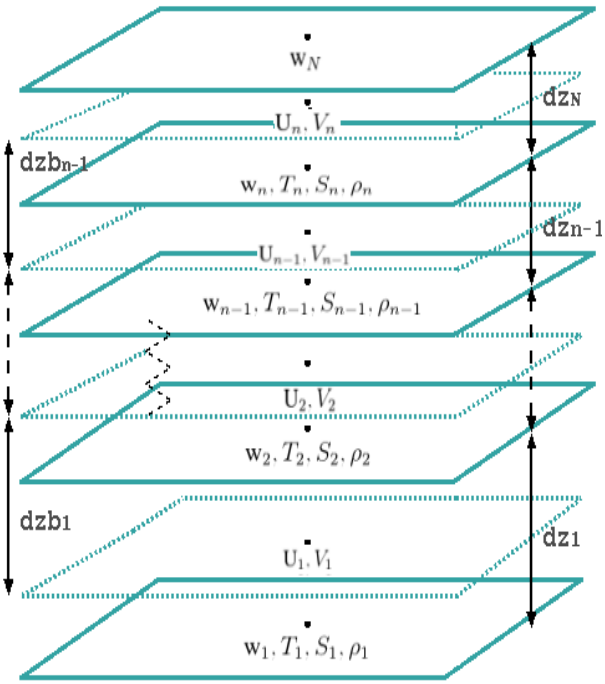

Figure 2.2: The vertical placement of variables, here depicted on an A-grid for simplicity.

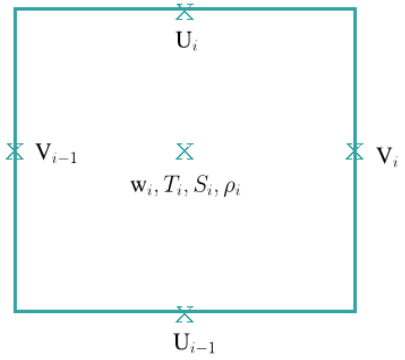

Figure 2.3: The horizontal placements of variables on the Arakawa C-grid.

2.2 The Arctic hindcast

The simulation is run for 17 years, and the first 6 years are considered a spin-up period, hence data from those years are discarded. The last 10 years of the simulation, when the system is believed to have reached a steady-state with a representable circulation and dynamics, is used. The model domain encompasses the Artic Ocean and it's sur-

rounding Seas, with the exception of the Bering Sea. The forcing data applied to the simulation was ERA-Interim atmospheric reanalyzes, and at the open lateral boundaries, operational ocean analyzes FOAM. River runoff was supplied from monthly climatologies (Isachsen (2015)).

The model-run used in this analysis contains 35 stretched vertical levels, with depths ranging from the order of 1m near the surface, to the order of 100m in the bottom-most cells. The resolution is increased near the sea surface, and allows for a well represented pycnocline profile. The horizontal gridspacing is 4 km.

A third-ordered upwind scheme for horizontal tracer and momentum advection was employed here, and a fourth-ordered centered scheme was used for vertical advection (Isachsen 2015).

The details of the model run is summarized in the table below:

The Arctic4 modelrun

MODEL	σ-coordinate (ROMS)
DOMAIN	minlat- max lat osv
RESOLUTION	4×4[km]
VERTICAL LAYERS	35 #
HORIZONTAL ADVECTION	3rd ordered upwind
VERTICAL ADVECTION	4th ordered centred
ATMOSPHERIC FORCING	ERA Interim
LATERAL BOUNDARIES	FOAM

2.3 Comparison with observations

How does the model fields compare to observations? We present a comparison of the hydrography in the model with the Arctic Regional Climatology(hereafter ARC). The climatology is based on the World Ocean Dataset (WOD) with data up until 2011 (downloadable at http://www.nodc.noaa.gov/OC5/regional_climate/arctic/). The model extends down to 45° in the North Atlantic, but since the climatology only covers the region from $60^\circ - 90^\circ$ N we compare the area north of 60° N. The ARC has a horiontal resolution of 0.25°, and is based on 87 levels in the vertical extending down to 4000m (more details can be found in Seidov et al., 2014). The climatology's annual dataset is comprised of all available data sampled through decades (Seidov et al., 2014). The Arctic4's ten-year averaged fields are interpolated onto the annually averaged ARC fields.

Figure 2.3 shows some discrepancies between the data. Overall, the model's temperature fields compare well with the ARC. We can clearly see the North Polar Front cutting through the Nordic seas, and extending into the Barents Sea. The sharp frontal zones west and east of Iceland are also correctly depicted, and the Polar Water exported from the Arctic is captured. The cold southward flowing Polar Water is met by the inflowing warm AW, resulting in the large temperature shift depicted along the Greenland-Scotland Ridge and Denmark Strait. Faroe However, in the Arctic Ocean the model depicts a nearly homogenous temperature field, while the ARC temperatures show some more structure, with warmer locations along the rim of the Arctic Ocean. The Kara Sea, and the northernmost part of the Larbrador Sea are also some degrees warmer in the ARC. We find the comparison satisfactory, as the deviations between the two fields is not occuring where the temperature is dynamically most important, but in the colder regions. Some of the difference we see may occur if the seasons in the climatological annual data are unevenly represented. There might be more available data during the warmer summer months, as many types of in-situ measurements are easier to obtain in more ice-free conditions, while the the model's seasons are weigthed the same. In a review of the ARC, Seidov et al. (2014) states that *"Because of the scarcity of winter observations, the possibility of seasonal bias in the high latitudes is always an issue"*.

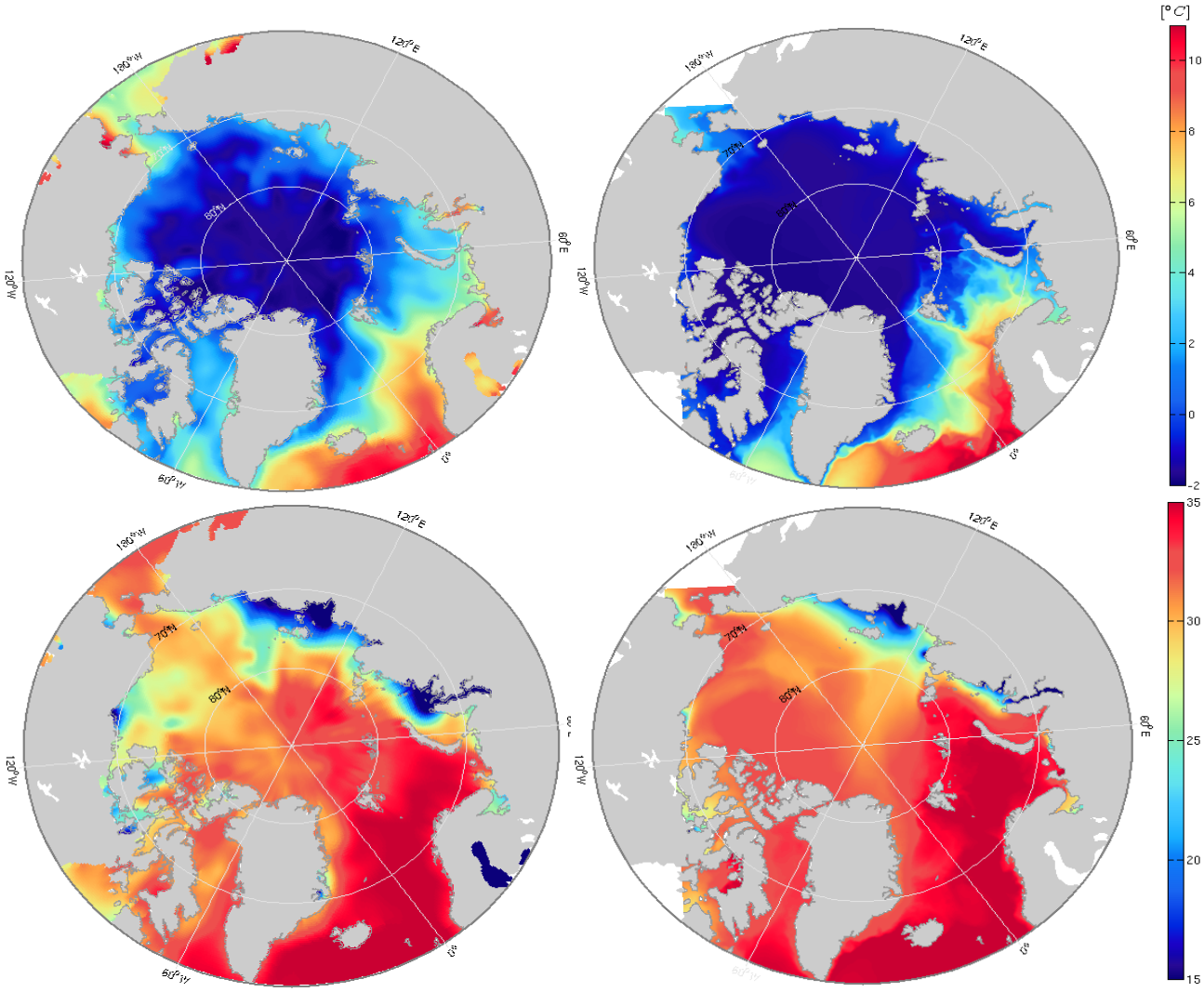

Figure 2.4: Annual temperature and salinity fields from the Arctic Regional Dataset (ARC), and the Arctic4 model.

The model's salinity fields within the Arctic Ocean deviates substantially from the ARC. There is a tongue of fresh water extending from the Laptev Sea into the Nansen Basin in the model, with increasing salinities westward toward the Canada Basin. The observations tend to an opposite distribution. In the Barents and Nordic Seas, is the distribution of model-salinity in close agreement with the climatology. The North Polar Front is exhibited in the salinity-field as well. The outflow from the Fram Strait and the onset of the EGS is substantially fresher in the observations.

A closer look into the vertical stratification showed that, as most Arctic models, this model seems to have trouble getting the halocline correctly simulated in the Arctic Ocean. The halocline, which is the (sharp) transition layer between the fresh surface-waters and saltier Atlantic water below, is an essential ingredient in the Arctic Ocean circu-

lation. At low temperatures, seawater density is nearly fully dependent on the salinity, through the equation of state. Another essential role the halocline plays, is to isolate the ice from the warmer waters below, as mixing across highly stratified waters requires a lot of work. The salinity is therefore of uttermost importance to simulate correctly at high latitudes, as it is a dynamically controlling factor. The Kara Sea is notably fresher and warmer in the climatological data, both these factors contribute to making the water less dense, therefore the Kara Sea in the model will be unrealistically dense. This is also the case for the western Arctic basin.

Discrepancies in temperature and salinity may have an impact on the dynamics represented in the model. An appropriate concern for this present study is how this may affect the eddy field. As noted, the Rossby deformation radius is believed to represent the length scales which eddies that will dominate in the eddy field take on, and a key parameter to represent correctly. Subsequently, ocean models strive to resolve this horizontal scale, and the measure may serve as an indication to the degree of mesoscale activity explicitly present in a model.

The Rossby deformation radius depends highly on stratification, and is the solution to a linearized eigenvalue problem, attained from the quasi-geostrophic setting (see section 3.1-3.2). The solution yield eigenvectors, denoting vertical normal mode structures, and L_d is attained by the squared inverse of the eigenvalues (Vallis 2006). Moreover, for a constant stratification, L_d can be calculated using the WKB approximation (Chelton et al. 1998), which takes the form

$$L_d = \frac{\int_{-H}^{0} N dz}{f\pi} \tag{2.8}$$

where N is the squareroot of the bouyancy frequency, $N = (\frac{g}{\rho_0}\frac{\partial \rho}{\partial z})^{(1/2)}$, and ρ is potential temperature. Here we see that the Rossby radius depends on the stratification, the local earth's rotation rate and the total water depth. Ld is expected to take on larger values in areas of great depth, that is in the basins, but vary also with the degree of local stratification.

We compared calculations of the model field's Rossby deformation radius, by using the WKB approximation, to other calculations in recent studies, and noted some differences. In one study, Nurser and Bacon (2013) based their calculations on model-data, and in another, Zhao et al. (2014) utilized high-resolution ice-tethered profilers in conjunction with climatology data to account for the layers beneath 750m.

In the Arctic Ocean, the Canada basin and the Nansen basin are of similar depths, but differ in terms of stratification. In the Beaufort gyre encompassed by the Canada basin, the upper ocean is a lot fresher and somewhat colder, which makes the surface layers stongly stratified. The Nansen basin is more saline and the density therefore varies less with depth. In this regARC, we might expect to see a variation of the Ld of increasing values from east to west in the Arctic Ocean (Nurser and Bacon, 2013).

This is indeed what is seen in the observational studies, where the maximum scales are found in the Canada basin. The recomputed L_d from the climatology is higly comparable to what was attained in the mentioned studies (see figure 5a in Nurser and Bacon 2013; figure 4b in Zhao et al. 2014). As we can see, in the model L_d is largest in the Nansen basin rather than peaking in the Canada basin. Still, the model captures the values and spatial pattern well at most locations. The Nordic-, Barents- and Labrador Sea show a very good agreement with the observations. Since the L_d is expected to shear a link with eddy lengthscales and the spatial scale of the most unstable wave, we find this correspondance reassuring for the further analysis. Due to the model-data differences in the Arctic Ocean, we have chosen to focus on the surrounding Seas and will, at times, merely comment on that area.

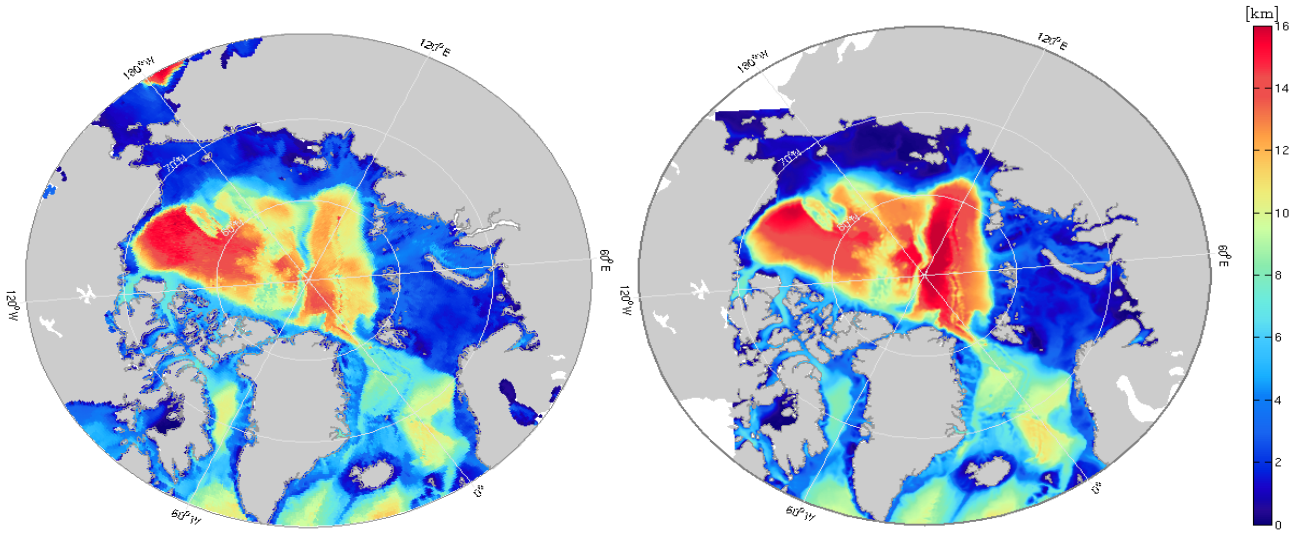

Figure 2.5: Rossby radius of deformation as calculated from observations (ARC) $0.25° \approx 30$km, and the Arctic4 model, 4×4km

Chapter 3

Linear stability analysis

3.1 Baroclinic instability explained

We make the assumtion that baroclinic instability can be regarded as the dominant process initiating the high degree of eddy activity observed in the Subarctic Seas. To examine this hypothesis, a local linear stability analysis is performed. This grants us characteristic properties of the instability process, which is useful for later comparison with eddy properties identified in the model field.

This chapter is organized as follows: First we describe process of baroclinic instability, secondly we work through the theory and procedure of the conducted linear stability analysis. We note the limitations therein, and lastly comment on the results.

3.1.1 The basic mechanism

We start this discussion by asking: What is the agenda behind baroclinic instability? This type of instability is both the atmosphere and ocean's response to differential heating, or horizontal density gradients.
The ocean, as well as the atmosphere, are continously working towards a state of minimum potential energy, with the centre of gravity at its lowest. Where there exists horizontal density gradients, surfaces of constant density (isopycnals) are slanted and thereby store available potential energy (APE). APE is the amount of potential energy that can be transferred into kinetic energy (Vallis 2006). In a non-rotating setting, a state of lowest energy entails flat isopycnals that are parallell to surfaces of constant pressure (isobars). An initial density disturbance would adjust in a way such that light fluid spreads uniformly on top of heavy fluid. The declination of the isopynals reduce pressure gradients, and eventually slow down the flow (Pedlosky, 1987). So, the flow equilibrates at a state of rest. However, when rotation is included, there exist an steady state where the isobars and isopycnals are not aligned, and the isopycnals are inclined. Through hydrostatic and geostrophic balance this steady state induces a vertically sheared flow called the thermal wind, by which horizontal density differences are balanced by velocity shear. This is expressed as $f\partial_z \mathbf{U} = \frac{g}{\rho_0}\mathbf{k}\times\bigtriangledown\overline{\rho}$ (attained by taking the vertical difference of the geostrophic relations, in combination with the hydrostatic balance).

Is this state stable to pertubations? Due to the sloping isopycnals, it is not a state of minimum potential energy as nature desires it to be. The slope of the isopycnals represent a pool of available potential energy, the steeper the slope is the more energy is available for conversion into kinetic energy. Small perturbations will frequently arise and grow at the expense of the system's APE, aided by baroclinic instability. In the beginning, these disturbances have a wavelike appearance, but they can quickly develop into swirling eddies. Furthermore, the eddies are, as remarked, efficient advecters of tracers, including heat.

We may further ask if the growth of initial perturba-

tions occur under any circumstances then?
Potential energy increases if lighter fluid sinks and denser fluid rises. This would raise the centre of mass, achieved by work done in the lifting mass against gravity. Conversely, when denser fluid moves down and lighter fluid is brougth up to replace it, potential energy is released.
The change in potential energy is expressed as

$$\Delta PE = g\Delta\rho\Delta z,$$

which relates the vertical displacement of parcels with change in densities (Vallis 2006). An instability may act to amplify the displacement. We realize this by considering the situation sketched in figure 3.1 that illustrates water parcel excursions. This state has a horizontal density gradient, the dotted lines depict the sloping isopycnals, and U is the induced thermal wind flowing with lighter waters to the right. The coloured circles represent fluid parcels in different exchange-scenarios. We can readily see that if the red and pink fluid parcels were vertically exchanged, a denser(red) fluid parcel with a lighter(pink) is exchanged. Restoring forces,respectively gravity and buoyancy, will act on them. Hence, in this stable scenario, and the parcels are forced back to their initial positions. On the other hand, if the blue and red fluid parcels are exchanged, in a slantwise manner, there is no restoring force acting on them. This is because ligth fluid is placed in a denser environment and dense fluid in a lighter environment. Hence, they would shoot past these positions, and their original motion gets amplified. The exchange between those parcels are unstable. The exchange path is not arbitrary however. The grey wedged area signify the possible range of path-angles for an unstable exchange. For an exchange path b and an isopycnal slope a, the angle of the path thus needs to be between

$$0 < b < a.$$

A purely horizontal exchange, at an angle of zero degrees, is a neutral exchange with no restoring forces. It can be shown that the maximum conversion to kinetic energy occurs at an angle $a/2$ (see Vallis 2006). The release can cause vigorous eddy velocities (Thorpe 2005).

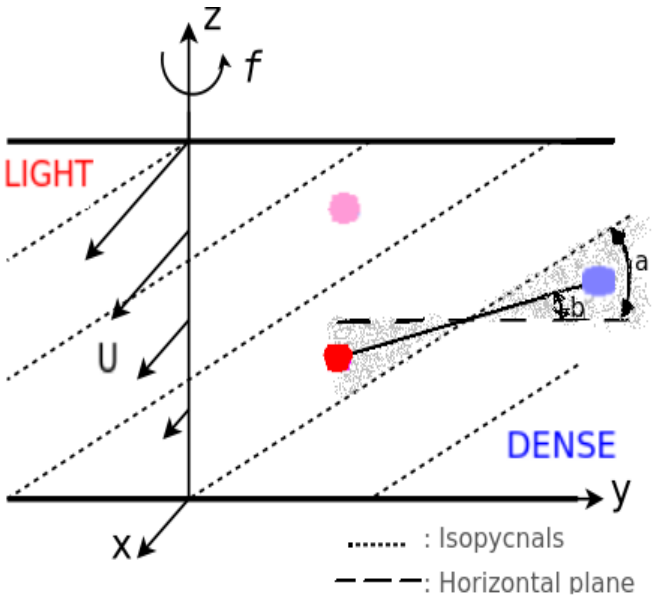

Figure 3.1: The colored circles represent fluid parcels. If the path of the red and blue parcels lie between the horizontal plane, and the isopycnal slope a, an exchange is unstable. Based on a figure from Tulloch (2009)

In the rest of this chapter, we will be concerned with the selection of waves that grows most rapidly in an unstable background flow. The fastest growing wave will extract the maximum APE present in the system, presumeably near $a/2$. Naturally, there are often constraints to this. We can easily see that by adding a topographic slope where the exchange occurs in figure 3.1.

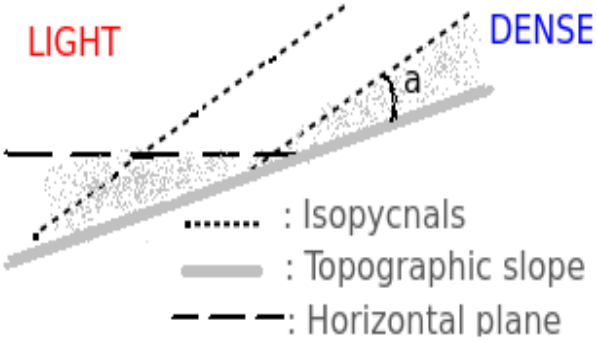

Figure 3.2: The grey line signify a topographic slope. Possible fluid-paths within the shaded area are reduced when topography is added.

The area of instability is reduced in this configuration. Several studies show that adding a topographic slope, will tend make the system more stable (Pedlosky, 1964). However, others have shown that this can destabilize the system (Orlanski 1969). For instance, consider a scenario where the angle of the bottom slope is $a/2$. If a horizontal motion onto a bottom slope induce a vertical motion proportional steepness of the slope, then perturbed waves will have a maximum unstable plane. We can easily see that if the topographic slope becomes as steep as a, or exceeds a, the shaded area dissappears and the system is stablilized.

We have started this discussion in a conceptual manner, but we will now move on to review the theory underlying our numerical analysis.

3.2 The linearized problem

The foundation of eddy dynamics has its core nearly exclusively in the theory of quasi-geostrophy(QG hereafter) (Vallis 2006). The QG framework is a reduced set of equations, and is commonly utilized to model motions of small Rossby numbers, in both the ocean and atmosphere. Vallis (2006) claims that no other set of equations are used more than this in theoretical studies. Studies based upon the QG equations have been able to succesfully account for *"wave and vortex propagation, long-lived coherent vortices, geostrophic turbulence with its forward and inverse cascade, eddy generation (from baroclinic or barotropic instabilities), eddy fluxes and surface frontogenesis"* (Mcwilliams,2008).

The evolution of eddies is predominantly non-linear, and the analytical treatment of such a problem is not attainable (Pedlosky, 1987). A way to work around the complexity caused by the nonlinearity, is to consider a linearized QG setting. A linear stability analysis(LSA hereafter) can uncover regions of instability, and has provided consistent predictions of the preferred length-scales and growth rates of oceanic mesoscale variability.(Smith 2007, Tulloch et al., 2011, Isachsen 2015). The major limitation inherent in the linear pertubation theory, is naturally that it is linear, and, as we noted, the evolution of mature eddies is highly nonlinear(Pedlosky, 1987). Hence, the LSA can merely yield the commencement of instability, and is not able to account for any further developements in the amplification of the unstable waves. Still, the most unstable mode is believed to emerge first from a background state of small perturbations, and commonly regarded to be the dominant one as the growth persists. Thereby, despite the non-linear evolution that most certainly occur at some a later stage, the LSA can render a "general character of the original profile" (Manley and Hunkins, 1985). Fundamental quantities to draw from a stability analysis are the rate at which the unstable pertubation grows, the dominating length-scales and the geographical distribution these. The growth rate signifies the time from the pertubation arises until it is a fully developed turbulent motion.

The LSA procedure can be summarized in three main points:
1. The quasi-geostrophic potential vorticity(QGPV) equation, and equations valid at the boundaries are linearized about a mean state.
2. An eigenvalue problem is formulated by inserting a plane-wave solution into the linearized equations, and then discretizing them.
3. Stability coefficients, eigenvalues with their associated eigenvectors, are extracted from the solution of the eigenvalue problem. These yield growth rates and lengthscales of the prominent growing wave.

Next we will look at the equations creating the foundation for the LSA, and then we explain the LSA procedure.

3.3 Theory

For flow in the interior, away from forcing and dissipation, the QGPV-equation is expressed as

$$\frac{D_g q}{dt} := (\partial_t + \mathbf{u_g} \cdot \bigtriangledown) q = 0, \ -H < z < 0, \tag{3.1}$$

where q is the potential vorticity, and $\mathbf{u_g} = u_g\mathbf{i} + v_g\mathbf{j}$ (subscript omitted hereafter) is the geostrophic horizontal velocity vector, and $(\mathbf{i}, \mathbf{j})$ are the unit vectors in the horizontal plane. Furthermore, $\bigtriangledown = \frac{\partial}{\partial x}\mathbf{i} + \frac{\partial}{\partial y}\mathbf{j}$ is the horizontal gradient operator.

With the aid of a streamfunction,ψ, and the hydrostatic balance, the horizontal momentum equations have been compressed into one equation with only one unknown, ψ. By definition $\psi = \frac{p}{\rho_0 f_0}$, which under geostrophy gives $u = -\frac{\partial \psi}{\partial y}$ and $v = \frac{\partial \psi}{\partial y}$. The relative vorticity expressed in terms of the streamfunction is $\zeta = \partial_x v - \partial_y u = \bigtriangledown^2 \psi$.

$$q = \bigtriangledown^2 \psi + \beta y + \frac{\partial}{\partial z}\frac{f_0^2}{N^2}\frac{\partial \psi}{\partial z}, \tag{3.2}$$

The first term in q is the relative vorticity, the second term denotes the planetary vorticity, and the last term is the socalled stretching term accompanying vertical changes in density (Lacasce 2013). The evolution equation reveals that for a parcel of water following the geostrophic flow, potential vorticity is conserved (Lacasce 2013). This means that as the flow evolves, q is not changed but merely relocated.

The flow in the interior typically couples with buoyancy-conditions at the boundaries. The buoyancy is defined as $b = \frac{g}{\rho_0}\frac{\partial \rho}{\partial z}$, and from hydrostatic balance, $b = f_0 \frac{\partial \psi}{\partial z}$. The equation valid at the boundaries, at the top $z = 0$ and the bottom $z = -H$, is the buoyancy equation(Vallis 2006).

$$(\partial_t + \mathbf{u} \cdot \bigtriangledown) b = 0, \ z = 0 \tag{3.3}$$

$$(\partial_t + \mathbf{u} \cdot \bigtriangledown) b + N^2 \bigtriangledown \mathbf{h} = 0, \ z = -H \tag{3.4}$$

where topography is included at the lower boundary.

The equations we now have at hand encompass processes on both long and short timescales. We are interested in the part of the flow which is associated with processes occuring on a short timescale. To separate the slow mean state and the quicker (eddying)state, we then divide the stream-function into a mean part and a fluctuating part, $\psi = \Psi + \psi'$. This results in the mean and eddying terms

$$q = Q + q', \text{ where} \tag{3.5}$$

$$Q = \bigtriangledown^2 \Psi + \beta y + \frac{\partial}{\partial z}\frac{f_0^2}{N^2}\frac{\partial \Psi}{\partial z}, \tag{3.6}$$

$$q' = \bigtriangledown^2 \psi' + \frac{\partial}{\partial z}\frac{f_0^2}{N^2}\frac{\partial \psi'}{\partial z}. \tag{3.7}$$

We also use $b = B + b'$,$h = \mathbf{H} + h'$ and $\mathbf{u} = \mathbf{U} + \mathbf{u}'$.

The local mean horizontal flow and stratification are assumed to be slowly-varying in the horizontal, and only have a depth-dependence.

$$\mathbf{U} = U(z)\mathbf{i} + V(z)\mathbf{j} \tag{3.8}$$

$$N^2 = N^2(z) = \frac{g}{\rho_0}\frac{d\bar{\rho}}{dz} \tag{3.9}$$

The assumption of a horizontally slowly-varying background state allows for periodic horizontal boundary conditions, in both the x- and y-direction. This means that each location where the equations are solved is considered a 'box' with doubly periodic boundaries, here with a 4 by 4 km area. The flow entering on one side, is considered the same when exiting at the other side. This is referred to as the local approximation, and Tulloch et al. (2009) remarks that it obviously is not suitable universally, and that it ignores several dynamical possibilities. We need to keep in mind the limitations of this approach, as we proceed with the analysis. The assumption of a steady, mean current neglects that eddies might impact the background flow (Flierl and Pedlosky, 2007), and does not incorporate any advection of eddies that certainly do occur in the full state. In our study domain, there are also narrow jets and horizontal gradients occuring in tight bands, often on the order of the internal deformation radii (**?**). By this, we reckognize that the flow may be subject to substantial change even within a small area such as 4km, and violate the homogenous assumption. Venaille et al., 2011 comment on this issue, and argue that: *This shows the limitation of locality hypothesis: in regions characterized by strong spatial variations of the mean shear (i.e., close to western boundary currents or to regions where topographic steering is important), eddy properties at one point may be due to instabilities*

occurring in the same area but at a different place (at a nearby location).

We further linearize the QGPV-eqations, valid in the interior, and the bouancy equation, valid at the boundaries, around the vertically dependent mean state. In order to linearize, we need to make the assumptions that $\mathbf{u}' << \mathbf{U}$, and that product of pertubation terms vanish, i.e. $\mathbf{u}'\mathbf{u}' \approx 0$. This assumption highlights another significant limitation of the linear approach. We have to keep in mind that even though the pertubations might be small initially, they do not necessarily stay small in the preceding evolution of the flow. The pertubation could in fact grow stronger than the background flow, as non-linear effects start to take precedence.

The linearization leaves us with

$$(\partial_t + \mathbf{U}\cdot\bigtriangledown)q + \mathbf{u}\cdot\bigtriangledown Q = 0,\ -H < z < 0$$
$$(\partial_t + \mathbf{U}\cdot\bigtriangledown)b + \mathbf{u}\cdot\bigtriangledown B = 0,\ z = 0$$
$$(\partial_t + \mathbf{U}\cdot\bigtriangledown)b + \mathbf{u}\cdot(\bigtriangledown B + N^2\bigtriangledown h) = 0,\ z = -H$$

By the horizontally homogeneous(local) approximation of the background flow, we have also ignored the mean relative vorticity $\bigtriangledown^2\Psi$. The gradient of the mean PV becomes

$$\begin{aligned}\bigtriangledown Q &= \mathbf{i}\partial_x Q + \mathbf{j}\partial_y Q \\ &= (\partial_z \frac{f^2}{N^2}\partial_z V)\mathbf{i} + (\beta - \partial_z \frac{f^2}{N^2}\partial_z U)\mathbf{j}\end{aligned}$$

where we have taken advantage of $V = \partial_x\bar{\Psi}$ and $V = -\partial_y\bar{\Psi}$. To lighten the algebraic burden in the further analysis we set the vertical stretching operator to $\partial_z \frac{f^2}{N^2}\partial_z = \Gamma$, yielding

$$\bigtriangledown Q = \Gamma V\mathbf{i} + (\beta - \Gamma U)\mathbf{j} = \beta\mathbf{j} - f\partial_z\mathbf{s}.$$

This follows the nomenclature of Smith (2007).

3.3.1 The eigenvalue problem

The pertubations we are seeking have wavelike appearances. Since the linearized equations have constant coefficients, we can search for normal-mode solutions expressed as

$$\psi = Re\{\hat{\psi}(z)e^{i(kx+ly-i\omega t)}\}. \tag{3.10}$$

Here $\hat{\psi}$ is the vertical structure of the pertubation, and ω the wave frequency, which both might take on complex values. $k,\ l$ are the horizontal wavenumbers, and the argument signify the wave's translation in space and time. Re denotes taking the real part of the product of the amplitude and $e^{i(kx+ly-i\omega t)}$. Since the equations are linearized, we can consider the solution for each set of wavenumbers as valid on its own. The substitution into the interior-eqations gives (after dealianiting the common factors i and $e^{i(kx+ly-i\omega t)}$)

$$(\mathbf{K}\cdot\mathbf{U} - \omega)(\Gamma - \kappa^2)\hat{\psi} + [k(\beta - \Gamma U) - l\Gamma V]\hat{\psi} = 0$$
$$\omega(\Gamma - \kappa^2)\hat{\psi} = [(kQ_{\mathrm{y}} - lQ_{\mathrm{x}}) + \mathbf{K}\cdot\mathbf{U}(\Gamma - \kappa^2)]\hat{\psi}$$

where Γ is the vertical stretching operator $\frac{\partial}{\partial z}(\frac{f^2}{N^2}\frac{\partial}{\partial z})$ and K is the wavenumber modulus $\sqrt{k^2 + l^2}$.
We furthermore make the substitution in the boundary equations. The upper and lower boundary condition, at $z = 0$ and $z = -H$ respectively, then takes the forms

$$(\kappa\cdot\mathbf{U} - \omega)\partial_z\hat{\psi} = k\partial_z U + l\partial_z V$$
$$(\kappa\cdot\mathbf{U} - \omega)\partial_z\hat{\psi} = [k\Omega_x + l\Omega_y]\hat{\psi}$$

where $\Omega_x = \partial_z U - \frac{N^2}{f}\partial_y h$, and $\Omega_y = \partial_z V + \frac{N^2}{f}\partial_x h)$.

Upon the discretizing the vetical stretching operator,Γ, the analysis amounts to solving a generalized eigenvalue problem, on the discrete form

$$\omega B_{\mathrm{ij}}\hat{\psi}_{\mathrm{j}} = A_{\mathrm{ij}}\hat{\psi}_{\mathrm{j}}. \tag{3.11}$$

where

$$B_{\mathrm{ij}} = \Gamma_{\mathrm{ij}} - K^2\delta_{\mathrm{ij}}, \tag{3.12}$$
$$A_{\mathrm{ij}} = (kQ_{\mathrm{y,m}} - lQ_{\mathrm{x,m}})\delta_{\mathrm{ijm}} + (kU_{\mathrm{m}} + lV_{\mathrm{m}}\delta_{\mathrm{inm}}B_{\mathrm{nj}}) \tag{3.13}$$

The δ-symbols represent Kronecker tensors,

$$\delta = \begin{cases} 0,\ i \neq j \neq k \\ 1,\ i\ =\ j\ = k \end{cases} \tag{3.14}$$

equal to one for the diagonal elements, and otherwise zero.

Hence the tensor products with δ_{ijm},δ_{inm} in the computation of A_{ij}, yield matrices with the vectors $(kQ_{\text{y,m}} - lQ_{\text{x,m}})$ and $(kU_{\text{i}} + lV_{\text{i}})$ remaining on the respective diagonals. The first term is thus an $i \times j$-matrix, as well as the last term resulting from $i \times n \cdot n \times j$ matrix-product. Both A_{ij} and B_{ij} becomes tri-diagonal matrices, which simplifies the discretization. In the idealized cases with constant stratification and equidistant layer depths, these matrices will be symmetric. This symmetry is broken in the full case we are considering. The eigenvalue problem we have presented so far is thus comprised of real, non-symmetric matrices. However, we will add some friction to deal with high growthrates at very small spatial scales. This is done in the form of a scale-selective horizontal, isotropic diffusion operator, $A_h \bigtriangledown^2 \psi$, and becomes a part of matrix B. By adding this element, the B becomes a complex matrix.

The discretized problem is solved on a grid with N levels. The matrices therefore have the sizes $N \times N$, and the solution renders N eigenvectors and their associate eigenvalues. The eigenvectors signify the normal modes $\hat{\psi}(z)$, and yield the vertical structure of the instabilities. The eigenvalues are the frequencies, $\omega = \omega_r + i\omega_i$, that may attain a nonzero complex value(Smith 2007). Whenever the frequency has a positive imaginary part, there arises a term, $e^{\omega_i t}$ which amplifies the amplitude $\hat{\psi}$ exponentially in time, t. From 3.13, and replacing $\omega = \omega_i + \omega_r$ we consider

$$\psi(x, y, z, t) = Re\{\psi(z)e^{\omega_i t}e^{i(kx+ly-\omega_r t)}\},$$

and realize that the unstable modes will grow at a rate ω_i. In the case of instability, the vertical structure of the amplitude, $\psi(z)$, is complex. The structure is retrieved from

$$\psi(z) = |\psi(z)|e^{\theta(z)} \tag{3.15}$$

$|\psi(z)|$ denotes the amplitude, and $\theta(z)$ the phase.

We pause here for a brief moment, to make an important remark concerning a prerquisite for instability and allow the disturbance to extract energy from the state. Interestingly, we will realize shortly that a vertical tilt, $\partial_z\theta \neq 0$, of the phase is needed. In addition, it also needs to be in a special relationship with the vertical velocity shear, for an instability to occur.
To examine this we follow Wright (1987).

From figure 3.1 we realize that the process of leveling out the inclined isopycnals entails a down-gradient bouyancy flux. The flux occurs horizontally across the sloping isopycnals when the water parcels are exchanged. A horizontal bouyancy flux can be expressed as $-\frac{g}{\rho_0}\overline{\mathbf{u}'\rho'}$, where $\mathbf{u}'$ is the horizontal vector of the perturbed velocity, and ρ' a density anomaly. We consider for simplicity, an exchange occuring in a positive y-direction and thereby only utilize the associated velocity component, v'. Under the geostrophic and hydrostatic assumption, and by inserting the wave solution $(A(z,t)e^{i\Phi(x,y,z,t)}$ where $\Phi = kx + ly - \omega t + \theta(z)$, the horizontal buoyancy flux can be expressed as

$$-\frac{g}{\rho_0}\overline{\mathbf{u}'\rho'} = (\frac{A^2 k}{2\rho_0^2}\frac{\partial_z\theta}{f_0}). \tag{3.16}$$

We take note here that if $\partial_z\theta$ is zero, there will be no horizontal buoyancy flux, and the wave cannot grow. In figure 3.1 again, it is evident that for there to be a release of potential energy at some depth, the product of this flux and the mean isopycnal slope need to be positive. The mean isopycnal slope,s_z can through thermal wind balance be expressed as

$$f_0\partial_z\mathbf{U} = \frac{g}{\rho_0} \bigtriangledown \overline{\rho}, \tag{3.17}$$

$$\text{with } N^2 = \frac{g}{\rho_0}\frac{\partial\overline{\rho}}{\partial z}, \text{ we get} \tag{3.18}$$

$$s_z = \frac{\bigtriangledown\overline{\rho}}{\partial_z\overline{\rho}} = -\frac{f_0}{N^2}\partial_z\mathbf{U}. \tag{3.19}$$

The product then takes the form, (for exchange in the y-direction)

$$-\frac{g}{\rho_0}\overline{\mathbf{v}'\rho'} \cdot s_z = \frac{1}{2}(\frac{Ak}{\rho_0 N})^2\frac{-\partial_z\theta\partial_z U}{f_0 k} < 0 \tag{3.20}$$

By reckognizing that (and recalling that $\Phi = kx + ly - t + \theta(z)$)

$$-\frac{\partial_z\theta}{k} = -\frac{\partial_z\Phi}{\partial_x\Phi} = \frac{\partial x}{\partial z}|_{\Phi=constant},$$

we discover that the lines of constant phase need and the velocity shear need to tilt in the opposite direction for .. to be valid, and allow release of APE. Wright makes the remark that it is not necessary for this criteria to hold at every depth level. LeBlond and Mysak (1978) showed that an adequate requirement is for the integral of 3.22, over the extent(in the y and z direction) of the disturbance, to fulfill the criteria.

3.3.2 Generalized QGPV

We will now look into a neat way to handle the boundary conditions, and later see how they are invoked in the discrete problem on the model grid. Bretherton (1966) presented a sophisticated way of generalizing the potential vorticity approach, to encorporate the boundary conditions into the equations valid for the interior. Bretherton considered baroclinic instability in fluids, and showed that any flow with horizontal temperature gradients over a rigid plane boundary, could be regarded identical to a flow with homogeneous temperature distribution over that plane, if one considers a concentration of PV adjacent to the boundary (Lappa 2005). The concept behind this is to add surface contributions to the interior PV, where isotherms intersecting the boundaries are imagined to progress along the boundary in an infinitesimally thin layer. The temperature gradient next to the boundary, and thereby the PV, is infinitely large. Consequently, the evolution of PV can be attained merely by the prognostic equation

$$\frac{D\hat{q}}{dt} = 0,$$

where $\hat{q}$ includes the addition of Dirac delta-functions at the top and bottom boundaries, of which intensities reflect the boundary temperature gradient.(Lappa 2005)

Consider the integration of q over a very thin layer, from the bottom $-H$ to a distance ϵ above.

$$\int_{-H}^{-H+\epsilon} q dz = \int_{-H}^{-H+\epsilon} \Big(f + \bigtriangledown^2\psi\Big) dz + \frac{f^2}{N^2}\frac{\partial\psi}{\partial z}\Big|_{-H}^{-H+\epsilon}$$

In the continous limit as ϵ goes to zero, the integration equals zero. However by implementing a constant temperature at the boundary, i.e. setting the term $\frac{\partial\psi}{\partial z}_{-H}$ to zero there, we get

$$\int_{-H}^{-H+\epsilon} q dz = \frac{f^2}{N^2}\frac{\partial\psi}{\partial z}\Big|^{-H+\epsilon} = q_b$$

Here we recognize that when applying a homogenous boundary condition, the sheet close to the boundary act as dirac-delta sheet, where the bottom vorticity goes to zero as it approaches the bottom. The same is valid for the upper limit. This allows us to express the QGPV equation in a generalized form

$$\frac{Dq}{dt} = \frac{D}{dt}\Big[q + q_b\delta(z-H) + q_t\delta(z)\Big] \qquad (3.21)$$

3.3.3 Neccesary conditions for instability

Even[1] though we know that most flows atmospheric and oceanic flows are ubiquitously unstable to instabilities, we do not generally know the stability of a flow. Since we simply cannot infer the stability of a particular flow regime, we need to make a stability-assessment. The stability of different scenarios in baroclinic flows has been under numerous investigations, that for the most part have relied upon the work of three pioneers, Charney (1947), Eady (1949) PHILLIPS (1954). They developed simplified, idealized models of baroclinic instability, that managed to capture essential aspects of the process. **?**CH64) and Pedlosky (1964) rendered conditions that needed to be fulfilled in order for a perturbation to grow, for these frameworks. This has later been referred to as the Charney-Stern-Pedlosky(CSP) criteria. By multiplying the eigenvalue problem by the complex conjugate, ψ^*, and integrating over the domain, they found that if there exist a non-zero imaginary eigenvalue, the vertical mean PV gradient in a combination with the boundary velocity-shear needs to change sign for the integral to become zero (see Vallis 2006 for more details).

The conditions for instability are simplest in the idealized case where the perturbations do not vary in the y-direction, and the mean flow is aligned in the x-direction, between to horizontal boundaries. This is the case we will consider here. We furthermore

[1]This subsection bases much upon an unpublished compendium(lecture notes) of Lacasce (2013)

need to consider the structure of $\partial_y Q$, and sign of the velocity shears(or the horizontal density distribution through the thermal wind balance) at the top and bottom boundaries. The possibilities for fulfilling the conditions can easily be demonstrated in a condensed form provided by the generalized context recently discussed. The delta-sheets of PV at the boundaries are included in the mean PV-gradient to give

$$\partial_y Q = \partial_y Q + \Gamma U^{top}\delta(z) - \Gamma U^{bot}\delta(z - H)$$

For an instability to occur, this expression need to become zero, i.e change sign somewhere in the vertical. Figure 3.3 gives an overview of the necessary CSP-conditions for the idealized case with a purely zonal flow ($V = 0$).

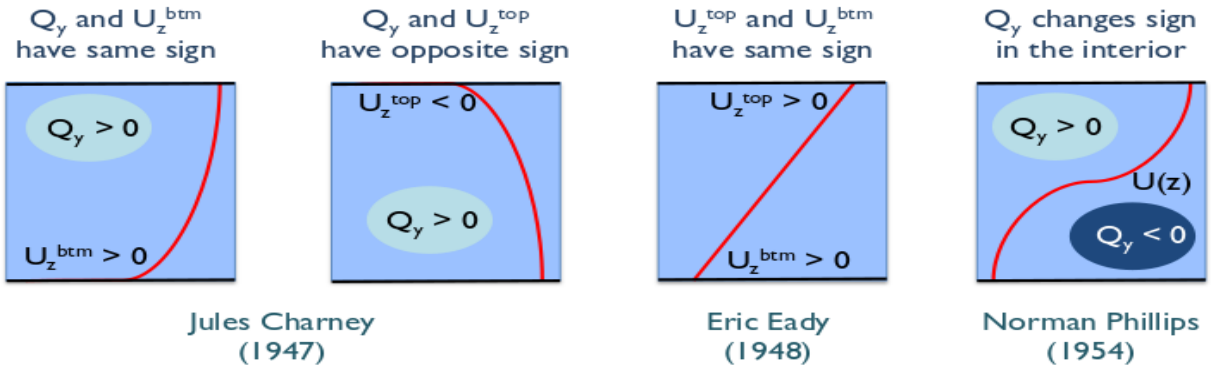

Figure 3.3: Different possibilities for instability in idealized scenarioes, depending on the top and bottom contibution to the mean PV-gradient and to the structure it.

This demonstrates different scenarios which may allow for an instability to occur. We should take note that all of these criteria are necessary for instability, but do not guarantee it however. These idealized cases yields three general types of instabilities (Smith 2007). Even for more complex cases with a lot more possibilities for instabilities, the instabilities are often referred to as Eady-type, Charney-type, and Phillips-type (Vollmer and Eden 2013, Smith 2007) based on their characteristics.

Scenario 1) and 2): The first two scenarios represents the problem of Charney (1947), with an unbounded boundary at the top or bottom. He studied the interaction between a thermal gradient and a non-zero interior PV-gradient, i.e an interplay between an edge wave and an interior PV-wave. β is included, which serve as the key ingredient in this model, and the velocity shear is constant. If $\partial_y Q$ in the interior has the same sign as the shear at the bottom, (nr.eq.) will *potentially* become zero. The next possibility, is when the shear at the top, and the interior $\partial_y Q$ have the opposite sign. The latter is more suited an oceanic setting where high velocity shears often occur in the surface layers. Charney-instabilities, in this case, then represent surface-trapped(surface-intensified) waves. The former is more realistic for an atmospheric setting.

Scenario 3):The third scenario represent the well-known investigation by Eady(1949). He considered flow between two rigid, flat boundaries. The background state in this model has constant stratification ($N^2 = constant$), and hence a constant velocity shear, furthermore β is neglected. This amounts in a zero mean interior PV-gradient. Hence, the velocity shears at the top and bottom need to be of same signs. Eady instabilities clearly depend fully on the boundary conditions. The instability arises from the interaction of edge-waves(or shears/density gradients) at the surface and bottom(Smith 2007). The amplitude of these waves decay exponentially from the surfaces, and the shorter waves are not able to interact(JL2013). If too small, the waves merely propagate on their seperate boundaries, unaffected by eachother(JL2013). This creates a short-wave cut-off scale for instability. However, larger waves are able to 'feel' the effect of eachother consequently may interact under the right conditions.

The last state was studied initially by Philips (1954) in a two-layered model. He let $\partial_y Q$ change sign in the interior, and neglected any shear at the boundaries. The model has been extended to include more layers in later years. The mathematical formulation becomes very complex. The addiotion of more layers, allows the PV-gradient to change signs more than once with depth, which commonly tend to occur in the ocean. Philips' model supports possible interactions beween two PV-waves in the interior. In the extended version, several waves can interact.

3.3.4 Stability in the N-layered case

How does this relate to our present study? First of all, we seek a numerical solution instead of these aforementioned cases which need to be very idealized to attain an analytical solution. We include both the horizontal velocity components, β, and we consider variations in the ocean's bathymetry. By rotating into a reference frame where $\mathbf{U}$ is directed along the direction of the most unstable wave, η, and thereby $V \approx 0$, we can analyze the properties of the eigenfunctions in the CSP-framework. However, keeping in mind that there is not necessarily obvious exclusions of the different types of instability. The instability at play, may be share aspects of more than one general type.
We recall that

$$\partial_y Q = \beta - f\partial_z \mathbf{s},$$

where $U = -Ucos(\eta)\mathbf{i} + Vsin(\eta)\mathbf{j}$, and $V = Ucos(\eta)\mathbf{i} + Vsin(\eta)\mathbf{j}$. Here the slope denote a vector pointed along the $\mathbf{U_{tw}}$.
Furthermore by adding topography to the bottom boundary condition, it takes the form

$$\partial_y Q_b = \Gamma \partial_z \mathbf{U} - f\partial_y h \tag{3.22}$$

Therefore, the collection of factors that are liable to affect the stability, is β, the vertical difference in horizontal layer thickness, and a bottom slope. In the simple Eady case, instability is possible merely with sheared velocites at the boundaries. If then β is included, as in the Charney problem, the shears need to exceed a certain limit resulting from the non-zero mean PV-gradient. By modifying the constant stratification, we get a depth-varying isopycnal slope, $\frac{f^2}{N^2}\partial_z \mathbf{U} = \partial_z s$ as well. We remark that the value of β is on the order of 10^{-12} at these high latitudes, and plays a much smaller role than the other terms.
The slopes $\partial_y h$ (Isachsen 2003; Isachsen and Nøst 2003) and $\partial_z s$ are more significant here. The type of stability can therefore be analyzed crudely by examining the configuration of these slopes. For instance, for a Phillips type instability, the isopycnal slopes have to reverse their tilt for $\partial_y Q$ to change sign with depth. A more thorough classification can be done by examining the vertical structure of the unstable wave-amplitude. This is given by the eigenvector $|\psi|$. Eady instabilities will have maxima amplitudes at the two boundaries. The amplitude of Charney instabilties have a maxima at either boundary, that diminish quite immediately toward mid-depths. Phillips type instabilities entail larger amplitudes at the upper boundary, and a slower decay away from the boundary.

3.3.5 Eady growthrate and lengthscale

The Eady model encorporates the primary processes taking place in the development of a baroclinically unstable wave. Despite its simplicity, it is able to describe how perturbations spontaneously can be generated and grow at the expense of the APE. It also gives an account of how a certain structure will related to the mode unstable wave (Vallis 2006). The model is very popular due to its virtues of an easy numerical implementation, a low computational cost, and its simple, but still rich explanation of the process.

We recall that the assumptions taken are that $\beta = 0$, $\partial_z U$=constant, N^2 =constant and a rigid lid is specified at the lower and upper surface. The interior mean PV-gradient is zero, and the flow evolution is set by conditions at the boundaries. The velocityshear at the top and bottom, indicates, through the thermal wind relation, density gradients across the direction of the flow. The characteristics of the fastest growing mode in the Eady model, are attainable analytically. The analytical solution renders expressions for the growthrate and the lengthscale in terms of the mean stratification and velocity shear. Pedlosky (1987) shows that the maximum

growthrate is found to be approximately

$$\omega_{i,eady} = 0.31 * \frac{Utw}{L_d}, \tag{3.23}$$

$$\tag{3.24}$$

that occurs at the wavenumber

$$k_{eady} = \frac{\pi}{1.6} k_d, \text{ and } l = 0, \tag{3.25}$$

where $k_d = \frac{1}{L_d}$. With the WKB-approximation for $L_d = \frac{NH}{f\pi}$, we see that the lengthscale for the fastest growing Eady-wave is $\approx 2L_d$.

The conditions for growth mentioned above, will change when topography is added. An augmented Eady model which accounts for a linear topographic slope was studied by Blumsack and Gierasch(1972). Their findings show that a relation, δ, between the sense the topography and the isopycnals are tilted, in an important factor. To see the effects of this, we compute the Eady problem for different values of δ. Figure 3.4 below depict the growthrates' dependency on δ for different configurations of the bottom slope, and growthrate curves for three distinct scenarios (as also shown in Blumsack and Gierasch, 1972; Isachsen (2011); 2015).

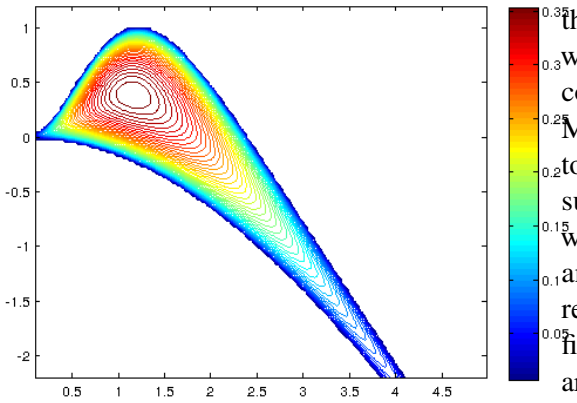

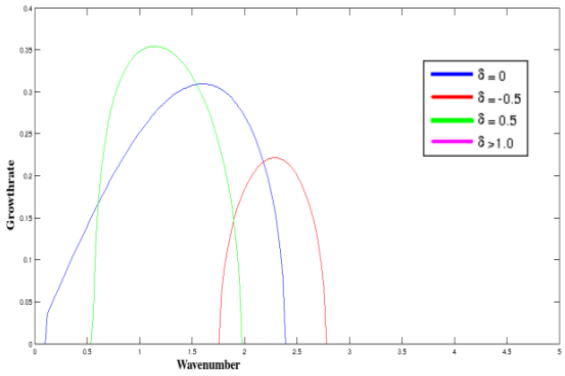

Figure 3.4: Top: Growthrates for different values of $\delta = \partial_y h / \partial_z s$ (for wavenumbers l=0), and non-dimensionalized wavenumbers $k \cdot L_d$. Negative values signify that the topographic slope is oppositely oriented the isopycnals slope. Bottom: Growth rate curves for the cases $\delta = 0.5$,$\delta = 0$ and $\delta = -0.5$, and $\delta = 1$.

From the top illustation, we realize that maximum growth (nondimensionalized by L_d/Utw) occurs when the topographic slope lies near half of the isopycnal slope. In this scenario, the bottom slope and the isopycnals slope the same way, like the scenario we discussed in fig 3.2. Th maximum growth near 0.5 suit the expectation of maximum growth for a particle path of half the isopycnal steepness. The maximum growth occurs at slightly larger wavelengths than for the typical $\delta = 0$, and at a larger rate of 0.35. This is evident from the growthrate curves in the following figure. We notice that the growth rate curve for $\delta = 1$, does not appear on the plot. When the slopes are oriented the same way and of equal magnitude, it acts to stabilize completely, as we can clearly picture in figure 3.2. Moreover, when $\delta < 0$ the growth will be shifted toward smaller and smaller wavelengths, and into a succesively narrower band. These coinsiderations will be beneficial to keep in mind in the coming analysis, as it is interesting to compare the more realistic case to the predictions of these simple configurations. We need to stress however, that these are highly idealized situations, and we do expect to find discrepancies in the more complex setting.

3.3.6 Energy transfer

An relevant aspect to look into is what contribution the waves make to the energy conversion between APE and EKE. Gill, Green and Simmons (1974, GGS hereafter) investigated the production of mid-ocean eddies by energy considerations. They made estimates of the transfer rate from APE to EKE, from the energy budget equation. The expression for this is attained by multiplying of the QGPV equation by $-\rho_0\psi$, and integrating over the domain (Smith 2007). The energy conversion term is comprised by the advection of the eddy PV by the mean shear (Smith 2007). Inserting a wavesolution to this, and integrating horizontally yields (See Smith 2007 or Gill et al., 1974 for details):

$$R(z) = \frac{V_e\rho_0}{2}\frac{f_0^2}{N^2}\frac{d\theta}{dz}\left(\frac{|\hat{\psi}|}{|\hat{\psi_{max}}|}\right)^2\frac{\kappa}{\kappa^2}\frac{d\mathbf{U}}{dz}, \quad (3.26)$$

where V_e is a velocity, θ the phase of the wave, $|\psi|, |\psi_{max}|$, the amplitude and it's maximum value. Integrating, $\int_{-H}^{0}(R(z)dz$, gives an estimate of the transfer, in Wm^{-2}. The LSA provide all the needed variables but one. We need to make an assumption regarding the velocity V_e. GGS determined this term by considering scenarios where the rate of energy removed by the eddies equalled the rate of energy supplied by the wind. The latter input was estimated to be around $10^{-3}Wm^{-2}$. GGS had found that the eddies were able to efficienly remove the energy-input by the wind, at a comparable pace. The maximum velocity, $0.08\ ms^{-2}$, were obtained by large-scale eddies. Smith et al. (2007) implemented this method for the purpose of filtering out less energetically important wave-selections in their global LSA. They set $V_e = 0.1m/s$, which was also our choice.

We recall than $\partial_z\theta$ and $\partial_z\mathbf{U}$ need to be tilted oppositely in an unstable wave. We then realize that $R(z) > 0$ for an energy transfer from APE to EKE. The magnitude is anticipated to be on the order of the crude estimate of the wind input, $10^{-3}Wm^{-2}$.

3.4 Discretization and numerics

3.4.1 Discretizating

We will not go into detail on how the matrices A_{ij} and B_{ij} are discretized, but we will show the discretized stretching operator. This serves to demonstrate the discrete implementation of the boundary delta sheets discussed in the last sections. The operator $\partial_z\frac{f^2}{N^2}\partial_z\psi$ is computed using centered differences, and takes the form

$$\Gamma_{nm}\psi_m = f_0^2\begin{cases}\frac{1}{\delta_{b_1}}\left(\frac{\psi_2-\psi_1}{N_2^2\delta_2-N_1^2\delta_1}\right), & n\ =\ 1\\ \frac{1}{\delta_{b_n}}\left(\frac{\psi_{n-1}-\psi_n}{N_n^2\delta_n-N_{n-1}^2\delta_{n-1}}-\frac{\psi_n+\psi_{n+1}}{N_{n+1}^2\delta_{n+1}-N_n^2\delta_n}\right), & n\ =2...N-1\\ \frac{1}{\delta_{b_N}}\left(\frac{\psi_{N-1}-\psi_N}{N_{N-1}^2\delta_N-N_1^2\delta_{N-1}}\right), & n\ =\ N\end{cases} \quad (3.27)$$

Here δ_b is the vertical distance between levels where buoyancy, $f\partial_z\psi$ are located, and δ is the distance between ψ-points. We refer back to figure 2.1 in section 2.1, where the bouyancy points and vertical differences will be collocated with w-points, and ψ lie at ρ-points.

We aquired the boundary conditions in the following procedure. The QGPV equation is attained by the combination of the vorticity and the buoyancy equation, respectively

$$\frac{D\zeta}{dt} = f\frac{\partial w}{\partial_z}, \text{ and}$$
$$\frac{D_h b}{dt} = -N^2 w$$

Realizing that $w = -\frac{1}{N^2}\frac{Db}{dt}$ the combination at the lower boundary yields,

$$\left.\frac{D\zeta}{dt}\right|_N = f\left.\frac{\partial w}{\partial z}\right|_N = -f\left[\frac{\partial}{\partial z}\left(\frac{1}{N^2}\frac{Db}{dt}\right)\right]\Bigg|_N$$

Furthermore, we invoke a homogenous boundary condition at the lowest layer, $\left.\frac{1}{N^2}\frac{Db}{dt}\right|_N = 0$. In the

discretized form this gives us

$$\left.\frac{D\zeta}{dt}\right|_N = -f\frac{D}{dt}\Big[\frac{1}{\delta z b_N}\Big(\frac{b_{N-1}}{N_{N-1}^2} - \frac{b_N}{N_N^2}\Big)\Big]$$
$$= -\frac{D}{dt}\Big(\frac{f}{\delta z b_N}\frac{b_{N-1}}{N_{N-1}^2}\Big)$$

Finally we arrive at the simple prognostic equation

$$\frac{D}{dt}\Big(\zeta_N + \frac{f}{\delta z b_N}\frac{b_{N-1}}{N_{N-1}^2}\Big) = 0 \qquad (3.28)$$

Inserting $b = f\frac{\partial\psi}{\partial z}$ and $\zeta = \bigtriangledown_h^2\psi$ results in

$$\frac{D}{dt}\Big[\bigtriangledown_h^2\,\psi + \frac{f^2}{\delta z b_N}\Big(\frac{\psi_{N-1}-\psi_N}{N_N^2\delta z_N}\Big)\Big] = 0 \quad (3.29)$$

The vertical spacing δz_N is the thickness of the bottom layer. In the continous case of the delta-sheet approximation, this is layer is infinitesimally thin. However, in its discrete form, this layer needs to be finite and represent the lowest layer on our grid. Consequently, the discretization entails an error of the order of this thickness of the lowest layer(Smith 2007).

3.4.2 Numerics

Due to the problem's relatively large computational cost, the algorithm was written in FORTRAN (the code is available from the author). To optimize the speed, the code was paralellized, and run on the University of Oslo's supercomputer, Abel. The job was still time-consuming after the parallellization, but the cluster machine offers yet another measure to speed up computations, namely an arrayrun. An arrayrun splits the computation into a prescribed number of smaller jobs, and makes it possible to run all these parallellized jobs simultaneously. The code was finally run in parallell split into 16 jobs. This was highly effective, and shortened the CPU-time of the run with about a tenthfold.

The library of eigenvalue solvers, LAPACK, was used to attain the eigenvalues and eigenvectors. LAPACK is the underlying library used when the Matlab command 'eig' is called, in which the appropriate solver is automatically chosen. However, when used in FORTRAN, the type of solver needs to be specified. We chose ZGGEV, able to handle complex, tridiagonal input-matrices Anderson et al. (1992).

The eigensolver algorithm ZGGEV[2] solves complex generalized eigenvalue problems for non-symmetric matrices of size $N \times N$. It calculates the eigenvalues, and on request also the generalized left and rigth eigenvectors, using the QZ-algorithm. We specified that the solver return all eigenvalues with their corresponding rigth eigenvectors. The QZ algorithm does not invert B, in case the B-matrix is singular. In the problem at hand, this will never occur, so formally it is equivalent to solving the common eigenvalue problem $C\mathbf{x} = \lambda\mathbf{x}$, where in this case $C = B^{-1}A$. The generalized eigenvalue problem solves the characteristic polynomial $|A - \lambda B|$, instead of the usual $A - \lambda I$. The eigenvalues are attainable if the former determinant equals zero The procedure is carried out in four steps containing various matrix reductions. In the third step, the eigenvalues are retrieved. The eigenvalues are the ratio of the diagonal elements of the now triangular matrices A and B. The ZGGEV does not output the ratio, but the elements as two $N \times 1$ vectors, α and β, such that

$$\omega_j = \alpha_j/\beta_j, \quad j = 1, 2, \ldots, N$$

are the attained eigenvalues once out of the solver. The eigenvectors are obtained form the triangular matrices in the final forth step, and then transformed back to the initial coordinate system.()

3.5 Results from the linear stability analysis

The linear stability analysis is conducted at each gridpoint in the domain of 1602×1202 horizontal points, and 35 vertical levels. The eigenvalue-problem is furthermore solved on a grid of wavenumbers, and the spectral domain is divided into 61×31 values of the wavenumber-components

[2]Information about the eigenvaluesolver in this section is obtained from *'LAPACK Users' guide'* (Anderson et al., 1992)

in the x- and y-direction, respectively. We take the advantage of conjugate symmetry inherent in the equations, where the following apply

$$\hat{\psi} e^{i(kx+ly-\omega t)} = \hat{\psi}^* e^{i(-kx-ly-\omega t)}.$$

Here, $\hat{\psi}^*$ denote the complex conjugate of $\hat{\psi}$. The symmetry yields an identical solution for a 180° rotation in wavenumber space, and allows us to only solve for the upper spectral plane. The wavenumbers are specified to lie in the intervals $-10L_d^{-1} < k < 10L_d^{-1}$ and $0 < l < 10L_d^{-1}$, scaled by wavenumber of the local Rossby deformation radius at each point.

3.5.1 Growth rates of the most unstable wave

We start by inspecting the growthrates extracted from the LSA. At each point, we make a selection of the largest, positive imaginary frequency, ω_i, and we record the associated wavenumbers. At each location, and for each wavenumber pair, (k,l), there can be several growing waves.

Figure 3. depict a map of the distribution of the maximum growth rates attained at each location. Overall, the pattern depicted is that most 'action' occurs in regions near boundary currents and along frontal zones. This suits the notion that baroclinic instability developes in regions of sloping isopycnals and vertical velocity shears (Gill et al. 1974). Along the coastal boundaries, the isopycnal slopes are steep and outcrops at the surface. This is due to the division between ligth coastal waters and denser basin waters. This gives rise to a horizontal density gradient, and furthermore currents in thermal wind balance translating with light waters to the right. As revealed here, these currents are susceptible to baroclinic instability. As expected the interiors appear more quiescent. On the long term, the isopycnals are generally more leveled out in the open ocean, and there is not much work to do for baroclinic instability. Thus in these areas, the most rapidly growing waves appear to be weaker. In the Barents Sea, however, regions of high growth rates are widespread.

The broad patches of very high growthrates found nearest shore, are areas with depths below 100 m, and below the 50m-isobath in the Chucki Sea. At these shallow depths, the QG approximation will most likely fail, due to dominating ageostrophic effects present there. Wind stresses at the surface (when icefree), as well as friction at the bottom, will break geostrophy. The entire, shallow water-column may be impacted. We therefore disregard the shallowest regions in our further analysis.

In the western part of the Arctic Ocean there is rapid growth along the Alaskan coast. This includes the well-documented region around Barrow Canyon, where eddy generations frequently have been observed (Pickart 2004, 2005; Wanatabe 2010). The Alaskan Coastal Current flows along the coast there, which has been deemed both barotropically and baroclinically unstable(Pickart and Appen 2012, Spall 2005). The western part of the Beaufort gyre, also believed to spawn shelf-break eddies into the Arctic Ocean interior(Wanatabe 2010), show high rates.

As highly unstable waves are commonly related to the boundary currents, and the currents are strongly confined to flow along the topography (Rossby et al., 200; Nøst and Isachsen 2003), high growth rates mainly coincide with regions of topographic slopes. It is interesting to note that intense wave developement largely concur with steep topographic slopes. We see elevated values at several places where the topographic contour lines converge. This is particularly evident along the steep slopes east in the Lofoten basin. From eq. 3.22 we saw that topography modifies the bottom contribution to the mean PV gradient, and hence influences the necessary condition for instability. It can prevent the gradient from changing sign or aid in a sign-change, surpressing or enhancing the instability, respectively. Seeing that topography can strongly influence the potential for instability, this implies that a flat bottom case, such as the Eady model, may be neglecting important features and not be dynamically adequate model. As noted, an augmented Eady model which accounts for a linear topographic slope was studied by Blumsack and Gierasch(1972).

Their findings showed that a relation, δ, between the sense the topography and the isopycnals are tilted, in an important factor. In studies focusing on the Lofoten basin, Isachsen (2011, 2015) noted that for the typical configurations of δ along the region of rapid growth, this theory predicts inhibited growth. He further remarks that the fact that merely adding bottom topography to the Eady model, will not yield a sufficient explanation for unstable growth at certain locations. Interior mean PV gradients need to be taken into account (Isachsen 2015).

3.5.2 Lengthscales of the most unstable wave

What length-scales are associated with the gravest modes? Figure 3.3 show the inverse wavenumber modulus, $1/\kappa = \sqrt{k_{max}^2 + l_{max}^2}$, of the fastest growing mode.

The map of spatial scales has a more noisy structure than the map of growth rates. Despite the noisiness in the field, some patterns stand out. The inflowing branches of the NAC depict larger lengthscales, of about 15km and higher. Thin bands of larger scales are also found along the westernmost branch of the NwAC, the EGC, and along the slope off the west coast of Greenland. In the entire Barents Sea, the spatial scales are small, of about 2-5 km. This is likely reflecting the shallow depths there, and the shallow waters on the continental margins also exhibit shorter scales than found in the basins. The Arctic roughly has larger scales in the Nansen basin, decreasing toward the west. Some parts of the boundary currents showing rapid growth, depict smaller horizontal scales. We refer here to the eastern flank of the NwAC, flowing along the Norwegian continental shelf, as well as the EGC as it tranlates around the tip of Greenland, and the Labrador current.

The source for the patchy appearance is likely linked to our unfiltered selection of the most unstable wave. Local maxima of growthrates can occur for several wavenumber pairs,k and l in wavenumberspace. The different maxima may arise due to distinct structures of the unstable modes (Tulloch et al.,2011). This will become evident in the next section where we examine the wave properties in more detail at specific locations. High growth rates found at very high wavenumbers, might signify surface intensified modes that do not play a large role the conversion of APE to EKE. Noise at high wavenumbers is also related to several zero-crossings in the mean PV-gradient induced by the noise in calculating the gradient. These disturbances are not baroclinic modes, but small-scale perturbations (Vollmer and Eden 2013). We are therefore not guaranteed the most energetically important perturbation by simply choosing the wave corresponding to the absolute maximum in wavenumberspace. A possible way to secure a better selection, is a filtering measure implemented by Smith (2007), which is based on the GGS energy transfer rate mentioned in section 3.3. The filtering act to leave out waves that do not contribute significantly to the energy converion. We employed this method, but did not get a large difference in the selected wavenumbers.

To filter out the small scale perturbations, we have chosen to use a scale-selective horizontal, isotropic diffusion operator, $A_h \bigtriangledown^2 q$. This is, as noted in 3.3.1, added to the LHS of the interior QGPV equation. This operator act on the very highest wavenumbers, so that most of these uninteresting features are left out. We are then more liable to select a larger and deeper mode, by avoiding most of these small features. This is apt because we desire to consider perturbations on the mesoscale.

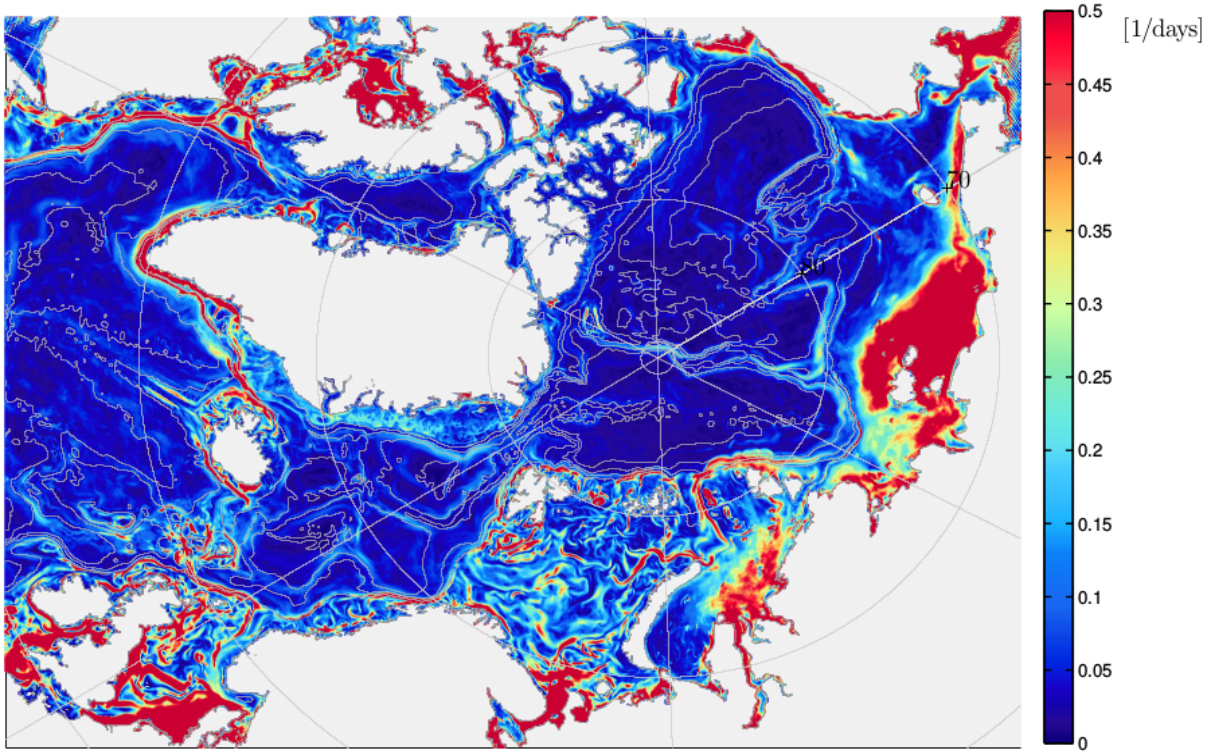

Figure 3.5: Maximum growthrates, ω_i, in $days^{-1}$

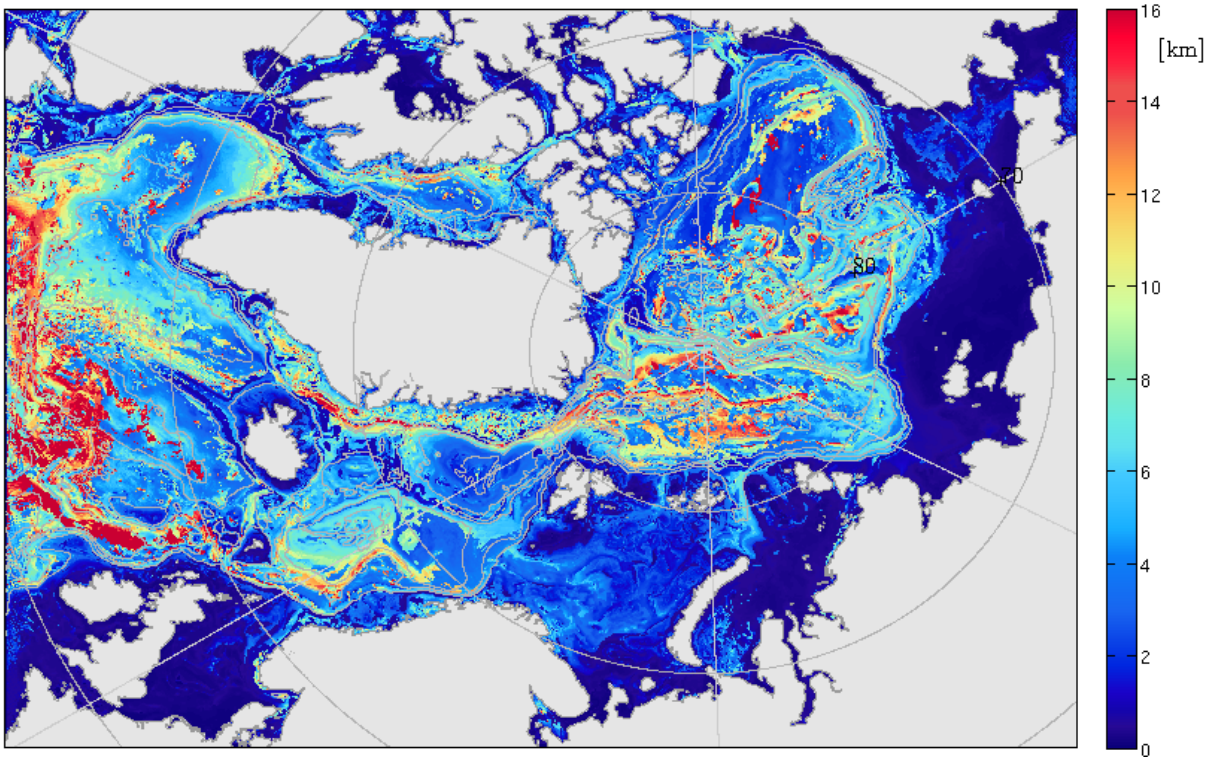

Figure 3.6: The associated lengthscale of the maximum unstable wave, $1/\sqrt{k_{max}^2 + l_{max}^2}$, in km.

3.5.3 Comparison with the Eady prediction

How does the Eady model compare to our more complex case? As noted, this simplified model of baroclinic instability is utilized in several studies to acquire the characteristics of unstable, growing modes. The model has demonstrated reasonable success in predicting properties associated with this type of turbulence(). Nonetheless, we point out again that the model does not represent a very realistic oceanic setting. Rather than having a constant velocity shear, the ocean typically experience high shears near the surface. An exponential profile decreasing rapidly with depth is therefore more realistic than the linear vertical velocity and density profile profile. The topography may also act to enhance or surpress instability. While the Eady model has a zero mean PV gradient allowing only for a coupling between two boundary-trapped waves, observed oceanic eddies might be governed by a completely different dynamics. It is therefore of interest to examine the Eady wave characteristics in ligth of a setting that includes a potential for all types of instabilities to occur.

We will in this section analyze the differences found in the properties of the most unstable waves in these two settings. The spatial pattern in two seperate maps(not shown) of the geographical distribution of the growth rates are strikingly similar. Regions of maximum growthrates are in agreement, and the Eady model seems to represent the fuller state quite well. This could lead us to anticipate a rather linear scaling relationship. It is more informative to examine maps of the scaling of the complex case versus the Eady model. In this way, we get an indication of over- or under-represented areas in terms of magnitude. We also look for discrepancies between the length scales associated with each scenario. We recall that the Eady length-scale is found near the Rossby deformation radius, at $L_d/1.6$. We thereby inspect the LSA lengthscales,L_{bci} in comparison with L_{eady}.

Figures 3.4-3.5 depicts the ratio of the maximum-growthrates found here, to that of the Eady prediction. The following picture shows how the LSA-lengthscales relate to the L_d. Both fractions are shown on a logarithmic scale.The white areas signify a scaling relationship of 1, and the red and blue values up to ten times larger or smaller values, respectively.

At first glance, the discordances are somewhat hard to systematize, as the distribution on the maps appear to be somewhat random. Still, the length-scales are primarily found to be *smaller* than L_d. In the Barents Sea and large parts of the continental shelves in the other Subarctic Seas, L_{bci} is found closer in accordance with the Eady conjecture. This is also true for flow along the frontal zones on either side of Iceland, and the inflowing branches of NAC.

On the other hand the growthrates exhibit more regions either of *larger* values, or in coherence with the Eady model. Very generalized, we find that large portions of the deeper waters have growthrates exceeding the Eady model. Curiously, when following the rim-current along the entire domain, most parts have lower values in comparison with the Eady growthrate. The EGC stand out as a clear example of this. What could be causing this tendency? Well, since these areas align with steeper topography than elsewhere, we might suspect that the topography may be a relevant factor. Smith (2007) notes that the vertical integration in the Eady-growth calculation smooths over smaller-scale instabilities, and may serve to partial explanation. Also, we revisit the comment on the modified Eady model, with added topography in the lower layer. For scenarios where the isopynals and the topography slopes in opposite directions, denoted by a negative δ and a common setting along the rim, an increasingly narrower band toward higher wavenumbers can give rise to instability.

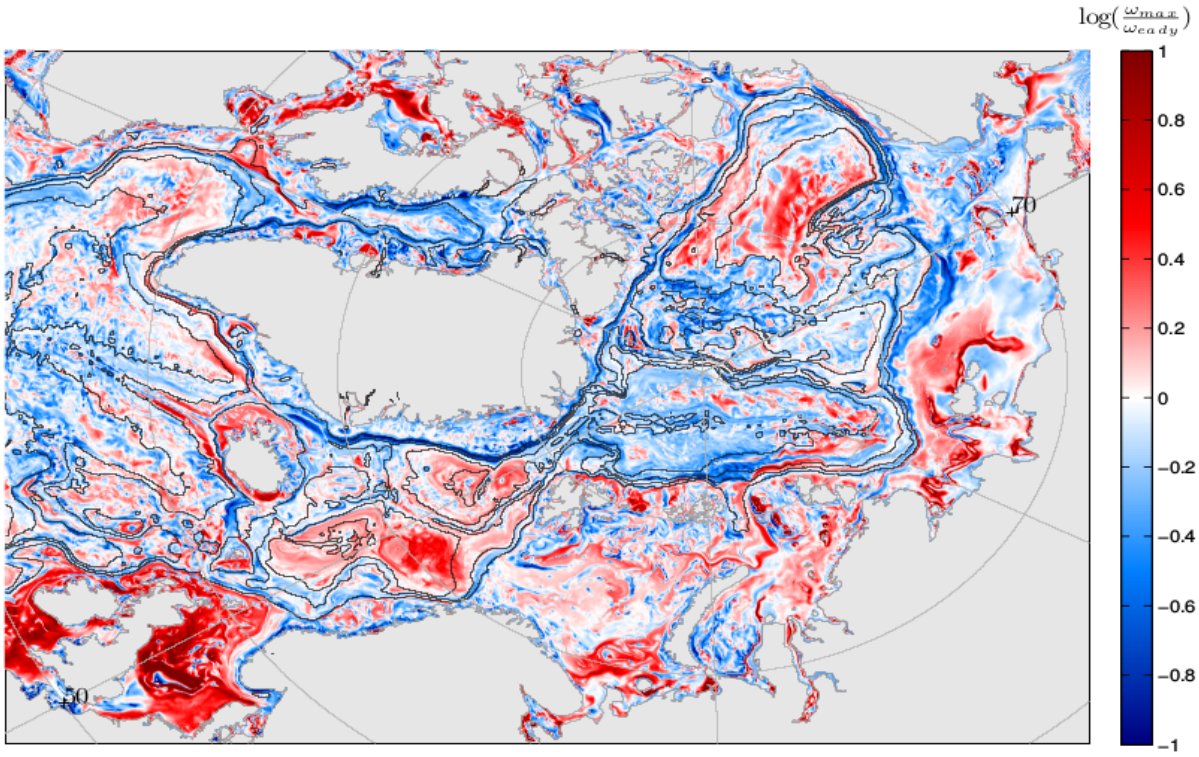

Figure 3.7: Maximum growthrates from the LSA scaled by the Eady growthrate.

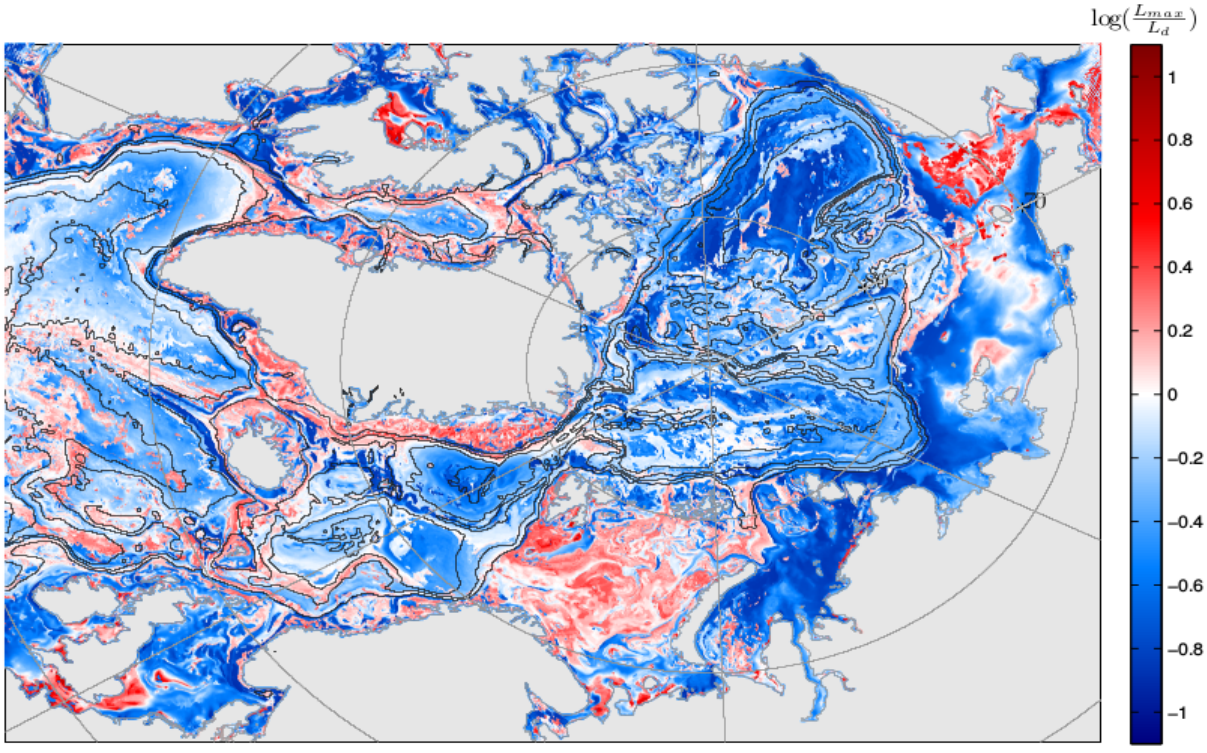

Figure 3.8: Lengthscales for the most unstable mode, scaled by the deformation radius.

Baroclinic energy transfer

We computed the energy conversion rate mentioned in section, shown in figure 3.6. We birefly comment on this here as we will come back to this later in the text. We takt note here tha the largest transfers happen aligned with the areas of greatest isopycnal slopes.

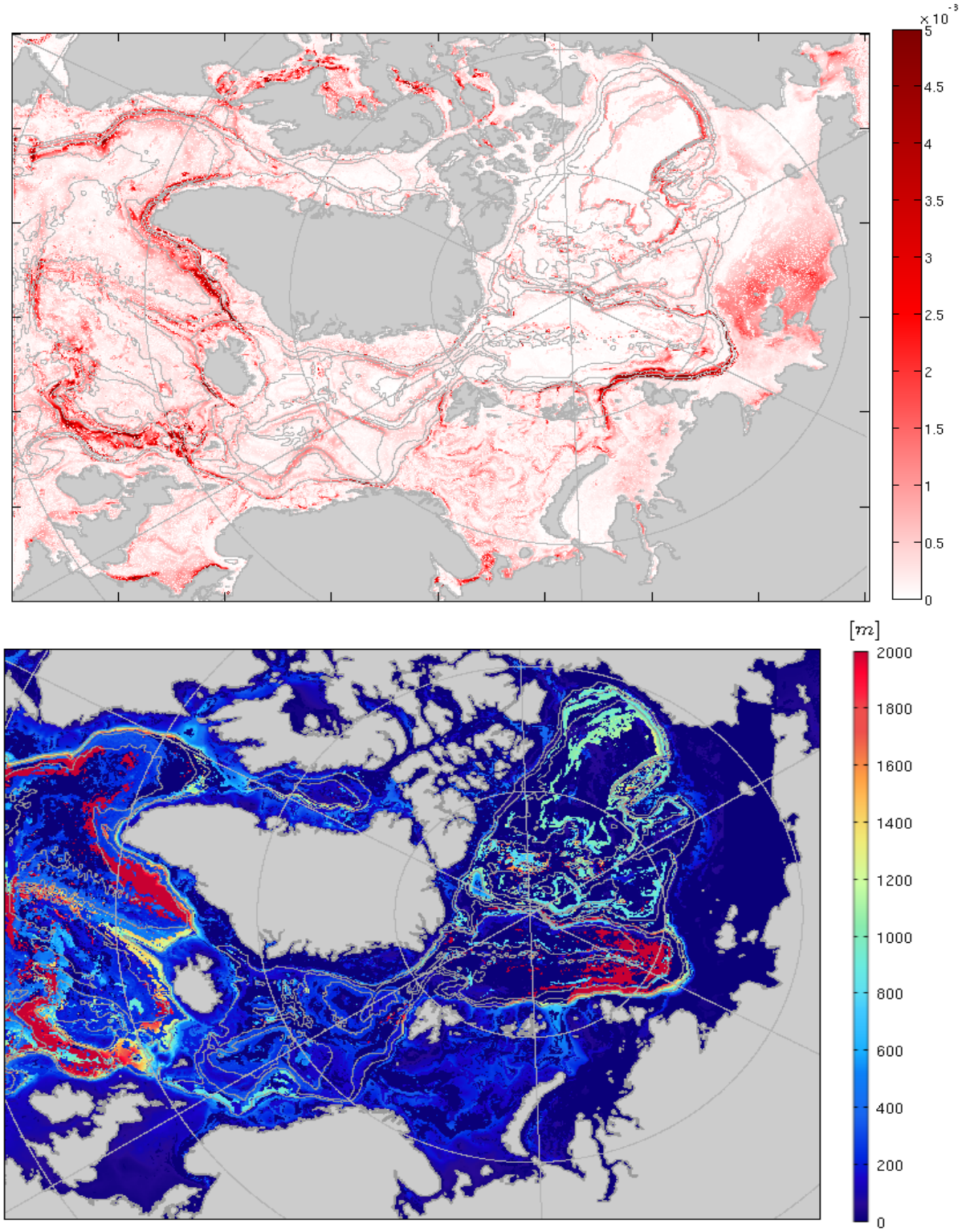

3.5.4 A closer look at the eigenvectors

In this section we look more closely into the detailed information the LSA renders at each locations. The incentive here is to attempt to classify the type of instabilities we find, and to look for indications if the assumption of Eady dynamics seem admissible. As noted, Eady instabilities are assumed in many parameterization schemes of eddy transport, while it is not certain that this is a dynamically valid assumption. Again, the setting in the Eady model is not very realistic for the ocean with amplitudes symmertric about the mid-depth. Since the stratification and velocity shears are typically intensified near the surface, the expected typical vertical profile have amplitudes more confined to the upper part, while noting that there can also occur bottom intensified instabilities. Tulloch (2011) puts forth a claim that the greater share of baroclinic instabilities can be classified as the Philips-types. We recall that this entails a sign-change with depth of the mean PV-gradient.

In our analysis, we investigated a multitude of locations within every part of the domain. Here we will present the results at two locations which serves to point out some of the typical findings. We can make a general statement about the broader picture we attained. On the basis of the locations we looked into, say that Eady-type instabilities are not a common feature. Our findings rather advocates that Philips- and Charney-type instabilities are more common.

The figures presented below show growthrates,ω_i, as a function of wavenumber. These were computed for the upper spectral plane of 201×101 wavenumbers, and then rotated to obtain the lower part. The dottet line signify the orientation of the thermal wind shear. The following plots depict characteristics for the most unstable wave, the vertical structure of the amplitude and the depth dependent wave-phase. The mean PV-gradient and the background velocities are shown, both rotated into the direction of the most unstable wave. This is done so that we can attempt to assess what we see by the necessary conditions for instability. Lastly, a vertical profile of the topography,temperature and isopycnals is shown.

The first column of plot belong to a point located in the Barents Sea, at $25.74^{\circ}E,\ 71.31^{\circ}N$. This location has approximately no topographic slope (or a slightly one), and can be considered a 'flat-bottomed'-case. The largest growthrates occur at $k/k_d \approx 2.5$. Furthermore is the fastest growing wave aligned with the thermal wind shear. This is what one would expect for an Eady instability, which indicates that the fastest growing wave here is goverened by Eady dynamics. The mean PV-gradient also implies this. The top and bottom contribution to the gradient is shown as the two short bars at the top and bottom. In this 'flat' case, the contributions essentially signify the top and bottom velocity shears. These need to be of the same sign to endorse an interacting Eady edge waves. We see that this criteria is fulfilled. Moreover is the amplitude is minimum at mid depths, and increasing toward the boundaries. The velocity profile is as in idealized settings more or less linearly increasing toward the surface. As anticipated for an unstable wave, the phase leads at the surface for an easterly sheared flow. The phase difference here is $\pi/2$, which is the phase shift that yields maximum growth in the Eady model. Despite having previously stated that an obvious classification of the modes as a specific type of instability, the wave characteristics at this location overwhelmingly points to an Eady type. All of the factors fits well with that Eady model. This result does not represent what typically has been found. However, we included it here since it was such a remarkable fit, and the constrast to the following steep-bottom case will serve us a point.

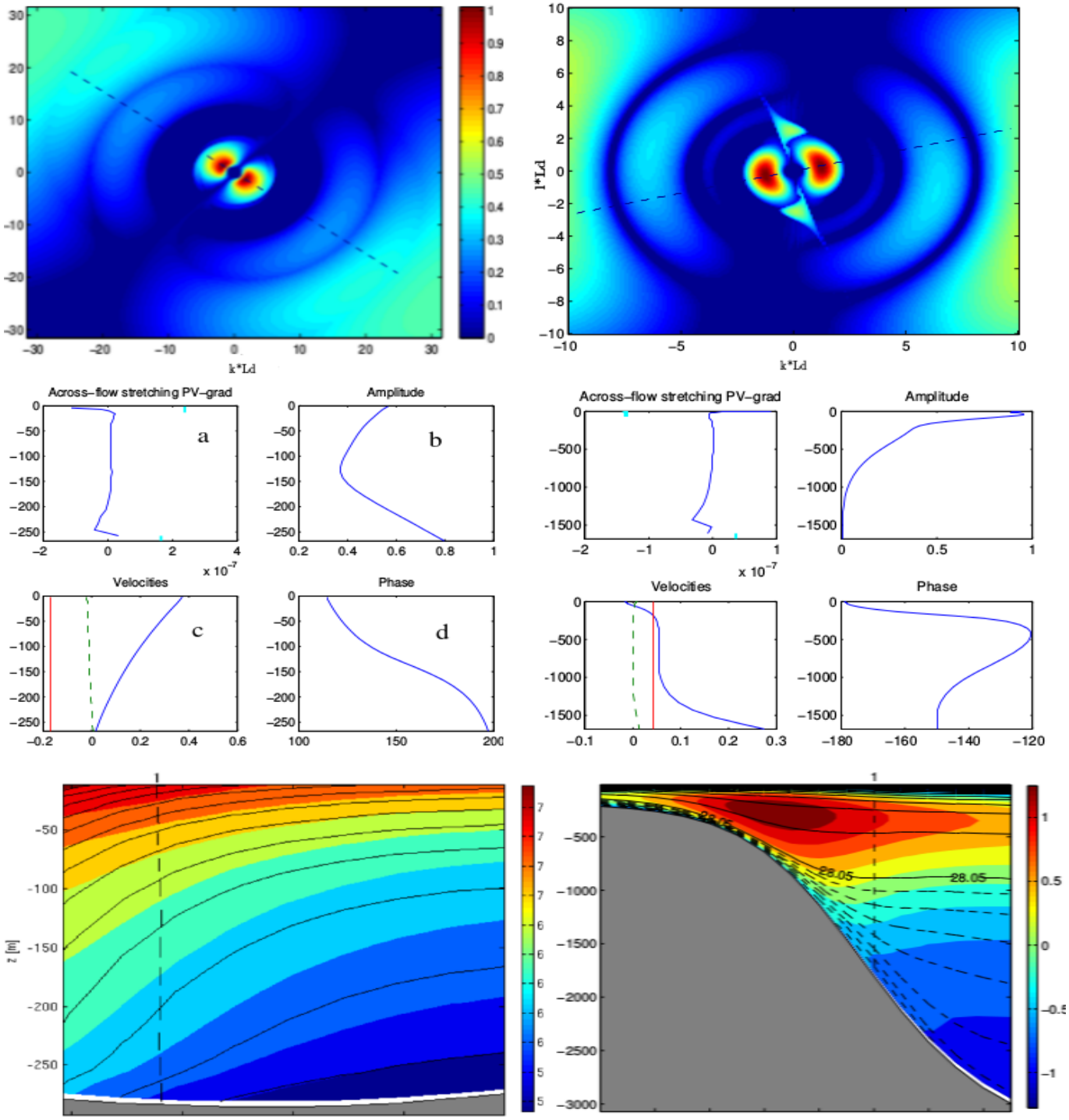

Figure 3.9: Top: Growth rates as a function of nondimensionalized wavenumbers $(k, l) \cdot L_d$. The dashed line is the orientation of the top-to-bottom thermal wind flow. Middle: Characteristics of the most unstable wave. The velocity in c) is rotated to be aligned with the most unstable wave, the dashed line in c) denotes $V \approx 0$. Bottom: A cross-flow slice of bottom topography, temperature and isopycnals. The dashed line indicate location of the selected point.

The next location was selected along the steepest topographic features north of the Fram Strait. The growthrate occurs also here at large scales, and is comparable to the last case, hence on the horizontal scale of the fastest growing Eady-type instability. The gravest mode is also here aligned with the thermal wind shear. This could again lead to the assumption that Eady dynamics might be able to explain what causes the instability. Nevertheless, when looking closer at the details, we realize that such an assumption will not be justifiable. The cyan-colored bars denoting the bottom- and top-contributions to the mean PV-gradient is of the opposite sign. This alone tells us that an Eady-like disturbance is not permitted by the charney-Stern-Pedlosky criteria. The negative top contribution, $\delta^{top} < 0$ simply reflects the negative velocity shear. The velocity-shear is the same at the bottom, however the contribution is positive there. In $\delta^{bottom} = \frac{f^2}{N^2}\partial_z \mathbf{U} - f\partial_y h > 0$, the bottom slope thereby makes a large contribution. Without including the term $\partial_y h < 0$, the contributions would be of the same sign allowing for potential edgewaves to interact. This illustrates how a bottom-slope can change the instability criteria.

Without the possible interaction of edge-waves, other interactions can however occur. The mean PV-gradient is positive in parts of the upper water column, and in conjunction with the negative top-contribution a Charney-type instability is possible. Additionally, the mean PV-gradient changes sign several times with depth, and a Philips-type instability is also relevant to consider. It is here instructive to examine the vertical structure of the wave's amplitude, as these two possiblities have different manifestations in with depth. The amplitude has its maximum at the surfas, falls off rapidly the top upper hundred meters, and then levels off to a monotonic decrease down to 1000m depth. The amplitude goes to zero at about the same depth as the isopycnals start to align with the approaching bottom slope. The slope of the topography and the bottom most isopycnal are of the same orientation, and appear to scale to approximately one. A stabilization for such a scaling is constistent with the modified Eady-model, where no instability is present for the slope-parameter of magnitude 1.

In a Charney-type instability the amplitude decreases exponentially from the surface maxima, this is an effect of implementing only one boundary. A condition is set that when the depth goes to 'infinity', i.e. toward larger depths here, the amplitude has to become zero. The characteristic amplitude of the Philips-type is also a somewhat rapid decrease with depth, albeit the modes are typically more deep-reaching. With this in mind, we might conclude that this mode resembles more the latter type.

Chapter 4

Statistics of the fully turbulent field

We start this section by a brief examination of the distribution of the full eddy kinetic energy (EKE) field in the model. This may serve as a first pointer to where we might expect to find high eddy activity. On the other hand, we note that EKE reflect all fluctuating motions deviating from a mean state. The mean state is predefined, and taken over a certain period in time or a limited spatial area. The EKE may therefore incorporate several types of motions depending on the way it is defined. High EKE-values may often just as well arise from fluctuations in currents speed or direction and as represent mesoscale eddies (Maslowski et al., 2008). In the following analysis, it could therefore be apt to compare the total amount of EKE in the domain versus the EKE associated with the detected eddies only. In this way we might be able to reckognize how much the coherent vortices contributes to the fluctuating part of kinetic energy.

By removing a temporal mean from the instantanous velocities, we are left with the eddying motions of the flow. The vertical component of the flow is commonly regarded as substantially weaker than the horizontal components. We thereby only consider the horizontal velocity components, assuming that: $\mathbf{v} \approx \mathbf{u}$, we make the subtraction

$$\mathbf{u}' = \bar{\mathbf{u}} - \mathbf{u}, \tag{4.1}$$

where $bar\mathbf{u}$ is the mean flow, and $\mathbf{u}$ is the model's daily output velocities. $\overline{EKE}$ per volume is then naturally obtained by $0.5\overline{u'^2}$. The overbar represents a mean over the same time period as applied to define the mean flow. Deciding on a suitable period for the time average is not trivial, but a reasonable estimate is motions occuring between a day to six months (Isachsen 2015). We have used a three-month average to filter out 'background' motions.

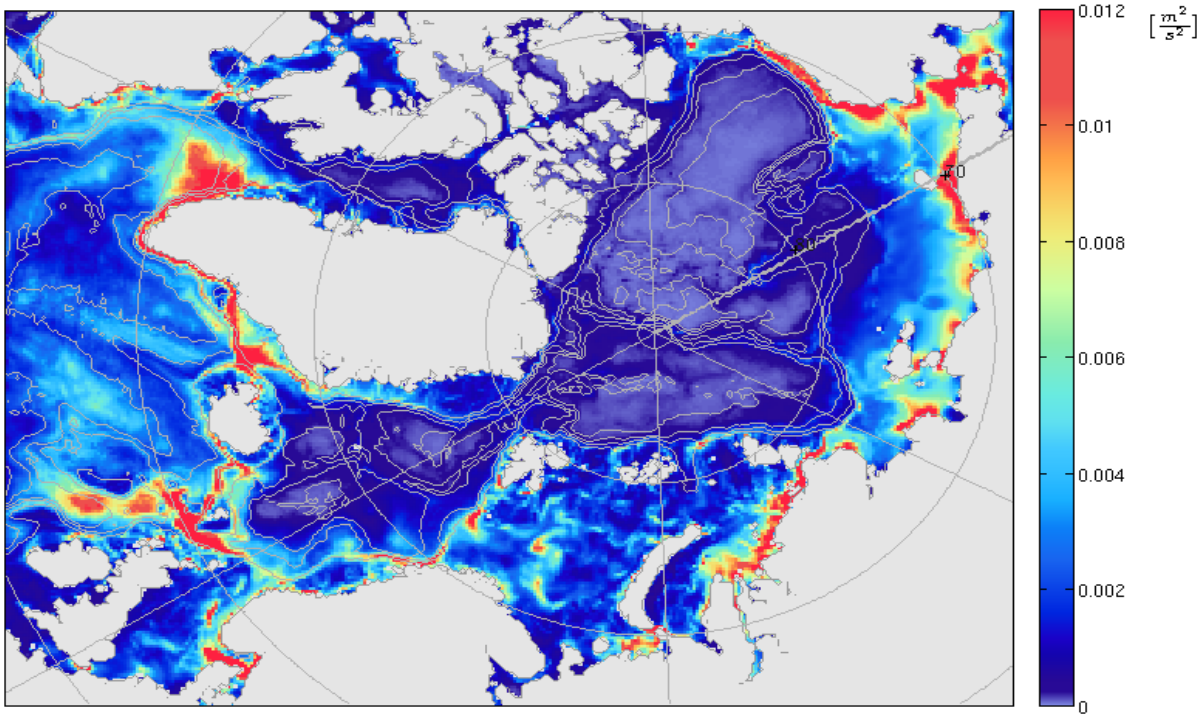

Figure 4.1: The Arctic4-model's 10 year mean, depth-averaged eddy kinetic energy field.

In figure 4.1 depthaveraged EKE values are shown. There is evidently an uneven geographical distribution of EKE within our domain. The central basins in the Nordic Seas together with the Arctic Ocean, appear to be subject to less variability than in most other locations. The inflow North Atlantic current (NAC), the easternmost branch in particualar, and the Iceland Faroe frontal zone, stand out as highly variable. The boundary currents along Norway and Greenland also show levels of high EKE. The EKE on the west side of Greenland is spread out into Labrador Sea. This region is known for its dense population of eddies. In fact, eddies have, from observational data, been reported in all the regions depicting elevated EKE. At the same time, these regions are also comprised of slender currents that frequently experience heavy meandering, that could also render this signs of variability. How large a portion of the EKE that can be attributed to coherent vortices, is one of the motivations for the following vortex analysis.

4.1 Autmatized eddy detection

Since the 1980s, several observational campaigns have focused on automatized eddy detection (J. Isern-Fontanet, 2003). In some of the early attempts, eddies were identified from changes in proxy ocean variables using infrared imagery. These proxies could be the color of the ocean, or temperatures at the sea surface (J. Isern-Fontanet, 2003). This is somewhat problematic, since these procedures rely upon changes in variables that are not directly linked to the eddies, but rather advected by the eddies. Several different processes impact such variables, and it may be hard to single out the changes that can be attributed to eddies.

Sea surface height (SSH) provided by altimetric data is however closely tied to ocean dynamical processes, and liably better suited for eddy identification. In the recent advances in satellite-measurements, increasingly detailed maps of the ocean surface have become available. Datasets from different satellites

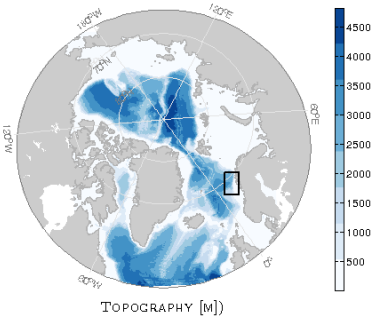

Figure 4.2: An algal bloom off the Norwegian coast. Satellite images offers coherent, synoptic maps of ocean variability. This image demonstrates how algal-blooms can reveal mesoscale ocean features. The picture show a vibrant eddy-activity, evident in the swirls which serve to both trap and mix these passive tracers.

4.2 Previous studies

The techniques can mainly be separated into two groups. They are either based on geometric or physical flow conditions. A physically based procedure, require detection parameters to exceed a prescribed threshold, whereas a geometrical conditioning entail an analysis of the pattern or curvature of sequential streamlines (Nencioli et al., 2010).

4.2.1 Physically based methods

Vorticity method

Mcwilliams (1990) conducted one of the earliest automated eddy detection investigations. He developed an algorithm to identify coherent vorticies in decaying two-dimensional turbulence at large Reynolds number. In a similar study, Thompson and University of California (2006) implemented a version of this method in combination with the OW technique. The census is realized by considering the vorticity field from a numerical solution. Defining vorticies by the means of vorticity alone does not guarantee the extraction of only vorticies. Other flow features also consist of high levels of vorticity. Subsequently, some regions satisfying the selection criteria may lack an eddy core. Hence (Mcwilliams 1990) refined earlier algorithms by a more stringent selection. Primarily two criterias identifies vortex-candidates from the structures that conform to a vortex. The first part entails what Mcwilliams call a 'pattern recognition or feature eduction', which detects connected regions of vorticity consisting of a single vorticity extremum. The local extremum is required to exceed value, specified to be 5% of the global maxima of vorticity within the domain. Secondly, the vortices are assumed to attain axisymmetrical shapes around this extremum. This idealized vortex-structure has frequently been observed in solutions of inviscid 2D turbulence. Such settings host isotropic horizontal flow fields, while a realistic setting in the ocean will consist of large scale shear and latitudinal variations in the Earth's rotation rate, which introduce anisotropy. Thereby, the characteristic axisymmetrical shape occuring for vortexes in 2D turbulence, may be a too strict criteria when applied to the ocean.

Okubo Weiss

The Okubo Weiss parameter is one of the most commonly used tools for identifying coherent structures. It has been employed in a number of observational and model studies in different parts of the World Ocean, as well as in global studies (Penven et al., 2005; **?**; Chelton et al., 2007). The Okubo-Weiss parameter(OW) originates from turbulence studies (Okubo, 1970; Weiss, 1991) and has commonly been utilized in two-dimensional turbulence studies((**?**)). It aims to localize regions dominated by rotation relative to deformation. It separates the flow field into locations subject to high rates of strain, and coherent rotating flow, associated with high vorticity of either sign. By a combination of strain and vorticity, the parameter takes the the form:

$$OW = S_n^2 + S_s^2 - \zeta_z^2 \tag{4.2}$$

where u and v are the horizontal velocity components, in the x- and y-direction respectively. The normal strain, $S_n = (\frac{\partial u}{\partial_x} - \frac{\partial v}{\partial_y})$, and the tangential stretching $S_s = (\frac{\partial v}{\partial_x} + \frac{\partial u}{\partial_y})$, together represent the total deformation of the flow,. The last term represent the vertical component of the relative vorticity, $\zeta_z = \partial_x v + \partial_y u$.

When OW is negative, relative vorticity dominates. This parameter is thus helpful to identify eddy boundaries, since an eddy core is likely to have negative OW values and regions around the core are often strongly deformed. The OW parameter is thus an illustration of the turbulent character of the flow, and eddies can be detected by the patches of negatively valued- encircled by positively valued OW (Penven 2005).
Despite the parameter's ability to systematize the flowfield, eddy detecting based on OW entails some deficiencies (Chelton et al. 2011, Nencioli et al. 2010, Williams et al. 2011). Firstly, an upper treshhold of the OW needs to be specified, for grid points belonging to an eddy-interior. This introduces an issue of deciding an admissable upper limit. A well-suited assumption is not obvious, as a single value might not be representable across regions (Nencioli et al. 2010). The issue of a

global threshold has been noted with concern in the studies utilizing OW as means for eddy detection. Global studies suffer the most in this regard. Polar regions are also especially problematic, due to the potentially small OW parameters associated with the small eddy-sizes. A typical choice of treshold has been $OW = -0.2\sigma_{ow}$ (**?**Petersen et al., 2013). σ_{ow} is the standard deviation of the Okubo Weiss parameter for entire domain. If this cut-off value is too high, the detection procedure will miss eddies of small scales. Additionally, if it is too low, large areas possibly including several eddies, may be characterized as one eddy. This results in false negative or positive detections (Chelton et al, 2011).

Secondly, the parameter is sensitive to noise related with its velocity inputs. In several studies, SSH anomalies are employed to estimate velocity components. These fields commonly contain a substantial amount of noise. Geostrophic velocities are computed through the relations

$$u = -\frac{g}{f}\frac{\partial h}{\partial y}, \tag{4.3}$$

$$v = \frac{g}{f}\frac{\partial h}{\partial x}, \tag{4.4}$$

is the Coriolis parameter. The calculation of OW, thus contains products of second order derivatives of SSH. The differentiation magnifies the noise initially present in these fields. Furthermore, a numerical solution will consist of finite difference forms, which also acts to amplifies the noise. A way to deal with the noisy fields has been to apply filters to the data, which are scale-dependent and thereby remove certain aspects of the flow (See app. Chelton).
We take note that whilst the OW is the traditional method based on physical criteria, other methods have been developed alongside it(). We shortly point out some of the other options, such as the 2D Wavelet method applied by Doglioli et al. 2007, and the somewhat rarer Winding Angle Method(Sadarjoen and Post, 2000, Chaigneau et al.,2008). The former, as in McWilliams studies, is based on the vorticity field (Doglioli 2007). The latter is based on the notion that eddy cores will be enclosed by circular or spiral streamlines(Robinson 1991, Necioli 2010). Studies which have compared the performance of OW up against these two methods, report that the two latter produce more accurate results. However, the applications are computationally costly. Since they also require velocity input, the same sensitivity mentioned present in the OW, will affect their performance as well.

4.2.2 Geometrically based method

Geometrically based methods have showed to be less problematic compared to the OW technique (Halo et al., 2014), and therefore in recent years been more preferred(Halo, 2012; Chelton et al., 2011; Souza et al., 2011). Nencioli et al.(2010) developed an eddy detection scheme based on the geometry of the velocity vectors. This was applied to a high resolution(1km) model product, and has further been utilized in a number of model studies. The method was validated against manual detection, and showed a high performance. 4 constraints are put on the configuration of the velocity vectors, and eddy centres are identified as all the locations which fulfill these criteria. The two initial criteria require that the velocity components in the x- and y-directions, need to reverse in a tranverse direction across the eddy centre, as well as decrease outward from the centre. Thirdly, eddy centres need to be the local minimum velocity point, and lastly a condition is put on the vectors sense of rotation. Due to the method's requirement of strongly accurate computations of rotational flow, its utility is restricted to highly resolved data. It has thence not been applicable to satelitte data with typically 0.25° resolution().

Contour based methods

Chelton et al(2011) concluded that, when SSH fields are required to attain velocities, detecting eddies merely by OW, does not yield satisfactory results. Their study rather advocates the use of an contour-based procedure. They analyze a global dataset of SSH fields, spanning 16 years. The aim of the study was to map and track mesoscale variability on a global scale. The data was attained from two merged altimeters (Le Traon et al., 2003), that rendered higher resolution data than used in previous studies (Chelton et al., 2007).

A procedure based on the SSH field has been applied in several studies(Chelton et al.,2007;Fang and Morrow,2003;Chaigneau and Pizzaro,2005). Such algorithms seek out peripheral closed SSH-contours. The justification for this lies in the assumption that the flow encapsulating eddies, is geostrophic and marks out streamlines which approximately collocates with closed SSH contours. An analysis built exclusively in terms of SSH, still demand a threshold to extract eddies,i.e. a lowest permittable deviation in SSH. Hence, the difficulties in arriving at an optimal limit remains. Chelton et al.(2011) developed an algorithm that avoids the requirement of setting any cut-off limits. Instead, a consequtive search at 1cm intervals is performed through sea level heights from -100cm to 100cm. Further conditions is set to filter out features which do not share the expected structures of an eddy. Restrictions are put on parameters such as the amplitude, size, and distance between any points inside the SSH contour. Chelton et al. claim that this outperforms the OW method, with being more resilient to noise and excess eddy detections. However, it has some struggles with seperating several connected eddies of the same polarity, in addition to the aformetioned issue with the handling of AVISO data.

4.3 A hybrid eddy detection method

For our statistical analysis, we chose to use a so-called hybrid method. It shares the major components of the one employed by Chelton et al. (2011), relying on both finding closed SSH-contours and the OW criterion. The code is based on a Matlab toolbox by Pierrick Penven (Penven 2005), freely available at *http://www.simocean.org.za/tooleddy.php*. It has been utilized in several other studies (Halo 2014, Raj et al. (2015)).

Syntaxwise, the code was rewritten to only depend on the internal matlab language. Other modifications to the code will be justified as we further work through the algorithm.

An overview of the algorithm can be listed in 4 main points:

1. The Okubo Weiss parameter is calculated from depth-averaged horizontal velocities aquired from the model. By using the model-velocities, and not geostrophic velocities computed from second-order derivatives of the SSH, some noise is avoided. A hanning-filter is however applied twice on the Okubo Weiss parameter in order to smooth out some grid scale noise. Eddy kinetic energy is also computed point-wise for the entire grid, by substracting a seasonal mean from the daily data, leaving us with the fluctuating(eddy) part of the motion.

2. The model provides daily values of the variable zeta, which represents the sea surface height. The surface-height field is extracted every 5th day, and local extremal points on the surface are detected. Anticyclones, associated with a minima in SSH, and cyclones, associated with a maxima in SSH, are evaluated seperately. In the original code, the verification of a minima- or maxima point requires that all 8 neighboring points, has a higher or lower value, respectively. The original algorithm by Penven however, is intended to compare results from a numerical model with the results from AVISO products, with a 0.25° horizontal resolution. For our purposes, a model field with 4 km resolution could then provide local extremal points seperated by only 4 km. As noted, the model simply will not be able to produce eddies of that size and seperation distance. Thus, the search is extended to the neighboring 24 points, yielding a shortest distance of 8 km between potential minima or maxima points. Furthermore, for every local extreme, we construct a surrounding subdomain. Starting at the centre, we then search for the largest closed SSH-contour around that point. This is achieved by looping through the contours, successively, with an increment of 1cm. The code originally uses 2cm, due to the limitation of altimetry precision.

3. Once a closed SSH-contour is found, we then search for a negative OW parameter within this sub-

domain. If no point inherits any negative OW points, the search is finalized and that eddy-candidate discarded. Otherwise, if there do exist gridpoints with a negative OW-parameter within the SSH-contour, the next step is to find the largest closed contour OW. The edge of the eddy is defined to be zero-contour of the OW-parameter.

4. Next, when an eddy is detected, properties such as area, eddy kinetic energy, vorticity, radius and amplitude are computed. The area is the sum of all area-elements which lies within the eddy-boundaries, expresses as:

$$ds = dx \cdot dy \tag{4.5}$$

$$Area = \int ds \tag{4.6}$$

The eddies EKE is computed by summing the EKE of all points within the eddy boundary, and weigthing this over the eddy's area.

$$eke = 0.5\sqrt{u'^2 + v'^2} EKE = \frac{1}{Area} \int eke \; ds \tag{4.7}$$

The eddies relative vorticity is attained by:

$$ds = dx \cdot dy \tag{4.8}$$

$$Area = \int \omega ds \tag{4.9}$$

The amplitude is calculated by subtracting the maximum and the minimum SSH-contour within the eddy-boundaries (see figure below). Expressed as:

$$Amplitude = \zeta(max) - \zeta(min) \tag{4.10}$$

Despite being a threshold-free algorithm, an aspect of the code is a collection of parameters set prior to the detection. A maximum allowable detected radius is set to 300 km (Chelton and Penven used 500km) to prevent an entire ocean gyre to be detected as an eddy. There is also a need to specify a minimum eddy radius, since the model is not fully resolving the eddy-field. The minimum radius was set to a value of 10km. The aforementioned SSH contour interval is set to 1cm, and lastly the number of times the Hanning filter is applied is set to 2.

Experiments with different sets of parameters showed little sensitivity to the results, as also found by Penven et al.2005. The decrease of 2 cm to 1 cm, brought the number of detected eddies up slightly, but did not change the statistical values.

Eddy tracking

A tracking algorithm was utilized, developedby Penven et al. 2005. Eddies across timeframes are linked through a similarity condition. Two eddies detected in two subsequent frames, are considered the same if the generalized distance is minimal

$$X_{e1,e2} = \sqrt{\frac{\delta X}{X_0}^2 + \frac{\delta R}{R_0}^2 + \frac{\delta \zeta}{\zeta_0}^2}. \tag{4.11}$$

The first term denotes the fraction of the spatial distance seperating the two eddies to a characteristic length scale specified by the user. In the following terms δR represents the difference in radius, and $\delta\zeta$ the difference in vorticity, over reasonable reference values. The reference values were set to

$$X_0 = 25km \tag{4.12}$$

$$R_0 = 20km \tag{4.13}$$

$$\zeta_0 = 10^{-5} \tag{4.14}$$

$X_{e1,e2}$ is set to infinite if the two eddies are of different polarity, to inhibit a change in the vorticity signature(Halo2013). The track gets obsolete also if the propagation distance between two timeframes is too long. A limit is thereby put on the eddy's translation velocity,$0.3\frac{m}{s}$, preventing unrealistic distances to occur.

Eddy temperature and salinity

Computations of the eddy core temperature and salinity anomalies were added to the utilized code. A typical year is created, comprised by daily means acquired from the 10 year model simulation. The anomalies are thereby attained by subtracting the mean values from the temperature and salinity of the eddy centre. This serves as an indication of whether a detected eddy is more bouyant or denser than its surroundings. Such information is of great importance, as it can highlight the potential role played by eddies in fluxing heat-, salinity either

onto the shelfs or basinward.

Snap shots of relative vortivity and Okubu Weiss

The figures presented below illustrate two of the parameters that take part in the eddy detection scheme; the relative vorticity field and the OW parameter. The fields are snap shots from 1st of January, 2000. We can reckognize most of the spatial pattern we saw in the EKE fields introduces at the beginning of this chapter. Most regions of high and low activity are located at the same places. Take note the resemblance of these two fields also. As it is with the EKE field, these parameters also 'picks up' other flow features than merely rotating structures (-encircled by strain when regarding the OW). An example of this is at the southern tip of Greenland. The vorticity here depict neighboring, elongated filaments of negative and positive vorticity. This is a reflection of the strong current hugging the coast there. The negative vorticity nearest the coast illustrate that the velocity is decreasing toward the coastal boundary, from the currents core-maximum further out. The water then attains an anticyclonic(clockwise) rotation, i.e a negative sign in vorticity. The opposite is true basinward from the currents core maximum. A decreasing velocity from right to left induces a cyclonic rotation, and hence a positive vorticity. This feature is also prominent particularly along the Labrador Current and the NwAC, but it also occurs along the entire rim current and elsewhere. We take note that the vorticity-sign of the currents meander will impact the characteristics of the eddies' cores, as they wrap around fluid when they are generated. Light waters are located near the coast, and becomes denser toward the basins. Assuming a current meander results in an eddy, then if the meander occures clockwise, i.e toward the shore, an anticyclone will wrap around buoyant waters. Oppositely, if the meander occurs cyclonically, then a cyclone appears and wraps around denser waters.

The OW parameter does not have the same widepspread feature, as it is more liable to identify coherent vortices. However, we do see, also here, the tendency of elongated filaments at the tip of Greenland. The boxed regions on the maps are zoomed in, and shown at the lower rigth corners. Here, we see an example of how the OW parameter detects circular, negatively valued features, which are the regions dominated by rotation. Also, the positive(red) values denote the strain, and is wrapping around many of the negtive(blue) areas. We can clearly indentify three large structures that stand out. These are likely eddies. Furthermore, in the vorticity map, the two northernmost eddies can be characterized as anticyclones with the negative vorticity, and the last eddy as a cyclone due to its positive vorticity.

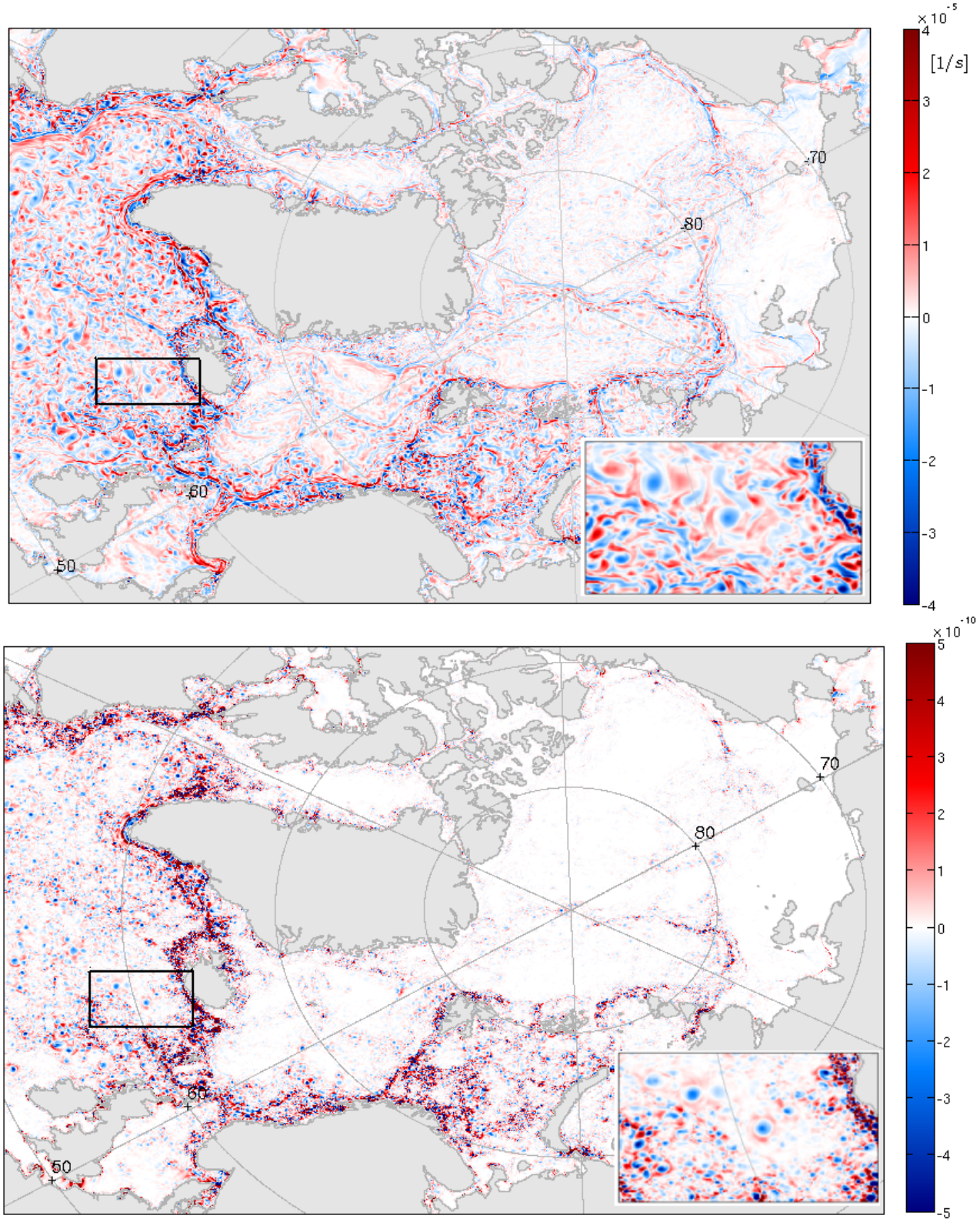

Figure 4.3: Top: Vorticity field. Bottom: Okubo Weiss parameter field. Both attained from depthaveraged 10 year mean velocities.

4.4 Results

In this section, we will present the results from the eddy detection. We have chosen to focus on the eddy characteristics for all the detected lifespans, and not a selected timeframe as done in a number of other studies(Chelton et al. 2007; 2011). The basis for this is that the shorter lived eddies, migth be developed or developing eddies, before the detection algorithm is able to identify them. In addition, we recognize that the tracking-algorithm might have shortcomings, and thence do not necessarily 'hold on' to the all of the eddies during their entire lifetime.

We treat eddy characteristics from the detection procedure in a Eulerian manner, where we consider eddy characteristics received from each timeframe with a 5 day interval. Inferred eddy properties and densities are aggregated on an regular grid of 20×20km. All eddies occuring within each box are then collected, and the average value of the respective characteristic represent that area.

4.4.1 Geographical eddy density

We will start by considering the geographical distribution of the detected eddies. Previous studies, utilizing observations and simulations, have confirmed the presence of eddies in all parts of our study domain(Rodionov 2004). In the proximity of frontal zones and boundary currents, regions of high eddy activity have been exihibited (Rossby et al., 2009). In addition, the Lofoten basin and the Labrador Sea off the westcoast of Greenland, are known to host maximum eddy activity in the Subarctic Seas. We therefore do not anticipate a homogenous map of eddy counts in the Subarctic Seas, but rather that eddy densities differs regionally. Expected findings in the Arctic Mediterrenean are more uncertain, as it is a particularly problematic area in terms of correct model simulations. As stated by Timmermans et al. (2008), there is generally a lack of long-term measurements taken in the Arctic Ocean, which are invaluable for our understanding of the eddy field there, and important for discerning the fidelity of model simulations.
Observational studies and high-resolution regional models have found several parts of the Arctic rich with eddies(Timmermans et al. 2008, Manley hunkins 1985, Hansen and Meincke (1979), Zhao et al., 2014, D'Asaro (1988)). Manley and Hunkins(1985) participated in the first mesoscale eddy survey in the Arctic Ocean (AIDEX), and reported finding 127 eddies during a 14 month time period. They suggested that, at any time, 25% of the surface area in the Canada basin is occupied by eddies. A common perception is that the south part of the Canada Basin is host 100-200 small-scale eddies (Newton et al. (1974); Manley and Hunkins, 1985; Spall et al. (2008)) supplied by the Chukchi Sea.

Figure 4.4 depict a map over eddy densities, which simply are the count of eddies within 20×20km boxes. White areas signify regions where no eddies were identified during the ten years simulation. Most notably, very few eddy occurences are seen in the central Arctic Ocean away from the shelf seas. We suspect that the model is not capable of resolving the small eddies present in the upper layers, of diameters around 10km (Timmermans 2008, Manley and Hunkins, 1985). Larger eddies with scales of 25 km have been observed deeper down in the water column, at the depths of the core of the Atlantic water, $800m$ (Timmermans (Timmermans)). A concern is also that these eddies might not produce a surface signal and then not letting the detection-routine discern them.
Apart from the Arctic Ocean, we find an overall sparse distribution of eddies in the central Norwegian, Iceland and Greenland basins, and higher counts in the enclosing areas. Some broad eddy rich areas are evident the Irminger Sea, the Labrador Sea off the westcoast of Greenland, and around the Lofoten basin. The southern part of the domain, depicting the inflow from the North-Atlantic, contain a significant amount of eddies as well. The branches of inflowing AW, possibly advect some eddies with origins in the NA. It is likely that some of these stem from the NAC, and are advected into the domain.

Other areas appear to have more concentrated distributions of high eddy population, such as the

Iceland-Faroe frontal zone and the Polar Front in the Barents Sea. This is also exhibited close to the NwAC offshore the coast of Norway.

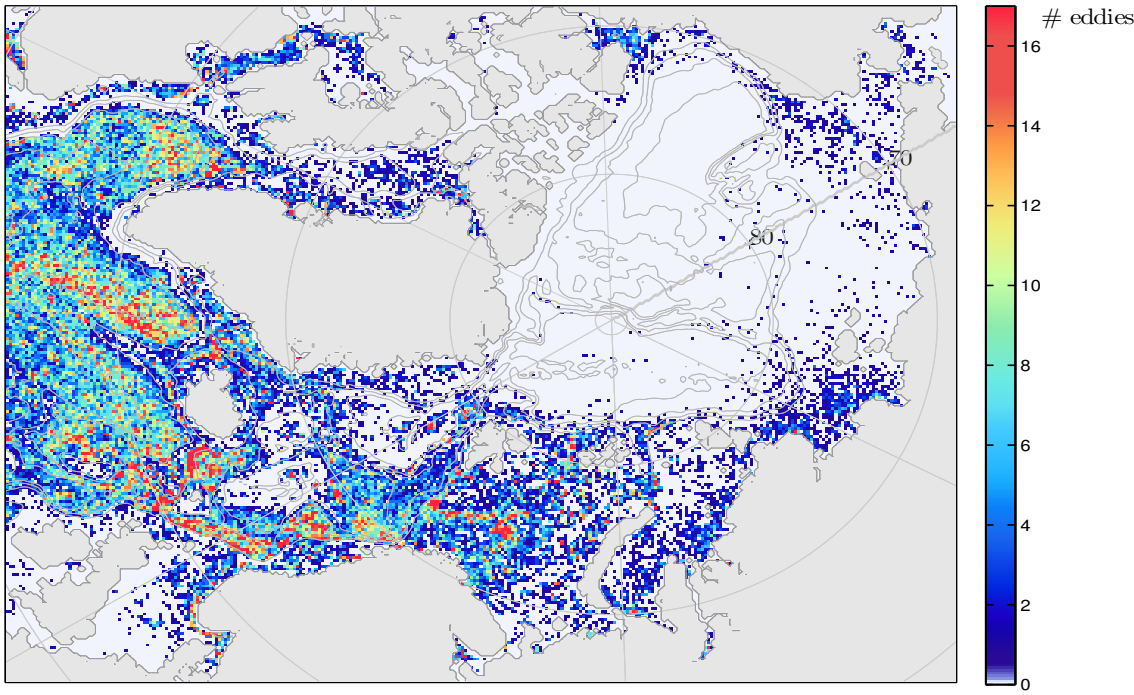

Figure 4.4: Eddy counts within 20×20 km boxed areas.

4.4.2 Eddy kinetic energy

We continue by comparing the map over the detected eddies kinetic energy shown in figure 4.5, with the total EKE figure 4.1. The strong consistency between these two maps implies that the eddies largely account for the total EKE. We take note that the EKE is not uniformly distributed. Concentrated bands of high EKE emerges mostly in association with boundary currents or frontal zones, and the areas of low EKE are more widespread. There is a strong coherence between the spatial patterns on the two maps. Still, figure 4.5 generally depict larger values of EKE, than for the total amount of EKE in figure 4.1. The Labrador Current, the flow out of the St Anna through, the WSC and along the Norwegian coast are found much more energetic when only considering the eddies' EKE. When averaging over the kinetic energy that encompasses *all* eddying motions, less energetic features are also included. In comparison, the averaged EKE associated with the eddies only, likely include more intense features. This may serve as a possible explanation for the higher values found in 4.5.

The Arctic Ocean, the central Norwegian- and Greenland basins and the Icelandic plateau, are the regions of lowest total EKE. These locations are collocated with the most pronounced white areas in 4.5, also reflected in figure 4.4. If the total EKE is associated with eddy activity, a coherence between regions of low EKE, and few eddy counts is indeed expected. Furthermore, the eastern-most flank of the NAC is higher in EKE than the other two inflowing branches. The central Labrador basin, as well as the Iceland-Faroe frontal zone and the Denmark Strait, are eddy active regions. The zone of elevated

EKE is broadened there.

The reasons causing the broad, high EKE at these locations are thought to differ. The currents surrounding the central Labrador basin exhibit large gradients of eddy fluxes, and this may indicate that eddies are primarily advected into the area(Lilly and Rhines, 2002; Prater 2002). At the Iceland-Faroe Frontal zone, advection of eddies is not perceived as the main cause for the raised EKE levels, but rather that eddies are generated there locally(Jakobsen 2003). The Denmark Strait is also believed to form eddies locally.

The Barents Sea appears to host a sustantial amount of eddy activity, evident in both figures. Energetic eddies are found along the pathway exiting the Sea through the St. Anna trough. This is not as clearly displayed in the total EKE. Neither is the energetic eddies, found near the West Spitsbergen, mirrored in the total EKE. Along the coast of northernmost part of Norway, and also of the Kara Sea, eddies and the EKE fields are intense. Additionally, the entire path of the NwAC has high EKE. This is, of course, consistent with it being baroclinically unstable as seen in the previous chapter.

There is broadly a good accordance between the distribution of the EKE and growthrates. The most unstable growthrates however comes out as a more grainy field than the smooth EKE field. Venaille et al. (2011) remark that "These regions of fast growth mostly reflect the fine-grained structures of the mean flow and the localized regions of instability." They further suggest that these differences are likely caused by advective effects. The linear stability analysis(LSA) only localized the initial posistions of instability and growth, but eddies can propagate or be advected away from their source regions. This is captured better in the EKE field, and it seems that this act to smooth out the highly localized regions yielded in the LSA.
We also anticipate that the maps over the distribution of eddy kinetic energy and eddy density show similarities. When comparing the spatial patterns with eddy density, we both find some agreement and disparities between the distributions. One clear difference is evident in the Irminger Sea, where the eddy count is high, whereas the EKE is not. The heightened EKE found around the southern coast of Greenland do not show up in the density distribution. Quite contrary, this area as well as a band in the western Labrador Sea, is mainly void of eddies. It is plausible that the EKE at these locations, is linked to fluctuations of the local energetic boundary currents. We recall that in the linear stability analysis, we found high growth rates at both these places, but length scales down to 2 km. It could be that the instabilities occurring are to small for the model to resolve. On the other hand, when investigating the SSH-contours in these 'white' areas, we see no closed contours in these regions, only steep gradients toward the coast. This coincides with the elongated features we saw in the vorticity, and partly the OW-field. If there are eddies advected, for instance along with the EGC around the tip of Greenland, appearantly very few eddies survive these high rates of strain.

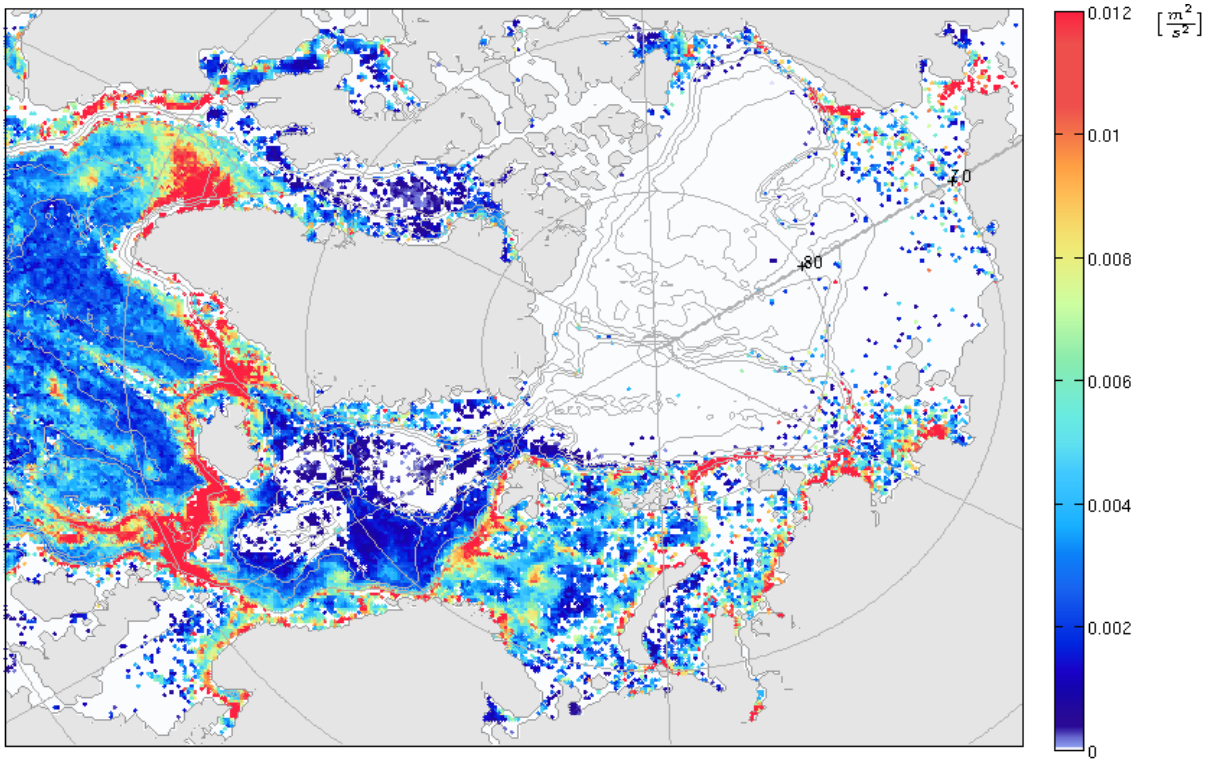

Figure 4.5: Eddy kinetic energy of the detected eddies.

4.4.3 Eddy radius

The top figure in figure 4.6 shows the effective radius of the detected eddies, $R = \sqrt{\frac{A}{\pi}}$, as defined in section 4.3. We notice that the branches of inflowing AW systematically contain bigger eddies, at about 25-35 km. Similar sizes are detected sporadically in patches elsewhere. The spatial pattern otherwise typically correspond to smaller eddies along the coasts and larger toward the basins. We take note that the smallest scales are restricted to 8 km.

How do the eddy radius inferred from the fully nonlinear eddyfield compare with the linear length-scale predictions? Before presenting the results, we take a brief look at what we might expect to find in the light of some earlier studies. The studies only provide implications, seeing that most global studies only extend up to 60°N. From AVISO data, Scott and Wang (2005) and Tulloch et al.(2011) examined the energy injection- and equilibrated eddy length scales, as well as kinetic energy spectral fluxes between them. They assigned the length scales related to the peak of the energy spectrum to the equilibrated eddies. Both studies revealed an appearant tendency for the for all three length scales to be larger than the deformation radius at high latitudes, and lower at low latitudes. L_{bci} from a global LSA, was found to be within a factor of 2 of the observed spatial scales at all latitudes, and both varied less with latitude than L_d.

Another study (Stammer 1997) found that zonally averaged eddy scales, derived from sattelite altimetry, were larger than L_d, but that the latitudinal change of the two, was linearly related. La Traon(1993) had previously noted that the observed eddy sizes varies latitudinally by a factor of 2, while the L_d varies by a twice as much. A study in the North Atlantic, utilizing drifter data, also found the linear relationship(Smith 2000).

The middle figure of 4.6 display the Rossby radius of deformation, and the following plot the radius of the detected eddies scaled by the Rossby deformation radius. It is evident that the 'observed' radius is universally larger than L_d, in agreement with other

studies(Stammer 1997, Smith 2007, Tulloch 2011). Away from the coasts, eddy sizes scale to a factor of 2-4 larger than the L_d. The largest contrast is seen in the Barents Sea, and certain areas along the the coast where the detection results are more than 10 times larger. One possible explanation could be that these differences are exhibited in shallow areas, and we recall that the $L_d = \frac{\int_{-H}^{0} Ndz}{f_0 \pi}$, is strongly a function of depth. In shallow regions, even for very stratified waters, L_d will take on substantially smaller values than at larger depths.

The spatial scales from the LSA agrees well in the Barents Sea, and elsewhere were mainly smaller than Ld or L_{eady}. The scales of the fully developed eddyfield is thereby also universally larger than the scales of maximum instability. This is a strong indication of that linear analysis do not provide well-estimated predictions of eddy lengthscales. Other studies (Chelton et al., 2007; Stammer 1997; Smith 2007) find globally that observed eddy-scales are uniformly larger than the lengthscales of linearly unstable waves. Smith mentions alternative reasons for the dissimilarities. One concern lies in the selection process of the most unstable mode in the LSA. Besides the quickly growing large, often deep instabilities, there are also small surface-intesified instabilities rapidly growing. These may occur at the same point of evaluation. The larger instabilities are generally believed to be larger contributors to the energy transfer, but we may fail to capture them at each location. Another compelling explanation which is consistent with these findings, is connected to the nonlinear stage of the eddy evolution. The notion is that energy is cascaded toward larger scales by nonlinear interactions, which may create this gap between the initial and final sizes. Scott and Wang (2005) has provided observational evidence for a strong inverse cascade in the ocean. On the basis of this, and the findings of a nonlinear baroclinic study (Smith and Vallis 2002), Smith et al. (2007) claims that a nonlinear energy cascade seems imperative to account for the observed spatial scales.

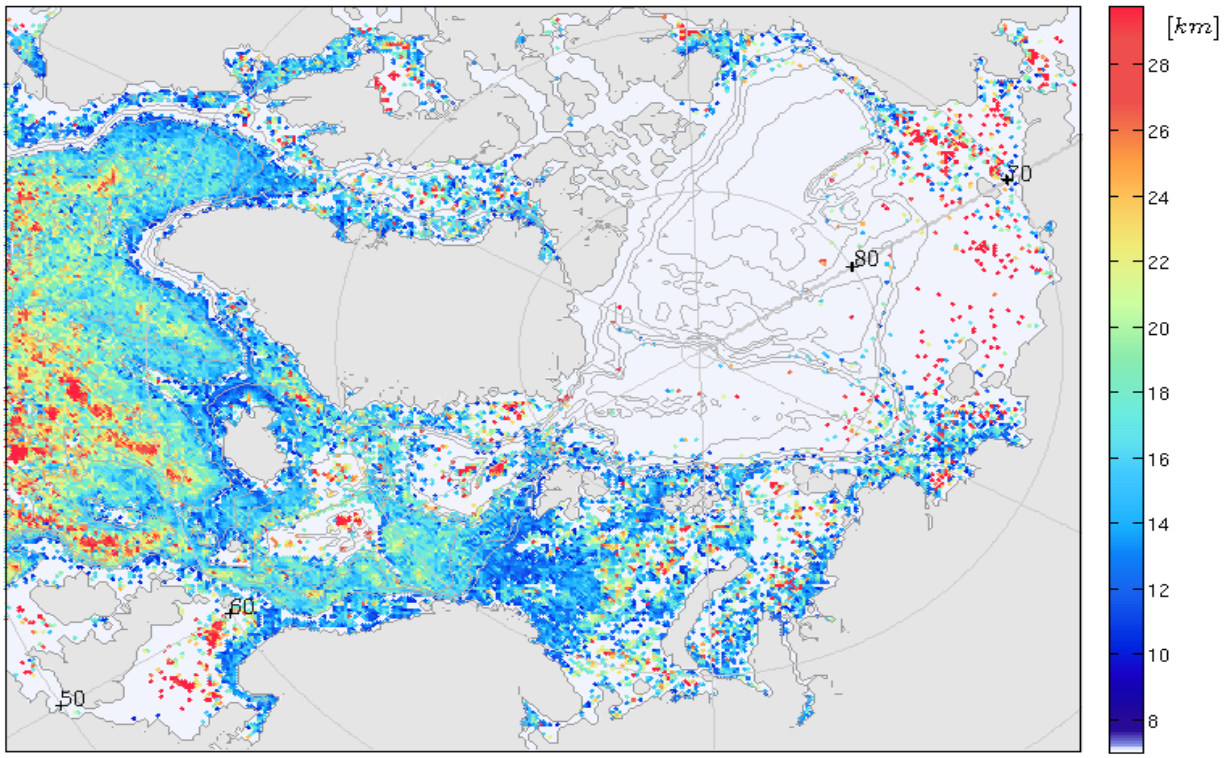

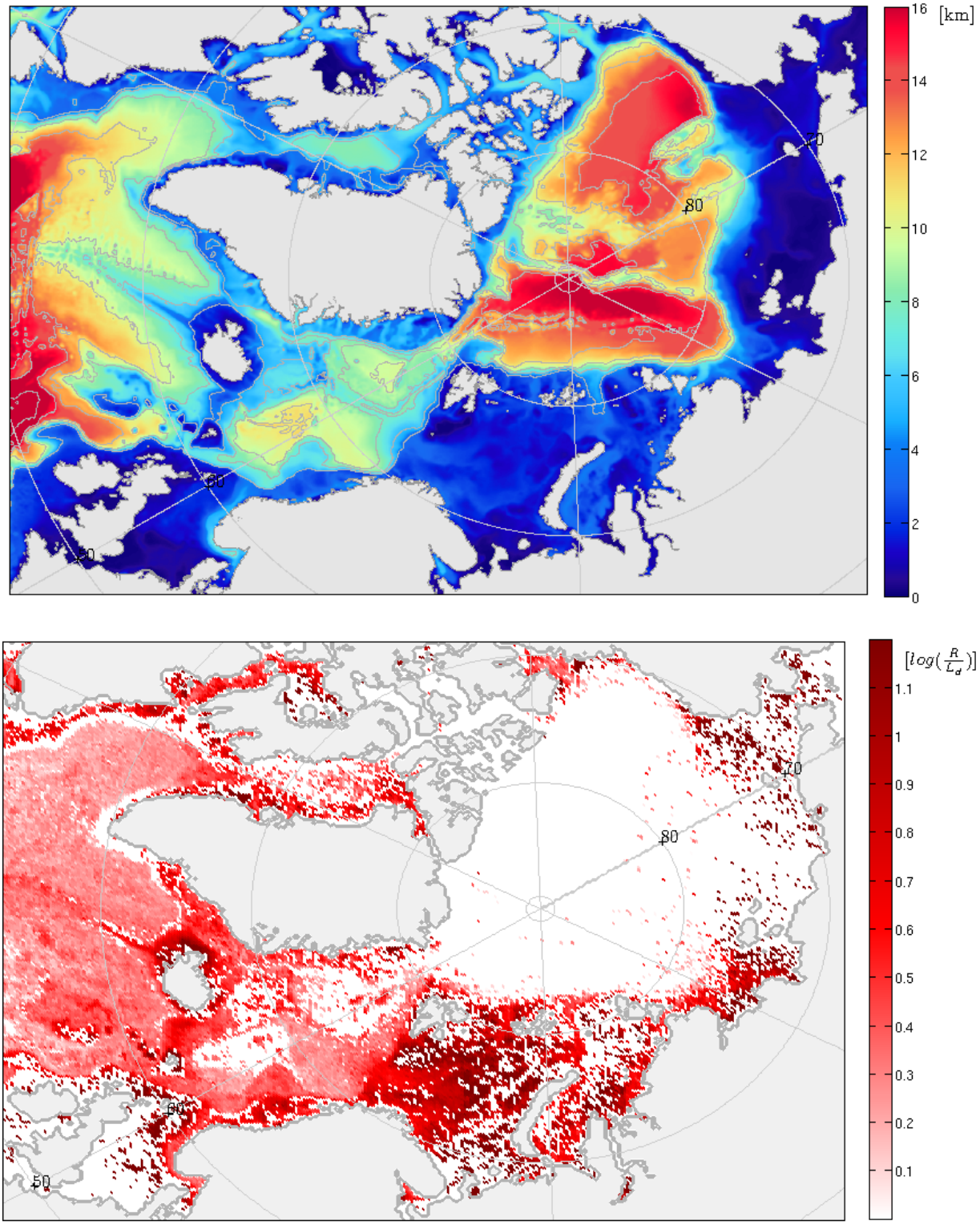

Figure 4.6: Top: Radius of the detected eddies averaged in 20×20km boxes. Middle: Rossby deformation radius,L_d, computed by the WKB approximation. Bottom: Eddy radius relative to L_d.

4.4.4 Cyclones versus anticyclones

Next we examine the eddy properties with respect to their sense of rotation. Are there any distinctions in the properties related to eddies of different polarity? As it is, assymmetries are indeed found in their spatial distribution and characteristics. These are often finite Rossby number effects. We start by an inspection of the asymmetries of the cyclonic and anticyclonic eddies' geographical distribution.

Of the total number of eddies detected, 54% are cyclones and 46% anticyclones. Figure 4.7 reveal a peculiar pattern in the partition of anticyclonic and cyclonic eddies in the domain. The maps show the fraction of eddies of either polarity, the number of eddies relative to the number of total detections. In some parts, high fractions of anticyclones and cyclones appear in vacillating bands. This is especially noticeable within the Norwegian Frontal Zone. Also, solely anticyclones inhabit the shallow part of the Icelandic Ridge with adjacent bands of a cyclones. On closer inspection, we can readily see that the cyclones generally have a larger tendency to occur near the boundary currents throughout the domain.
The plots imply that at some locations a larger amount of anticyclones find their way into the basin. Less cyclones escape the boundary currents, and are probably rather advected along the coast or trapped.

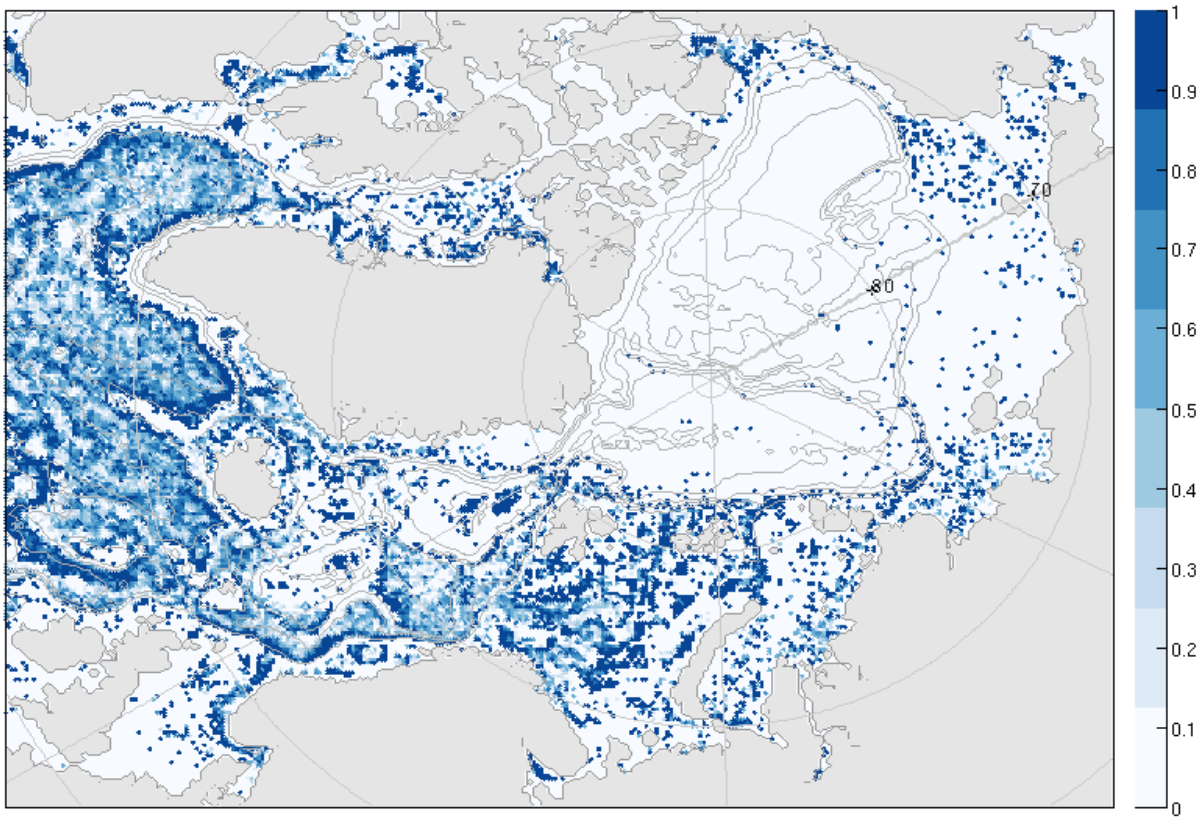

Figure 4.7: The number of cyclones over the total amount of eddies.

Property histograms

The histograms in figure 4.8 a)-d) depict density distributions of different eddy characteristics resulting from the eddy detection run. The red colored bars represent values associated with anticyclones, and the blue bars represent cyclones.

In figure a), the sizes of all detected eddies is shown. The anticyclones are found to attain a slightly larger radius on average than the cylcones. The mean radius for each polarity, represents all identified eddies, regardless of location. Anticyclones retain

a mean radius of 17.7km, and the cyclones one of 16.2km. The larger attained eddy-sizes are more frequently attributed to anticyclones, and the lower distribution is dominated by a greater number of cyclones. The positive skewness of the distribution imply that a larger amount of smaller than average eddysizes are likely to occur.

The histogram over eddy vorticity, tend to the same shape as the radius distribution, in that high extreme values occur less frequently. The intensity of anticylones versus cyclones do not significantly differ. There is however a tendency for cyclones to attain slightly higher vorticities.

The Rossby number ζ/f serve as an indicatication of how well the geotrophic approximation apply to the eddies. Mesoscale eddies are usually assumed geostrophically balanced (McWilliams, 2008). However, at high latitudes where the eddies are smaller, some on the verge of entering the submesoscale regime, this assumption may not be fully adequate. Toward smaller scales, the Coriolis force start to become less important, and an advective (centrifugal) term is needed to balance pressure gradient term. the validity of the geostrophic approximation relies on the condition that $\zeta/f << 1$. We find that 90% of the eddies we register, have a Rosby number lower than 0.2, and we can conclude that a geostrophic assumption is largely valid within an error of 20%. Even so, centrifugal and ageostrophic effects might have an impact their evolution (Chaigneau and Pizarro, 2005).

The ability for eddies to trap fluid in their cores, can be measured by a nonlinearity parameter U/c (Chelton et al. 2011). U denote the maximum rotional speed of the eddy, and c is their propagation speed. We attain the rotational speed by $\frac{1}{2\pi A}\int_{Area} VorticitydA$. The propagation speed is computed simply by the distance between each position along the eddy track, divided by the time between each recorded position (here 1 day). $U/c > 1$ indicates that fluid is trapped within the eddies, since the rotational velocity exceeds the translation rate (Chelton 2011). This means that the fluid will be carried by the eddy along its propagation. The parameter is also usefull to distinguish eddy features from linear waves, seeing that the latter cannot trap fluid. From figure d), we can see that most of the identified eddies have a nonlinearity parameter greater than 1. This is consistent with the findings of Chelton et al. (2011) who found that practically all of the eddies they detected outside the tropical regions were nonlinear.

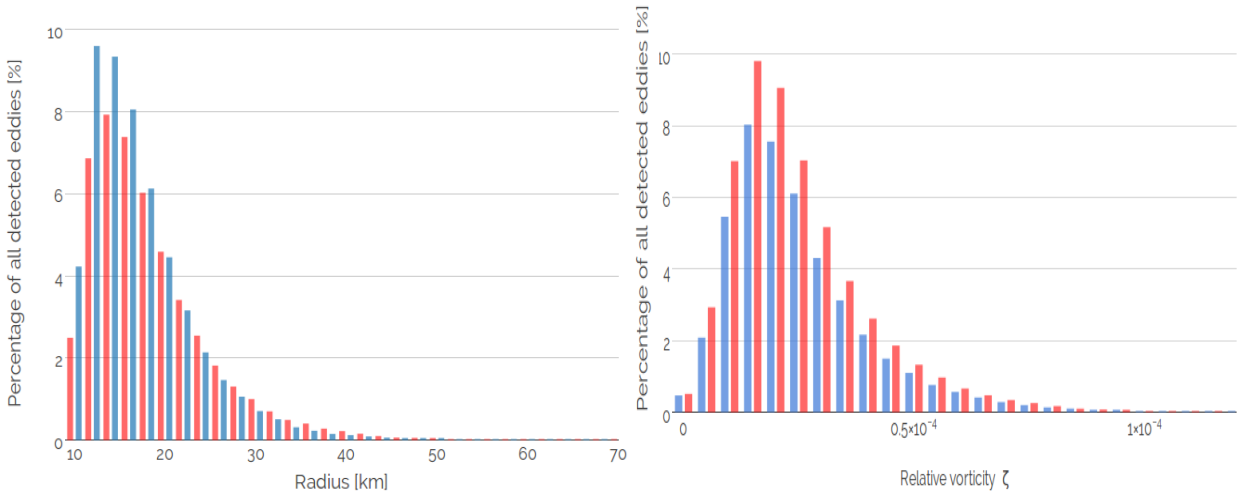

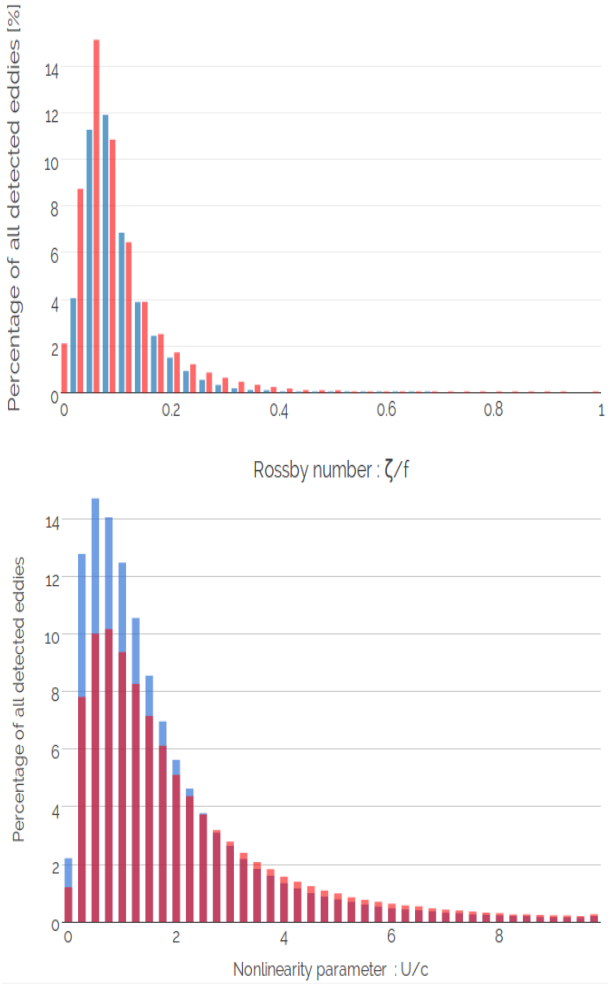

Figure 4.8: Blue bars denote cyclones and red bars anticyclones. a) Histogram of the radius of the eddies, in km. b) Relative voicity c) Relative vorticity scaled by the Coriolis parameter, f d) Nonlinearity parameter U/c.

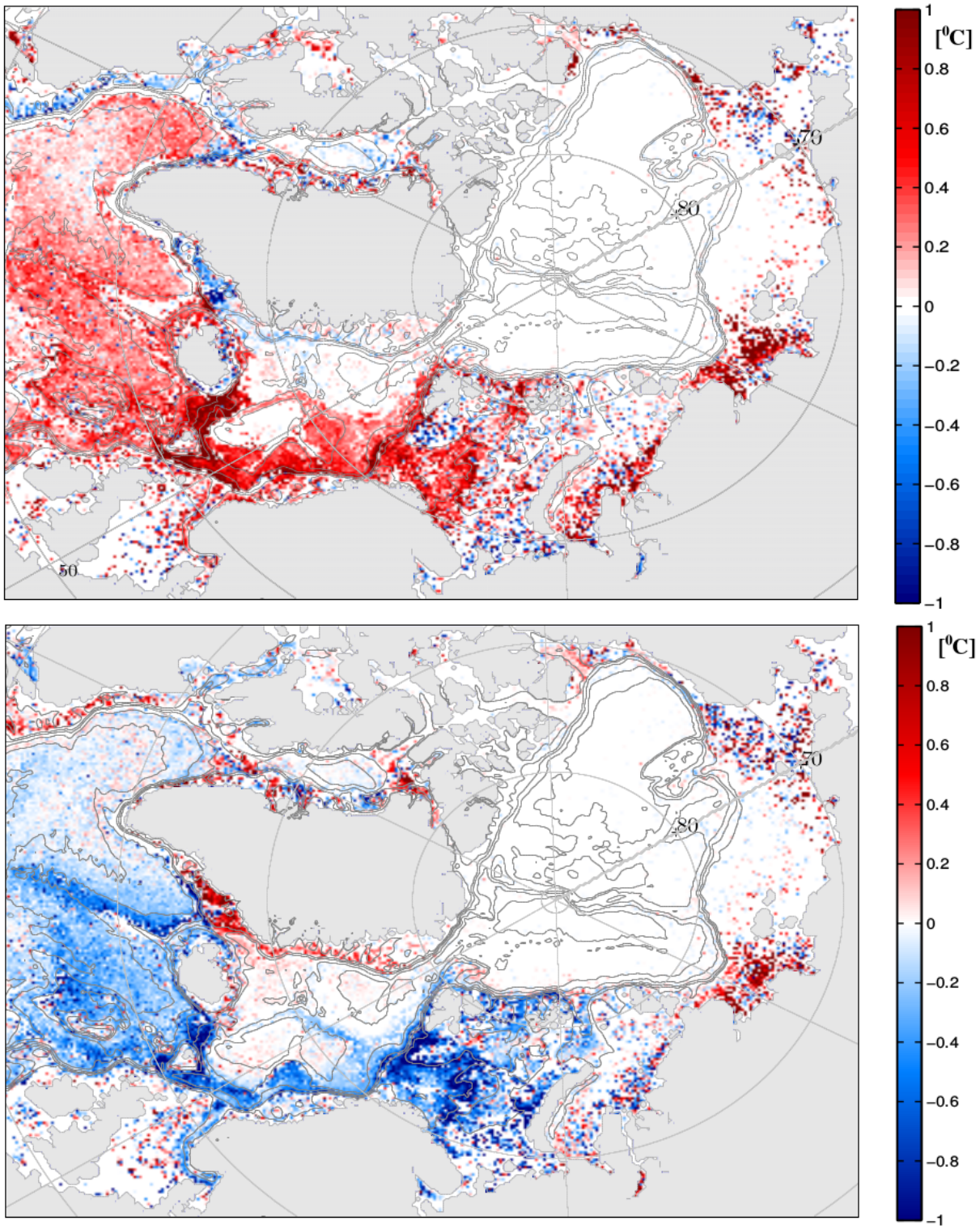

Figure 4.9: Top: Temperature anomalies for anticyclones. Bottom:Temperature anomalies for cyclones.

Eddy temperature anomalies

The eddies play essential roles in heat and salt balances. For instance, the deep water formation in the Greenland Sea requires a transport of salt supplied by the AW transported across the NPF (Walcowski 2014). The supply of AW toward the Greenland Sea

gyre is also needed to close heat and freshwater budget there (Lilly 2003). During the years 2005 and 2006, observations were made of anomalous large anticyclones propagating north-west across the NPF toward the Fram Strait (Walcowski 2014). These eddies carried large amounts of heat, and questions arose as to whether such eddies reach the Arctic Ocean. Investigations shows that this is possible, and that at least one of the observed 'giant'-eddies arrived intact at the Fram Strait. Polyakov et al. (2005) raises the concern that similar eddies might greatly impact the Artic Ocean hydrography. The substantial heat loss in the Lofoten basin and the labrador Sea also require the heatflux supplied by warm eddies to maintain a heatbalance. The ICA in the Labrador Sea have been crudely estimated to provide between 25%-100% of the heat required to balance the heat loss occuring during the winter months (Lilly 2003).

In this context it is interesting to note the temperatures of the detected eddies relative to typical ambient conditions. A potential discrepancy in eddy polarity here is also noteworthy. We expect to find predominantly bouyant anticyclones, and dense cyclones.

Figure 4.9 show the anomalous temperatures of detected anticyclones and cyclones, respectively. The temperature signature is overwhelmingly clear. The anticyclones are predominantly warmer, and the cyclones colder than the surroundings. However, the reverse temperature signature is seen in regions hosting Polar Waters. Owing to the fact that potential density of seawater is controlled by temperature and salinity, this is not surprising. The notion that anticyclonic eddies are bouyant and cyclonic eddies are dense, is still in accordance with these results. In warm waters, temperature primarily set the density stratification, but in colder waters such as the Polar Waters, salinity serve as a proxy for density. Hence, anticyclonic cores may comprise of cold Polar water, and still be buoyant, due to the low salinity effect.

To verify the trend we see in the maps, we examine how temperature and polarity relate at a couple locations. The top scatterplot in figure 4.10 from the boxed region covering the Iceland-Faroe Frontal Zone and the Faroe Shetland Channel is presented, and the lower plot represents the boxed region off Lofoten. The blue colors represent cyclonic eddies and the red anticyclonic eddies. We can readily see that the cyclonic eddies of positive relative vorticity are mainly colder than the environment, and the opposite is seen for the anticyclones.

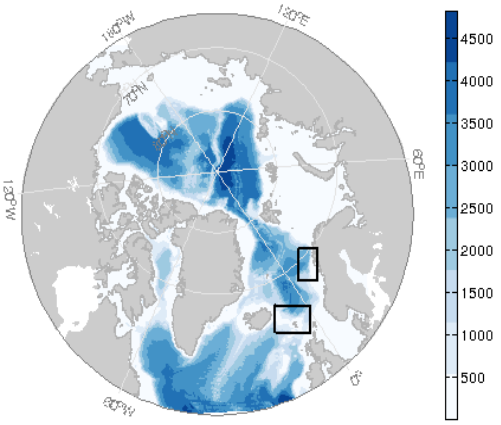

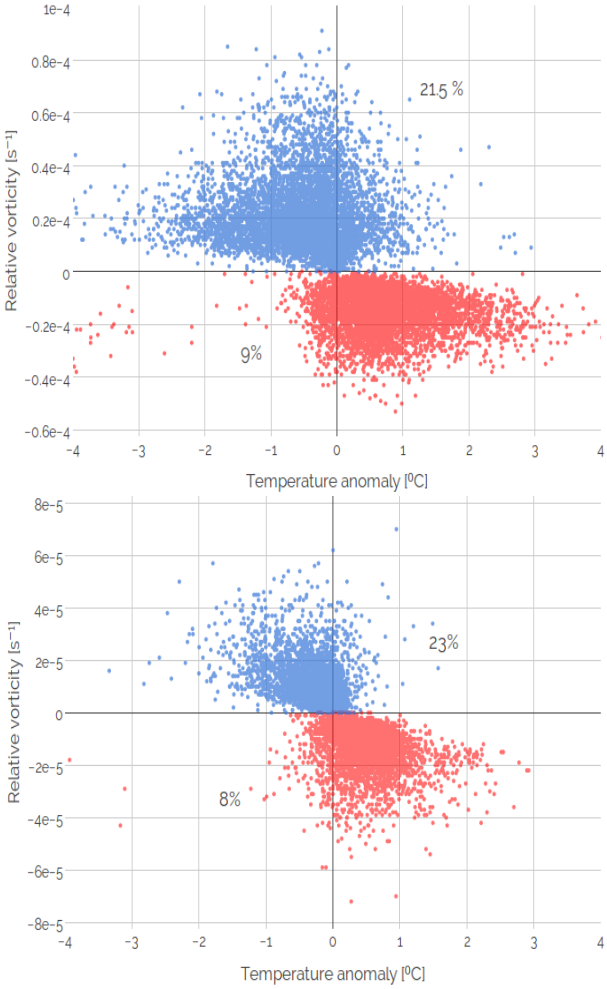

Figure 4.10: Top: The two boxes are the areas considered. Middle: The temperature anomalies of detected eddies in a region embedding the Iceland-Faroe Frontal Zone. Bottom: The temperature anomalies of detected eddies in a region off Lofoten. The percentages in the two lower plots denote the fraction of eddies showing the opposite of the major trend.

4.4.5 Eddy lifetimes

An eddy lifetime is commonly defined as the timeperiod from the eddy originates up until mixing and frictional dissipation destroys its identity. The evolution and consequent duration of an eddy varies greatly, and depend on complex, nonlinear phenomena. If the spin-down processes are known, the eddylifetimes can be crudely estimated. Sea ice can act to dampen the eddy's intensity. Lateral and vertical velocity shear associated with the eddy and ambient flow may also play this part (Timmermann 2008). Radial velocities can foster convergences or divergences in the horizontal flow field with a resulting vertical flow. This then, can allow for mixing to occur across the eddy boundary, and weaken the distinctive eddy core characteristics and velocitites. Despite that there exists several more spin-down mechanisms, some of the eddies keep intact for long time. Ripa (2000) adressed the stability of ocean vortices and noted that "The longeviety of some vortices is remarkable, given the turbulent environment in which they a embedded. Others, though, do not last long."

The lifespan of the eddies we were able to track range from 1 day to a maximum of $1\frac{1}{2}$ years (539 days), with a mean of 26.8 days. The mean is calculated for all eddies tracked for more than a day. The majority of the eddies lasted for less than one month, only 22% had lifetimes exceeding this. Petersen et al. (2013) conducted a eddy census globally, and report that merely 25% of their identified eddies lived for longer than 28 days. We bear in mind that this was a global, three-dimensional study. The coherence here may imply that there exist a large number of shorter-lived vortices, or it may be that the tracking routines need improvements, or the models have a too coarse gridresolution.

The eddy-lifetimes relative to the percentage of eddies tracked for more 30 days is shown in figure 4.11.

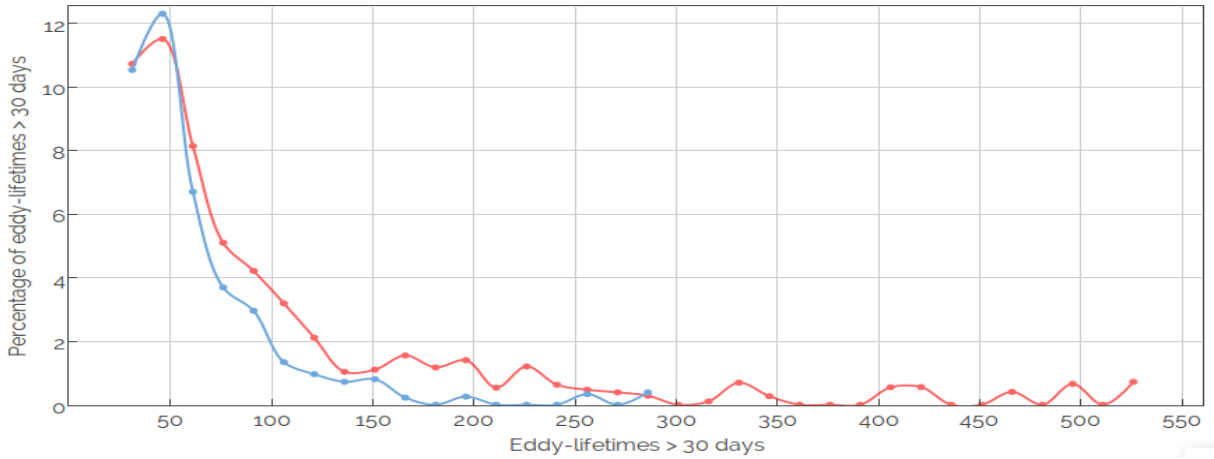

Figure 4.11: Lifetimes of detected eddies tracked for longer than 30 days. The red line denote anticyclones, and the blue cyclones.

The lifetimes shown are apportioned according to eddy-polarity. We find an asymmetry in the distribution. Anticyclones are prevalent for lifetimes exceeding 60 days, whereas a greater number of cyclonic eddies occured for shorter lifetimes. All eddies tracked for longer than 272 days are anticyclones, which show that anticyclones might be more resilient than cyclones. We shall however keep in mind that some part of the cyclones are of smaller scales. If they get too small the routine may not

be able to identify them. Consequently, an attempt to keep track of them during their entire lifetime will not succeed. Setting possible weaknesses of the tracking routine aside, it is likely that the eddies tracked over longer periods, play a larger role in transporting water properties away from their formation site. For this reason, we focus on the eddy tracks with a longer duration. Additionally, map showing tracks of all lifetimes are very busy and hard to decipher.

Under the assumption that the eddytracking results are liable, we might hypothesize why the anticyclones would be more resiliant than the cyclones. As alluded to, an explanation for an eddy life-cycle is difficult to conjecture. We have not investigated the evolution of discrete eddies throughout their lifetimes, and noted potential dissipation routes. Our approach is rather here to look for an overall causation that might serve as part of an explanation.

The notion of longer-lasting anticyclones do concur with earlier observational studies (J.Lilly pers.comm). Lilly (2000) suggest this is the reason for the predominance of anticlonic eddies seen in the central Labrador Sea. A typical generation location for these eddies is off the west coast of Greenland. From there, the eddies have to travel great distances to reach the central part. Cyclonic eddies are hardly observed there, and may not make this far if they are shorter-lived. Pedlosky et al. (2008) also examined eddy generation along the west coast of Greenland, employing a 3-layer quasi-geostrophic model. Their study show that anticyclones have longer lifetimes than the cyclones, and therefore prevails in the basin. They describe a typical eddy evolution event consisting of the following steps. Initially, a dipolar structure is formed. The cyclonic disturbance is forced downstream and is subject to the current's cyclonic shear which rapidly, within a day, acts to destroy it. Thus, an anticyclonic eddy is left in isolation, which eventually moves into deeper waters triggered by the combination of a downstream topographic step and conservation of vorticity. The quick destruction of cyclonic eddy, and the persistent anticyclones propagating basinward, is observed to occur frequently.

Petersen et al. (2013) claims that kinematic considerations give reason to expect that eddy size and lifetime are positive correlated. The basis for this is that the larger eddies carry more mass and momentum, and can better resist ambient shear or impacts of passing over topography which works to destroy the vortices. They find a clear correlation between eddy size and lifetime. Our results show a preference for anticyclones to be larger than cyclones, whoes longer lifetimes might be supported partly by this.

If we further take a glance back at figure 4.7, we recall that large fractions of cyclonic eddies are found along the boundary currents. These cyclones find themselves more frequently in regions of high shear. If some extend down to the shelf topography, they will also be affected by bottom friction. The anticyclones however are more concentrated nearer the centres, and perhaps often freer to develop undisturbed.

4.4.6 Generation and termination of eddy trajectories

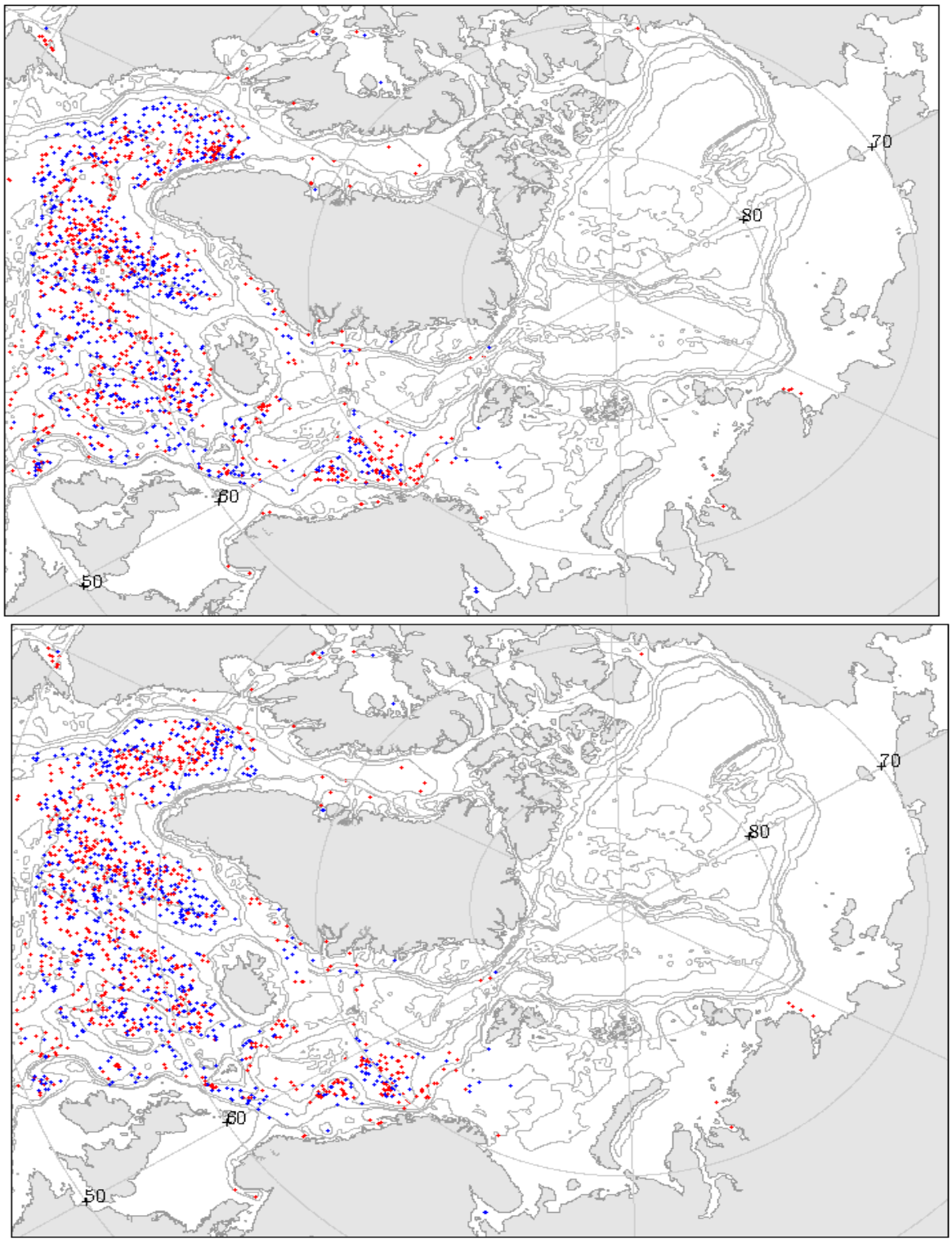

Figure 4.12: Top: Generation points of eddies lasting longer than a month. Bottom: Termination points of eddies lasting longer than a month.

We now examine briefly the initial and final positions of the detected eddies' tracks. We are causious with the terms generation and termination points, due to the possibility that an eddy might have developed prior to being identified, as well as terminated after it is lost track of. With this in mind, the locations where eddies are initially detected and eventually lost, might still indicate particularly active eddy-generation and -termination spots.

Figure 4.11 depict first and final positions of eddies lasting for 30 days or longer. A striking consequence of focusing on these more resilient eddies, is that the Barents Sea and the Arctic Ocean is almost entirely devoid of eddies. Additionally, hardly any eddies are seen along the east coasts of Greenland and Canada where icecovers exist. Nevertheless, the eddies show up on maps plotted for shorter timeperiods. Smith (2000) mentions the difficulties of estimating eddy lifetimes in the Polar regions. He presents a suspicion that in sea-ice covered regions, lifetimes will be shorter and decayrates higher, due to the friction applied by the sea-ice. This might explain why we are not seeing any eddies of longer lifetimes where there is sea-ice. The Barents Sea has a partial sea-ice cover, but is a very shallow sea, where bottom friction might act to bring down the lifetime.

In the Labrador Sea, an active generation region is quite evident. A particularly clear location of eddy origins is seen on the westcoast of Greenland. In the following plot over the termination points, eddies that emerged in at one concentrated spot, have been scattered. Most of these seem to be anticyclones, which end up in the central basin. This fits well with the common notion that Irminger Current Anticyclones are formed in this region (Lilly 2003). In the Lofoten basin, the same tendency appears to occur. There are anticyclones accumulating in the basin at the end of the eddy lifetimes.

Furthermore, a discrepancy in eddy-polarity becomes evident when focusing on eddies with lifetimes of 3 months or more. Eddy eddytracks in the Lofoten Basin and the central Labrador Sea (not shown) are then exclusively anticyclonic, while cyclones populate the Irminger Sea. As expected from our attained eddy lifetimes, anticyclonic eddies strongly dominate the picture.

4.4.7 Energy transfer

Lastly, we will take a look at the energy transfer in the full model fields. This is not a part of the eddy detection routine, but serves as a pointer to wether baroclinic instability can be claimed as the primary source for the eddies detected in the study domain. As seen in section 3.2 baroclinic instability leads to a transfer between APE and EKE. In the energy budget, which for a bousinessq fluid entail a coservation of kinetic energy and potential energy, a transfer term arises, the vertical bouyancy flux. The eddy part of this term denote the transferal of available eddy potential energy to EKE. A way to realize this intuitively follows in line with the discussions in section 3.1 and 3.2. We saw there that a horizontal density flux will result from baroclinic instability, but also a vertical buoyancy flux since the process entails moving light on top of dense water. If light water is lifted into a denser environment, and dense water down, then the sign of this flux will be positive. Computing this flux will therefore map ut locations where this processes is active, and we will assume that it is most likely baroclinic instability causing heightened values of this flux. We keep in mind however, that the full model field will, as mentioned concerning the EKE, also encorporate motions acting to produce the same signal. We can then again compare the fields to the calculations we made of how much the most unstable wave contributed to such an energy transfer. We compute the term $\overline{w'b'}$, where w' is the perturbation vertical velocity, and b' is the perturbed buoyancy. By removing a 3 month seasonal mean from the daily values, we get (w'=w-$\overline{w}$ and $b' = b - \overline{b}$. The product of this is then averaged over three months for all the 10 years. We attain an annual field by then taking the mean of all four seasons. Figure 4.12 shows the vertical density flux(top).

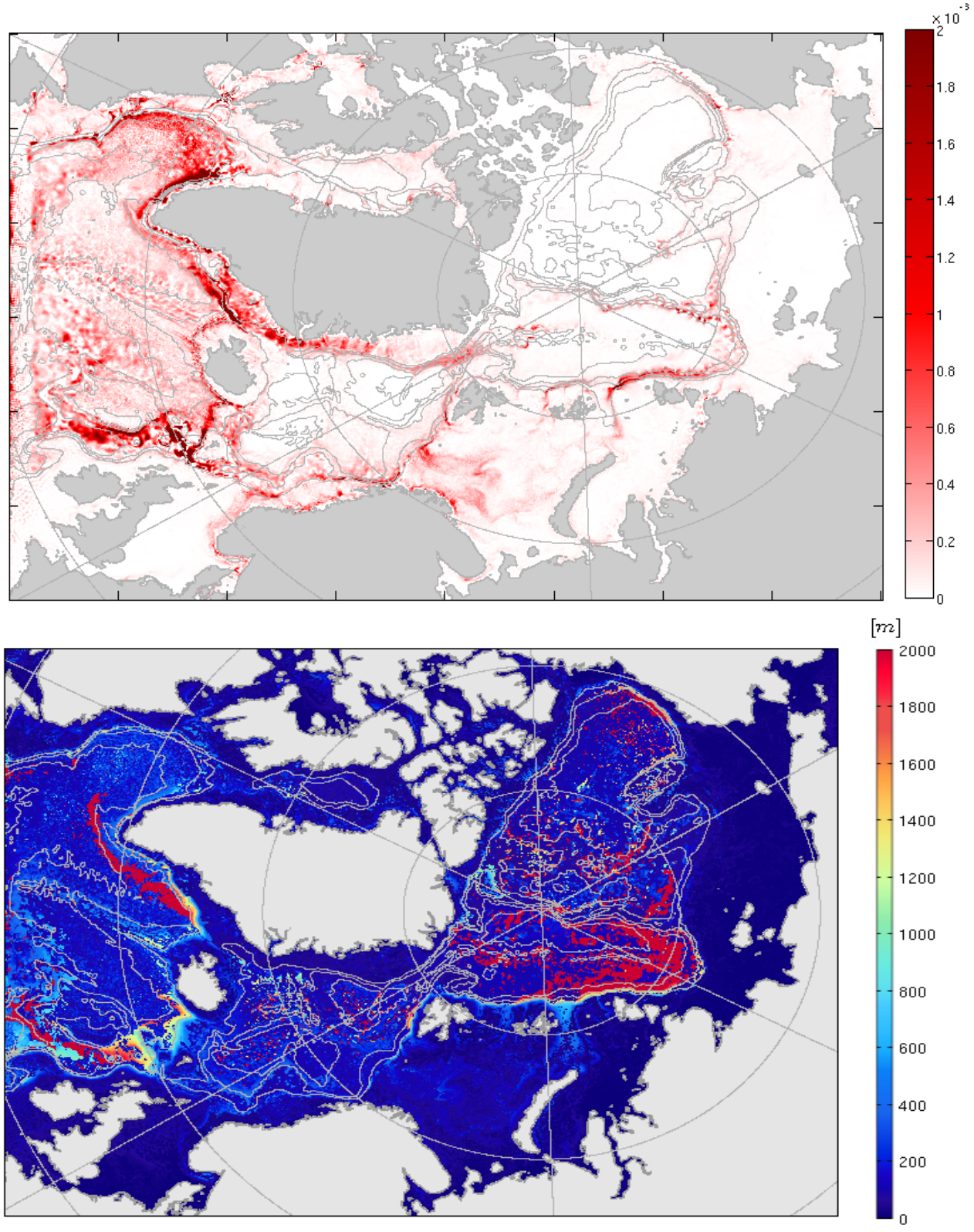

The spatial patterns here reveal a large consistency with both maps attained from the linear analysis. We take note that the colorscale for the transfer is slightly different here, but this is to bring out the patterns of distributions. The magnitudes are of the same order as presented in (Smith 2007), in W/m^2. Locations of

strong baroclinic energy conversion are strikingly coinciding. The largest values occur along the strongest currents zones. The energy transferral of the gavest modest appear more localized in spaced. There are high transferrals for instance in the Labrador Sea, which likely mirror that advection of eddies int oThis is expected as these are regions steep isopycnals slopes, and as we recall, the process utlimately works to level out the steepness into that region. By the coherence of the two maps, wa can to the least say that baloclinic instability plays the major role in this. The depth of the maximum conversion is shown in the lower plots. When leaving out the upper 1-50 m in calculation the depths of these patterns are also very similar.

Chapter 5

Summary and discussion

5.1 Summary

This study aimed to gather more knowledge of eddies in the SubArctic Seas, and to examine if baroclinic instability could be responsible for the region's mesoscale eddy activity. This is to, the author's knowlegde, the first comprehensive eddy census model-study encompassing the entire domain.

Through this study we have
1) Tested the hypothesis that baroclinic instability can accounts for most of the eddy activity in the study region. We found that it can be regarded as the primary source for the eddies.
2) We have related the eddy length and time scales provided by linear predictions with statistics of the fully-developed macroturbulent field. A linear stability analysis on mean fields from a 10 year model simulation was successfully conducted.
3) We discussed the growth rates and associated length scales of fastest growing waves, and looked briefly if Eady dynamics could account for the growth we found. The last point was intended to be more extensive.
4) We implemented an eddy detection procedure, and investigated the statistics of the fully turbulent field in terms of the characteristics of the identified eddies.

5.2 Our results in light of previous studies

In this chapter we examine the results of this study in the context of the of earlier studies that have estimated eddy characteristics either through a linear analysis, or direct observations of eddies. Firstly we compare the predictions from the LSA with previous studies. Secondly, we take a plunge into the existing records of eddy characteristics inferred from observational studies, and look for agreements or disagreements in what was provided from the eddy detection procedure. Finally, we juxtapose the characteristics yielded from linear theory and from the statistics of the nonlinear field. By this, we look to infer what utility a LSA has in characterizing the mature eddy field.

5.2.1 Characteristics inferred from linear stability analysis

We have found few linear stability analysis studies covering our study domain, and there are no LSA studies that take more than one particular region into account. Hence, a full comparison throughout the domain is not attainable, but we can still examine specific locations. The most recent studies are investigations of the NwAC round the Lofoten basin by Isachsen (2015). He performed a linear stability analysis based on model output, and focused on the effects of topography as means for a comparison with Eady theory. The model data he used is a subset of the same data utilized in our study. In

Isachsen (2015), maximum growthrates are found over the steepest topographic slopes along the Norwegian coast. Isachsen(2015) notes that these areas also host the highest EKE leves, which indicates that baroclinic instability most likely can be held accountable for the eddy activity in that region. Our results are in general accordance with his findings, both in terms of magnitude and geographical distribution of growthrates and lengthscales. In both studies, predictions from the Eady model seemingly produce saticfactory results when compared quantitatively. The basin however consistently appears to have smaller but faster growing waves than Eady dynamics predicts. However, even if the model can yield reasonable growthrate estimates, it is becomes evident that assuming a zero PV gradient in the interior neglects important dynamics. In agreement with Isachsen(2015), at several locations found here the unstable wave amplitude is forced to dissappear as it approaches a bottom slope. Isachsen reports that computations with a flat bottom give a reduction in spatial scales and growth rates, which was also consistent with the altered Eady model of Blumsack and Gierasch (1974).

Another recent LSA study of the Labrador Current between $50^\circ - 58^\circ$N, was conducted by Thomsen et al. (2014). The main core of this current has been estimated to be postitioned between $55 - 58^\circ$N. Mean flow and stratification needed in the LSA, was obtained from both mooring data and model simulations. The analysis was done in a nonhydrostatic ageostrophic setting. They sougth to find a cause for enhanced EKE levels observed during winter months. Their study uncovered three types of unstable modes that were dominant. The one relevant for comparison here, is the socalled balanced,interior mode resulting from baroclinic instability. This was the mode with the largest spatial scale. It had maximal growth rates of 1 day^{-1}, and wavelengths of about 30-45 km. The growth rates from our calculations, are in relatively well agreement with theirs. A comparison is displayed in figure 5.1 below (see figure 8a) in Thomsen, Soren. Eden (2014) the figure presented here is rotated -90°).

We notice that the peak growthrates we attain are larger than theirs, with a maxima of about 1.5 day^{-1} along the core of the Labrador Current. Even so, the patterns of high growth are comparable. We cannot expect a complete agreement, neither compare these results in the smallest details as their analysis has a different basis, and represent only growthrates in March while ours is from a 10year mean. Nevertheless, from a larger perspective, the spatial patterns and values are of the same order. In both studies there lingers little doubt that the Labrador Current is baroclinically unstable.

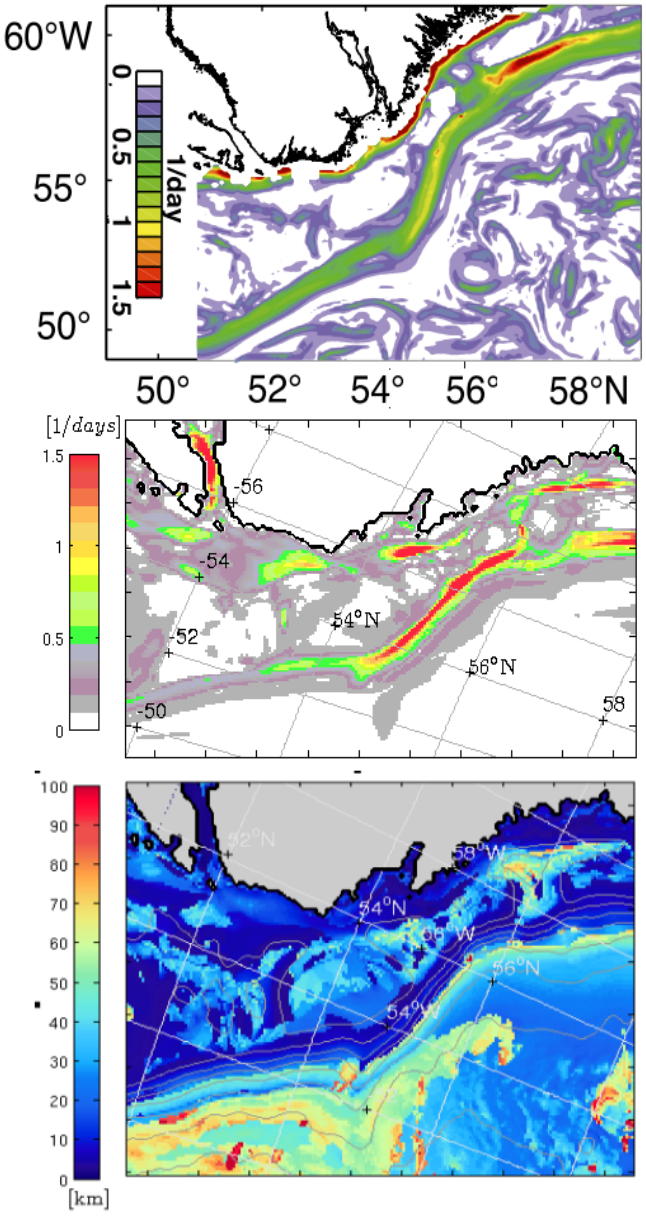

Figure 5.1: Top: Growthrates for the unstable interior mode in the study of Thomsen et al. 2013, shown in figure 8 a) pp.458. This is computed from model data in March. Middle: Predicted growthrates of the most unstable mode in our present study, calculated from 10 year mean datafields. Note the different colorscheme. Bottom: Lengthscales associated with the most unstable wave in our study, contour-lines denote bottom-depth showing 250m and 500 m, and then onward with a contour-interval of 500m.

The associated lengthscales found here divert from their findings. We find a lot smaller wavelengths of about $10 - 25$km related to the most rapidly growing waves. This difference may be rooted in several things, related to issues of numerics, differences in the model runs, the analysis or simply that we have not captured the largest mode in our selection. We do however speculate if this could be an effect of an included topographic slope. Thomsen et al. neglect topography in their calculations. The basis for this was that they were focusing on seasonal effects, and there is no seasonal change in topography. They do however mention that some studies (Isachsen 2011; Vollmer and Eden, 2013) point to a stabilization and surpressed growthrates by including topography. We do not find reduced growth rates over the slopes, the magnitude of the growth rates seem rather unaffected by this and even exceeding their flat-bottom calculations. However, the discrepancy is seen in the lengthscales. As noted in 3.4, along most of the rim current, though hosting high growth rates, length scales are systematically shorter over the steep topographic slopes. It may perhaps seem unlikely that the waves should reduce to half the sizes merely due to topography, but appears at least to contribute in some way. It certainly contributes to the strucure of the wave. The interior modes in Thomson et al. were attributed as Eady-type instabilities, due to their along-flow orientation and the relation between growthrates and wavenumber.

We remark again that in our analysis, Eady-type instabilities did not commonly occur, particularly not over steep topography. The Eady-type has maximum amplitudes at the top and bottom, but we frequently found only a maxima at the top and zero at the bottom. This serves again as an example of incidentally comparable growthrates, but with different underlying dynamics. Additionally, as noted by Isachsen (2011; 2015), a modified Eady model that includes topography, predicts supressed growth and wavelengths when the bottom and isopycnals slope in the opposite direction. This scenario is commonly found along the coast, where buoyant water rest on the shelf and denser water is found on the seaward shelfside. The modified Eady model, give no explanation to why we are seeing enhanced growth here. Another aspect to this issue, is that our analysis relies on quasi-geostrophy, which will get problematic over steep bottomslopes. In the derivation of the QG-equation, one of the main requirements invoked, is that the fraction between the bottomslope and the fluid depth is on the order of the Rossby number, which should be $<< 1$. Hence, we need to be careful in our claims concerning regions of steep topography. It would be beneficial to repeat our present stability analysis using linearized primitive equations, and look for discrepancies between the solutions. The latter should be well-behaved also over the steep slopes, and could give an indication of the degree of sensitivity in the QG estimates. Still, one would need to consider closely how to select the unstable modes in each case, if they are to be compared justly.

We shift our attention back to the Nordic Seas in the rest of this section. In the LSA we performed, noticably large growthrates were associated with both the Norwegian Coastal Current (NCC) and the eastern branch of the Norwegian Atlantic Current (NwAC). The flow following the topography anticyclonically around the VÃ¶ring Plateau did also entail elevated growthrates with a timescale of about 5 days, but these are much weaker than the intense growth exhibited in the inner branch with a period of 1 day.

The variability in the NCC is believed to be driven by local instabilities. Ikeda et al. (1988) utilized sattellite imagery of the NCC and current meter data, as well as an idealized QG-model in an experiment they called the Eddy Tracking Experiment. Their study area is displayed in the pink boxed regions in

figure 5.1 superimposed on the results of our study. The western part of the study area is occypied by incoming (dense) Atlantic Water (AW), carried by branch of the NwAC deflecting into Skagerak. The NCC is positioned along the coast, and consist of fresher coastal waters (**?**). Satelitte pictures had revealed the presence of a sequence of eddies of 60-100km wavelengths along the Norwegian coast, and one question the authors adressed concerned possible sources for these eddies. They regarded both barotropic instability and baroclinic instability as plausible eddy generation-mechanisms. Through an energy analysis merely 1% of the kinetic energy was fed to the emerging perturbations, and the wavelengths related to this barotropic instability were extensively larger than what had been observed. They concluded that baroclinic instability was the dominant generation mechanism for the eddies they observed and simulated. A stability analysis from their QG-simulation yielded a wavelength of 54 km and a timescale of 2.3 days for the most unstable wave. Neither the observed nor the modeled spatial scales are consistent with ours at more than the southwestern area of the domain. Elsewhere, much smaller length scales of 10-25 km are seen, and the growth occur at an overall slower rate.

There are many possible sources for the discrepancies. Smaller scale instabilities may be harder to catch by a manual detection in satelitte imagery. On the other hand, we could have missed modes of larger scales in our LSA, and selected some of smalles scales. Nevertheless, comparable scales and growth rates are found just south of this region, and further along the part of the NCC encapsulating the entire southern coast of Norway (see fig.3.5). Shi (1998) performed a LSA on the front between the the saline, dense AW and the fresh, light coastal water in the NCC. This front is present all along Norwegian Coast, as the NCC and the NwAC in tandem are make their way up North. In the linear stability analysis of Shi (1998), the dominant unstables waves were found at 16 km with period of at 1.25 days. It is suggested that these short waves, are a product of a frontal instability, in which the disturbances grow at the expense of the potential energy stored in the steep isopycnals across the front. Shi, Xiao Bing, Røed (1999), performed a linear stability analysis in their study of frontal insstabilities at upwelling fronts. Their analysis found a preference for the gravest modes to appear within two distinct bands. One band occuring at 10-20 km with a timescale of one to two days, is referred to as the frontal mode, arising from baroclinic instability. The other band was at 60-70 km, referred to as the mixed mode, arising from both baroclinic and barotropic instabilities. Interestingly, in figure 3.5 we noted that the NCC, the Labrador Current and parts of the East Greenland Current had high growthrates at short length scales. Again, this coincides with steep bottom slopes, which one of the potential weaknesses of the present analysis. Nonetheless, we can remark a possibility that the mode selected here could be a smaller-scale frontal mode. The basis for this is that these currents seperate two watermasses, light waters on the shorward side and denser on the basinward side, which sets up local frontal zones. The topography can act to increase the cross-flow density gradient, and aid to steepen the isopycnal slope and thereby the vertical velocity shear. It was noted by Shi and Røed (1999) that when the vertical shear was incresed, the growthrates were increased.
energy Another study, by Mysak and Schott (1977), found evidence that the NCC, around $63°$N, was baroclinically unstable. They had observed eddy features with length scales of 30-60km. and from mooring measurements of the current strength, the energy spectra peaked at periods of 2-3 days. Experiments with several idealized barotropic models were conducted to try to explain the observed variability. Barotropic instability could not yield the observed wave frequency, so they carried out a linear stability analysis to see if baroclinic instability could produce positive complex frequencies closer to the observed values. They used two baroclinic channel-models with two layers and different uniform, cross-stream topographic slopes (The second model was the one of Smith (1976)). Adjusting to a representable slope, yielded better results. The fastest growing wave that best matched the observations, had a period of 2.5 days and a wavelength of 39 km. The growthrate corresponds to 0.4days^{-1}, and lies within the range of values also we find along parts of the NCC. However, the peak imaginary frequencies rendered form our study exceed the values in both the observations and the model

experiments. The observed spatial scales of 30-60 km were sampled from in-situ data within the black boxed region in figure 5.1 The figure show the resulting lengthscales from our LSA. We see that the span of scales of the most unstable modes is well-respresented by the observed sizes, however, when including extremal values, the LSA length-scales in this region lie within a larger interval of 10-80 km.

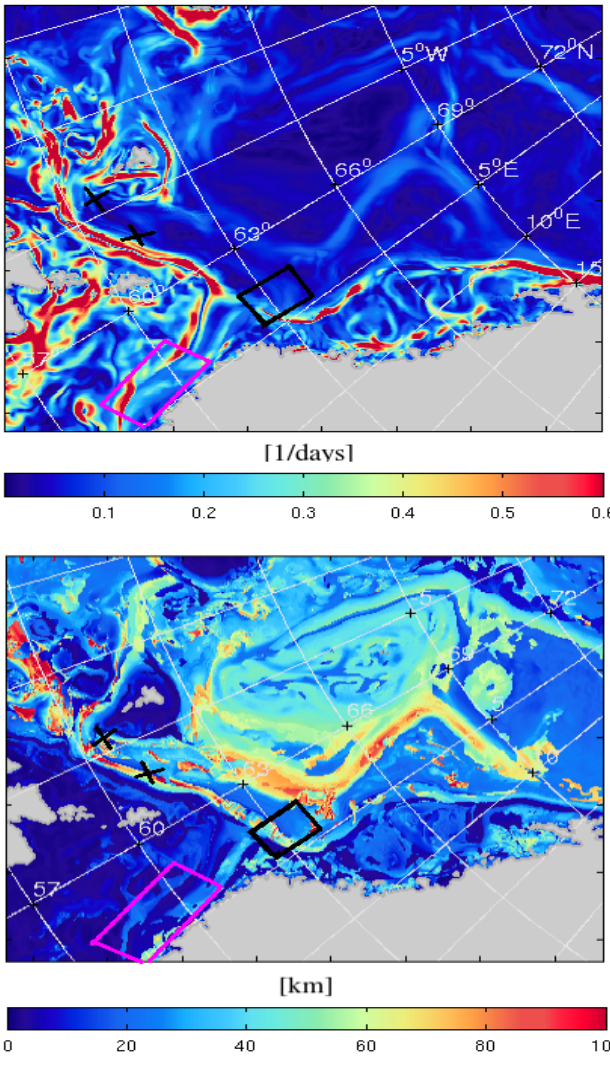

Figure 5.2: Growth rates and lengthscales for the fastest growing wave. The crosses and boxes relate two thee of the studies we are considering here.

Hanzlick (1983) applied the baroclinic model of Mysak and Schott (1977) to study baroclinic instability in the West Spitsbergen Current (WSC). Lengthscales of 30-40 km and periods of 3-4 days were found. The slightly slower growthrates in the WSC than in the NCC were proposed to be an effect of the steeper bottom slopes near Svalbard. On the contrary, the growthrates in our study do not seem to decrease toward the steep slopes near Svalbard, but rather decrease as the slope levels out past the Lofoten area. The length scales we find around the position of the WSC are smaller than- or comparable with what was found by Hanzlick. Teigen et al. (2010) also found indications that the easternmost part of the WSC was baroclinically unstable. A linear stability analysis of data from current meter moorings, yielded wavelengths of 15-30 km, and periods of 1.5-3 days. These higher growthrates, and smaller spatial scales fit our results better than Hanzlick's.

An area in connection with the southern parts of the NCC and the NwAC is referred to, by Rodionov et al. (2004), as the Iceland-Faroe Frontal Zone (we adopt their term, IFFZ, here). An early sketch of these connected regions by Griffiths et al. (1982) is shown in figure 5.3.

The IFFZ has been found highly unstable. Rapidly evolving small-scale eddies and frontal meanders on timescales down to 2 days, and length scales down to 10km are frequently observed there (Poulain et al., 1996). The area stand out as highly unstable in our growth-rate calculations. This suggests that baroclinic instability may support the observed elevated eddy-activity there. We refer again to figure 3.4 displaying the growthrates over a subdomain of our analysis. We now focus our attention on the region west of 0°-meridian, between $61 - 63°$N. We remark that timescale of 2 days ($0.5\text{days}-1$) is observed, but also that the peak growthrates are even higher. We fing a maxima of 1day^{-1}.

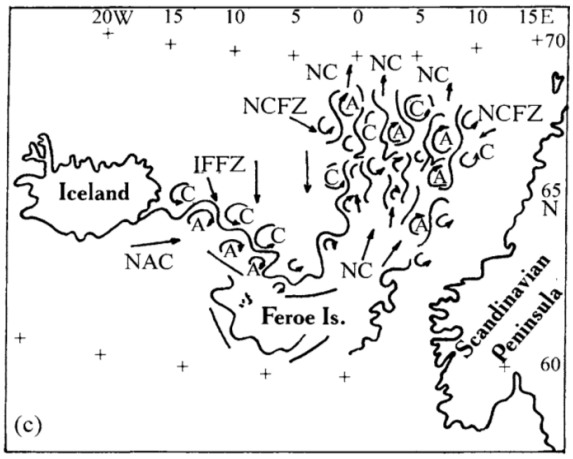

Figure 5.3: Sketch of currents instabilities along the Iceland-Faroe Frontal zone, and the NwAC, according to Griffiths et al. (1982).

Embedded in the IFFZ is the Faroe-Shetland Current, a narrow slope-current which is an important contributor for the inflow of AW into the Nordic Seas (Sherwin 2006). According to Hansen and Østerhus (2000), over half of the heatflux is introduced to the Nordic Seas via this current, and hence plays a significant role in the ocean's density-driven circulation. Eddies observed in this region are believed to be generated by baroclinically unstable frontal meanders (Sherwin 2006). The model of Mysak and Schott (1977) was utilized yet again in a baroclinic instability analysis by Sherwin (2006). He studied mesoscale variability in the Faroe Shetland Channel, and found that the region has high eddy activity originating by meanders in the front separating two watermasses there (AW and modified AW). Data was sampled from a large multitude of different in-situ measurement equiptment, and compared to the stability analysis. The model produced unstable waves at scales of 49-59 km, and growth rates of 3-5 days, largely depending on the strength of the vertical current shear. Sherwin concluded that the eddy generations can, at the initial growth stages, be explained by baroclinic instability. The observations that was gathered implied that the meanders occurred at particular locations, rather than emerging randomly. In figure 5.2, the two black crosses indicate the preferred locations. The unstable wave-characteristics recovered in Sherwin (2006), lie at the lower range of what we find in this region.

We have seen both discrepancies and consistency between the results of ours and previous studies. Since most of the studies lack a common platform that suits a detailed examination, we did not anticipate a detailed agreement, and neither is this our main concern here. Our main aim here was to map out the general picture we find depicted in literature on the role of baroclinic instability within the study region. A recaptulation so far is that we find supporting evidence for our claim that this type of instability likely is the main advocator for the eddies.

5.2.2 'Observed' eddy characteristics

We now turn to the part of this study concerning characteristics of the fully turbulent field. We will compare the properties of our detected eddies with what has been derived from mainly observational studies.

The regions of high eddy activity found by the eddy detection algorithm (seen in figure 3.4) are consistent with the findings of several previous studies (Rossby et al., 2009; Prater et al., 2009) Observations have displayed a vigorous eddy field at the Iceland-Faroe frontal zone (Sherwin2006). The Norwegian coast with its broad multistructured frontal zone, is frequently infested by eddies (Rodionov 2004, Mysak and Schott 1977, Ikeda et al. (1989)).

We found few recent studies charting the eddy field within the Barents Sea. Mesoscale vortices has however been recorded in most parts of this sea. Studies report the presence of eddies in the western region of the Sea, close to the connection with the Norwegian Sea (Johannessen et al. 1983a), and in the northwestern part, where subduction of North Cape Current water under fresher Barents Sea water occurs(Kosolapov and Lebedev, 1989b, Lebedev, 1992b). Antiyclonic eddy generation has been observed in the MIZ in the melt season (Fedorov and Ginzburg, 1988,1992). The presence of the NPFZ, which seperates Barents sea- and Atlantic waters, often exhibiting across temperature gradients of 2-3°. Its heavy meandering, is a source of frequent eddy formation (Rodionov et al. 2002).

This front is highly evident in the 10year mean model hydrography in figure 2.3, and snapshots of the temperature field clearly show an abundace of mesoscale structures. In figure 4.2 we see there are high eddy counts occurring around the mean position of this front.

The distribution of the eddies' anomalous temperature, displayed in appear to be quite consistent with observations. Cold Irminger cyclone s with 5-18 km radius, and larger 15-30 km warm-core eddies have been found in mooring measurements from the centre of the Labrador basin (Lilly 2002). In the Irminger Sea, anticyclones are reported to entail anomalous saline cores relative to the ambient waters(Johannesen 2013; Johannessen et al. (1987)). Observations from satellites and current meters have revealed cyclonic eddies that are trapped in the EGC, and do seemingly not escape the current (Bruce 1995). These eddies' temperature signal was colder than the embedding current. The cyclones we detected near the EGC mostly also had a cold signature. However on the shelf where the fresher(lighter), colder waters reside, and the cyclonic eddies show a warmer temperature anomaly. This is consistent with the expectations that cyclones embed denser waters, and also that anticyclones are buoyant as they seem to enclose fresh, cold Polar waters in their cores. We anticipate to see this wherever the salinity mainly determines the density, which becomes evident in the temperature anomaly maps (figures 4.). In fact, we do see a reversed temperature trend in the regions occupied by fresh, ligth PW. Of the 14 eddies identified near the Fram Strait during MIZEX '83-'84, the cyclones were reported to wrap around warm AW (Johannessen et al. (1987)), as depicted in figure 5.4 Furthermore in a study of the west coast of Greenland, warm-core rings were observed off the coast in both winter and summer, nearly all of anticyclonic rotation(Zhu et al. 2013). Similarly, anticyclonic eddies have been found to be predominant off Lofoten in the Norwegian Sea.

Consistent with our findings, Richards and Straneo (2015; early online version), state that the anticyclones in the Lofoten basin have positive averaged temperature and salinity anomalies, and scarcely any close to zero or negative anomalies. They report of maximum anomalies of $0.3°C$ in the Lofoten basin, which are a lot lower what we find which can be up to several degrees. They further note that the anomalies in the Lofoten Basin are smaller than inferred values of anticyclones from observations in the Irminger Sea (Fan et al. 2013) and the Labrador Sea (de Jong et al. 2014). In the latter study, anticyclones in the Labrador Sea, had positive temperature anomalies as large as $2-3°$C, and in the former reported temperature anomalies of $0.28°C$. Our estimates in the Irminger Sea are of the same order, but in the Larbrador Sea the temperature appear similar as in the Irmingen Sea.

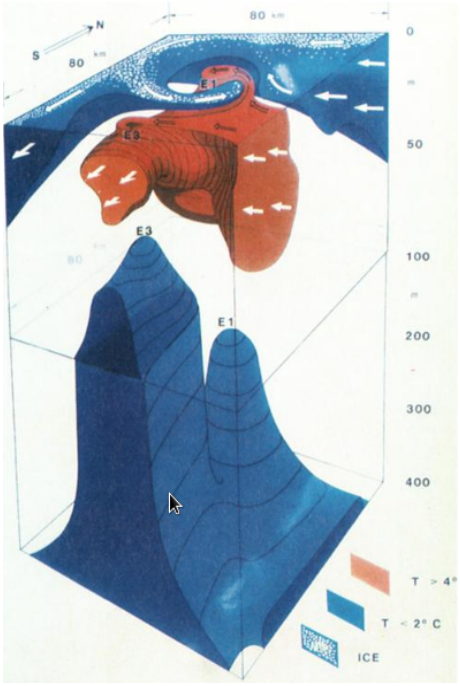

Figure 5.4: An illustration mead based on the discoveried done in and aroung the Fram Strait, '83-'84. A cyclonic feature wraps around saline and warm, but dense, waters (AW).

Cold-cored cyclones were found in an eddy-survey conducted along the Faroe Channel using drifters and CTD and XGB casts. The slope current initially exhibited meanders across the Faroe slope, and the meanders grew into 'backward breaking' filaments wrapping around pools of cold water. The end result was a series of cold-core cyclonic eddies, with temperatures $1° - 1.5°$ colder than the ambient AW. The eddies appeared to be advected along the background flow, and act to entrain cold water in

the warmer FSC transporting them. The anomalous temperatures found in this study is in accordance with our findings.

Allen et al. (1994) states that the Iceland-Faroe Front frequently nurture cold-core eddies, of similar characteristics as those found in the FSC. In a combined high-resolution (2.5×2.5km) model and observational study, also from the IFF, Popova et al. report finding warm anticyclone developing on the colder northern boundary, encircled by numerous cold cyclonic eddies, as well as a cold eddy to the south of the front.

Jakobsen et al. (2003) states that "The distribution of the mesoscale variability indicates that eddies are formed at fronts and shed away into the gyre centers. Here the eddy kinetic energy is relatively large compared to the mean energy". Observational and model studies do show heavy eddy activity associated with fronts and boundary currents. For the two archetype regions of eddy shedding in the Subarctic, off Lofoten and the West coast of Greenland, Jakobsen's statement has shown in numerous cases to be highly valid. The reservoir of AW in the Lofoten basin is replenished by anticyclones expelled from the NwAC, believed to occur near the location where the topography is steepest (Kohl 2007; Spall 2010; Rossby et al. 2009b). The vivid mesoscale eddy scene in the Lofoten basin is thereby upheld by eddies originating along the northbound bondary current, propelling westward into the basin, where they there follow geostrophic contours(Isachsen 2011,2015; Kohl 2007; Raj et al., 2015). Utilizing a numerical model, in conjunction with altimetry, Kohl noted that the spawned anticyclones has a tendency to aggregate at the largest basin depth, and in this way nurish the quasistationary Lofoten anticyclone residing there. We refer back to figure 4.12, in the Labrador Sea both cyclones and anticyclones frequently appear to be generated off the coast of Greenland near $61 - 62^{\circ}N$. The next figure show that most end up in the basin. This formation site is wellknown from past studies. Energetic eddies have been found shed into the central basin from the boundary current near where the West Greenland- and the Irminger Current diverge (Prater, 2002; Lilly et al.,2003; Pedlosky, 2008; Zhu et al.,2013).

In global studies, eddy generation and termination points are found typical also in open-ocean regions(Chelton et al., 2011; Petersen et al., 2013). Basically, eddy origins are found common in whatever region eddies propagate in. The authors note that this agrees with the notion that most part of the World Ocean is baroclinically unstable (Stammer 1998; Smith 2007). Our illustration of eddy generation points(fig.) also indicate widespread occurences of eddy formations.

When we focused on eddies with lifetimes longer than 3 months, it was clear that both the Lofoten basin and the Labrado r basin only show anticyclonic tracks. The tendency of longlived anticyclonic eddies occur in observational and model studies as well (Lilly 2003, Pedlosky 2008). In the QG-regime, there is a sign-symmetry in polarity, and no way to explain differences between cyclones and anticyclones. Studies going beyond the QG regime find that anticyclones have a tendency to be more stable and coherent than the cyclones (Arai and Yamagata 1994; Baey and Carton 2002; Stegner and Dritschel 2000; Graves et al. 2006).

Rossby et al. (2009) deployed 22 floats in the vicinity of either Iceland or the Faroes. They found that energetic trajectories off the Lofoten Islands also appeared to be predominantly anticyclonic. Based on the deepening of basinward isopycnals, implications have been made that large anticyclones are shed from the continental margin (Rossby et al., 2007). Rossby et al. (2009) stated, concerning their results attained by these 22 floats, that *"These float data, despite the limited numbers, would seem to support the idea that the basin circulation is predominantly anticyclonic near the surface, but more research is clearly needed"*.

Assesing isolated events observed eddy sizes against a 10 year statistic, is difficult, both due to the range of scales they can take on. but also that one might be comparing a mean value with the tail of a distribution, which is not representable for the larger part. We found however one study where data from 114 satelite surface drifters in conjunction with a data set comprised of 35 000 buoy

days were used to investigate statistical properties of eddies in the Icelandic, Norwegian and Greenland Seas(Rodionov 2004). Tens of kilometers long meanders of the fronts were found to occur everywhere within the NPFZ, and about 400 eddies detected. Warm vortices are found to appear on the cold side-, and cold vortices are found to appear on the warm side of the front, of both rotation types. Cold-core cyclones are most frequently observed. The resulting eddy length scales corresponded to around 3 times the Rossby radius of deformation, which were in accordance with the length scales estimated from IR images (Rodionov et el., 2004 and references therein).

The table below show their findings. Other studies have reported similar scales. If we are to compare the different regions, we that our findings at least lie within the span of these sizes. During the MIZEX '83-'84 program, estimated eddy-sizes were 20-40 km, rotational velocities around 40 cm/s, and lifetimes about 30 days. MIZEX'87 was carried out as a continuating program of the '83-'84 project. This study indentified and tracked "ice" vortices, vortex dipoles and meanders in the MIZ. Typical scales for the eddy pairs, were found to be 30 km, and the associated lifetimes to be 3-4 days. (Johannessen et al, 1994b, MIZEX'87 Group).
Long-lived anticyclonic eddies with a diameter of about 10 km have also been observed in the Greenland Sea (Gascard et al., 2002) these eddies have a large vertical extent (about 2000 m), which is relevant to the deep-mixing depth.

FRONTAL ZONE	AVERAGE RADIUS	[km]		NUMBER OF VORTICES	
	Cyclones	Anticyclones	Radius all	# C	# AC
East-Greenland	15	16	15.5	20	12
Iceland Coastal	15	15.5	15	17	4
Iceland-Faeroe	14.5	15.5	14.5	16	16
Jan Mayen	17.5	13	17	43	7
Norwegian Current	25	23.5	24.5	28	29
Mohn Ridge	26	19	23	40	10
Norwegian Coastal	16	17	16.5	18	10

5.3 The usefullness of the linear prediction

The local approximation has been used in several studies that has accredited eddy formation to local baroclinic instability (Gill et al. 1974,). It forms the basis for a large fraction of theories for ocean eddies, and is widely used in ocean model parameterizations. Despite this, there are several issues associated with the local approximation we make in the linear stability analysis.As noted, each gridcell of our domain is taken as a local patch of ocean that does not vary horizontally. Eddies that emerge are presumeably a reponse to an instability of the local and steady background field (Vallis 2011). This huge simplification disregards many dynamical aspects such as advection of eddies. Eddies may, for instance propagate, from regions of high growthrates and enter regions with lower rates (Vallis 2011). Furthermore, no eddy-mean interactions are allowed by assuming a steady background flow (Farrell and Ioannou 1999; Flierl and Pedlosky 2007). Vallis (2011) lists several other limitations of the theory: *"Other dynamics that play a role in eddy formation include the radiation of instabilities from boundary currents into the interior* (Kamenkovich and Pedlosky 1996; Hristova et al. 2008), *weakly nonlinear growth of unstable modes (Hart 1981; Pedlosky 1981), sensitivity to nonzonal flow instabilitiess* (Spall 2000; Arbic and Flierl 2004; Smith 2007) *nonparallel flow instabilities* (Pedlosky 1987), *barotropic (BT) instabilities of horizontally varying mean flows, and strongly nonlinear turbulent dynamics"* (Held and Larichev 1996).

The dynamics of the turbulent, nonlinear field represented in the model simulation, is not restricted

to stay within the QG regime (Vallis 2008). The final energy of eddies are most probably a product of nonlinear processes, as are their equilibrated lengthscales (Vallis 2008). Hence, a linear initial growthstage compared to a nonlinear evolution of unstable waves is expected to exhibit somewhat different properties.

Smith (2007), Tulloch (2011) and Vollmer (2013) local baroclinic stability analysis globally utilizing data from climatologies. Spatial scales and growth rates of the most unstable waves was examined, and compared to global estimates of the Rossby deformation radius, L_d, the Eady growthrate and observed eddy scales. The analysis in the three studies exended up to about 70°N, hence most of our present study is not covered in their analysis. Nevertheless, general remarks can be made about the utility of linear theory in classifying the macroturbulent field, as well as noting the relation between the simplest- estimates and a more complex model.

In all three studies, the Eady growthrate, ω_e show near agreement with the maximum growthrate inferred from LSA. This seems to be especially true for the higher latitudes (Tulloch et al., 2011) On the contrary, the lengthscales of the most unstable waves, L_i, are not very well-represented by L_d. Generally, Vollmer (2013) and Tulloch et al. (2011) find that L_i is smaller than L_d at low latitudes, and larger at high latitudes (poleward from $50°$). This is based on zonal averages away from boundary regions, which grants little information on geographical patterns of the distribution. Global maps (fig.6 Tulloch et al., 2011) reveal that the source for this zonal trend is largely caused by discrepancies in the Antartic Circumpolar current (ACC). The ACC and locations of intense growth at the same northern latitudes, such as the Kuroshio, the Gulf Stream and branches of the North Atlantic Current's (NAC) venturing toward the Nordic Seas are larger-scale instabilities, with a scaling $L_i > L_d$. The authors note that the weakly unstable gyres entail smaller-scale instabilitites.

Quite conversely, Smith (2007) found that L_i was smaller than L_d in the ACC, and at all latitudes in fact. He implemented a filter to sieve out less important waves in terms of baroclinic energy conversion, that are anticipated to be of smaller scales. Still, the resulting spatial scales of some larger scales show the same tendency. Figure 5.5 below show a comparison of the maximum growth, the observed and the deformation scales. Generally, we see that the fastest growing waves are well below L_d, however less so in the high latitudes, a tendency which concurs with the other two studies recently mentioned. All the observed scales exceed the linear predictions greatly near the poles. The eddy census from satelittes by Chelton (2011) show a largest gap. We keep in mind, the limited ability of satelitte retrievals(this far) can provide in representing realistic characteristics of the smallscale mesoscale features at high latitudes.

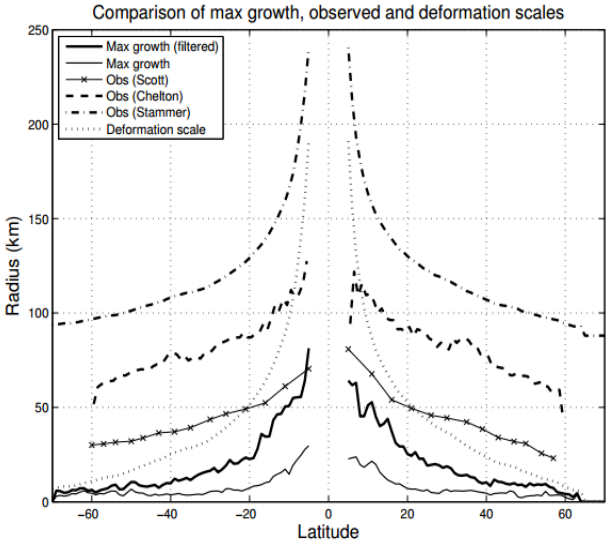

FIGURE 11: Zonally averaged scales (in km) of: maximum growth, filtered by condition that baroclinic conversion $G > 0.5$ mW m^{-2} (bold solid line); scale of absolute maximum growth (thin solid line); the inverse of the centroid wavenumber of surface kinetic energy spectra from analysis of satellite observations by R. Scott (line with x's); the radii of coherent vortices from the analysis of satellite observations by Chelton et al. (2007) (dashed line); the zero-crossing of the lag of the spatial autocorrelation function from the analysis of satellite observations by Stammer (1997) (dash-dotted line); and the first deformation radius (dotted line).

Figure 5.5: Figure 11) from Smith (2007).

An aspect all the three studies in discussion here share in common is the agreement that scales from LSA are smaller than the observed scales. this is consistent also with our findings. We suggest, as also proposed in the other studies, that the larger scales demonstrates an inverse cascade of energy. This can, as mentioned, not be explained by linear theory as it mirrors the end-products of highly nonlinear interactions.

It should be noted that the close agreement with

the Eady growthrate in Smith (2007) and miximum growth, was only stated for the filtered growth rates. The unfiltered rates were found to be much larger than the Eady estimate in areas where surface instabilities are prevailent. We recall from figure 3.4 that the growthrates exceeded ω_{eady} at several locations, e.g in the Lofoten and Canada Basin. L_i was also depicted smaller there (figure 3.5) We calculated the baroclinic energy conversion rate for the most unstable modes selected in our analysis, however we did not employ this as a filter. The reason behind this was partly due to the lack of a sound physical basis for choosing an upper treshold that should segregate the waves contributing to a significant energy conversion and those who do not. Smith (2007) set the limit based on GGS's estimates of the mean energy-input into the ocean by winds. This limit did not show to be apt in our analysis, and these caluculations were left out. Subsequently, as noted by Smith (2007), the unfiltered growthrates we find may also correspond to surface intensified modes several places. As an improvement of our analysis, an element that would be beneficial to add, but needs to be considered in more detail, is a sound technique for selecting more significant instabilities.

The most unstable lengthscale attained in our study, is smaller than the Rossby deformation radius at most locations. This is in crontrast to the zonal averages presented by Vollmer (2013) and Tulloch et al. (2011). On the other hand, we do see the same tendency of scales larger than L_d occuring in the energetic frontal zones next to Iceland and the boundary currents in the Nordic seas, the inflowing NAC branches, and the Barents Sea. In these areas, $L/L_d \approx 2$, as one expect from Eady theory. It is hard to be conclusive about the growthrates in this matter, as they occur both comparable and substatially smaller in some of these areas. However, we recall that the dynamics did not seem to be represented by an Eady instablility. The last case considered in 3.5.4 represent better several of the locations we examined that had a bottom slope. Surface intensified features was also exhibited frequently, and less so bottom-intensified flow. However, the bottom-intensified flows did appear more often than expected, which can be an interesting aspect to look further into at another occasion. Notably, we looked mostly at areas where the topography was sloping, but we recomputed every point also with a flat bottom. Excluding the bottom slope, commonly resulted in shifting the growth to slightly scales. The vertical structure wasMoreover, this also typically increased the growthrates, at some occassions 2-5 times overestimated by the flat bottom. The differences arising whenever flat-bottom slopes were invoked, thus imply that the assumption of Eady dynamics may tend produce larger scaled, more intense growth than what the fuller analysis gives.

Final remarks and outlook 1) We found that when linear predictions and products of a fully trubulent field are set side by side, there are, not surprisingly, differences present. Our findings reflect what has been observed in the others studies attempting to make similar comparisons. Namely, that this is not a trivial purcuit. As noted by Smith (2007), the most severe differences are especially observed in lengthscale of the perturbatons compared. Levels of growthrates are found more ammendable. As many climate model parameterizations of eddy transport depend on an Eady growthrate, as well as a characteristic lengthscale. A concern is here if the parameterizations are not representing the dynamics correctly, and that both growth and lengthscales might often be overestimated.

2) Despite discrepancies we found in the details of this issue, and the difficulties present in such juxtapositions, the broader picture is clearer. We recall the resemblance in the spatial patterns in the maps(figure) over baroclinic energy conversion. This gives leverage to the claim of baroclinic instability as a dominating generation mechanism, and we go as far as to say that it indeed can be regarded as that.

3) The eddy census have yielded estimates of key eddy characteristic, which was broadly found consistent with observational data. The commencement of further such studies is needed to verify these findings.

There are some intriguing questions that we have

not focused on in this study, but which are highly relevant. The most striking gap between eddy observations and modelled eddies at an 'eddy-permittable' resolution is perhaps the eddy counts in the high Arctic Ocean. With the search-criteria utilized here, we were not able to catch much of the 'action' that has been observed there. The 'eddy-void' in the Artic Ocean has also been implied in another eddy census study. Petersen et al. (2013) conducted a three-dimensional automated eddy census. They employed a global model simulation, which includes the Arctic Ocean. The model has a varying resolution of (10km at low latitudes, down to 3km in polar regions. Their census also show low eddy activity in the central and eastern Arctic Ocean. They suggested these low eddy counts could arise from a combination of factors, such as inadequate model-resolution and difficulties in producing a correct stratification. We also think that our model is also subject to these limitations. Eddies in the Arctic typically have a small lengthscale. Observations have indicated that numerous of eddies commonly have a diameter of 10km (Timmermans et al.2008), and reside immediately beneath the halocline. This scale is too small for our model to resolve, and we do not expect to find eddies of this type here. It would be interesting to investigate what causes this gap, and to perform an eddy census in the idpolar regions at a even higher model resolution. Another looming question is associated with the vertical extent of the eddies. Most of the eddy detection algorithms handle 2 dimensional fields, and we are left with some guesswork as to what structures the eddies possess in the vertical. Timmermans et al. (2010) have indicated the existence of deeper larger eddies in the Arctic, residing in the AW layer. The most eddies observed in the Arctic have been located about the shallow halocline depth. Why are we not catcing these? One might wonder, if there are eddies lurking beneath far beneath the surface that do no not leave a signal at the surface. Petersen et al. (2013), find that 97 % of their detected eddies of lifetimes longer than one month, extended all the way to the surface. Still, further investigations are need.

Bibliography

Anderson, E., Z. Bai, C. Bischof, J. Demmel, J. Dongarra, J. Du Croz, A. Greenbaum, S. Hammarling, A. McKenney, S. Ostrouchov, and D. Sorensen (1992). *LAPACK's User's Guide*. Philadelphia, PA, USA: Society for Industrial and Applied Mathematics.

Arakawa.A, L. (1977). Methods of computational physics. *Academic pres. 17*, 174–265.

Barton, E. (1997). Oceanography: An illustrated guide.

Beszczynska-Moller, A., E. Fahrbach, U. Schauer, and E. Hansen (2012). Variability in atlantic water temperature and transport at the entrance to the arctic ocean, 1997â2010. *ICES Journal of Marine Science: Journal du Conseil*.

Bretherton, F. P. (1966). Critical layer instability in baroclinic flows. *Quarterly Journal of the Royal Meteorological Society 92*(393), 325–334.

Charney, J. G. (1947, October). The Dynamics of Long Waves in a Baroclinic Westerly Current. *Journal of Atmospheric Sciences 4*, 136–162.

Chelton, D. B., R. A. DeSzoeke, M. G. Schlax, K. El Naggar, and N. Siwertz (1998). Geographical variability of the first-baroclinic Rossby radius of deformation. *J. ˜Phys. ˜Oceanogr. 28*, 433–460.

Chelton, D. B., M. G. Schlax, and R. M. Samelson (2011). Global observations of nonlinear mesoscale eddies. *Progress in Oceanography 91*(2), 167 – 216.

Chelton, D. B., M. G. Schlax, R. M. Samelson, and R. A. de Szoeke (2007). Global observations of large oceanic eddies. *Geophysical Research Letters 34*(15), n/a–n/a. L15606.

Crease, J. (1962). Velocity measurements in the deep water of the western North Atlantic. *J. Geophys. Res. 67*, 3173–3175.

Cuny, J., P. B. Rhines, P. P. Niiler, and S. Bacon (2002). Labrador Sea Boundary Currents and the Fate of the Irminger Sea Water. *Journal of Physical Oceanography 32*(2), 627–647.

D'Asaro, E. A. (1988). Observations of small eddies in the Beaufort Sea.

Eady, E. T. (1949). Long waves and cyclone waves. *Tellus 1*(3), 33–52.

Femke de Jong,Furey, Heather H., M. Valdes, James R.Bower, A. S. (2013). Eddy Seeding in the Labrador Sea: A Submerged Autonomous Launch Platform Application. *Journal of Atmospheric and Oceanic Technology 30*(11), 2611–2629.

Flierl, G. R. and J. Pedlosky (2007). The nonlinear dynamics of time-dependent subcritical baroclinic currents. *J. Phys. Oceanogr. 37*, 1001–1020.

Gent, P. R., J. Willebrand, T. J. McDougall, and J. C. McWilliams (1995). Parameterizing Eddy-Induced Tracer Transports in Ocean Circulation Models.

Gill, A. E., J. S. A. Green, and A. J. Simmons (1974). Energy partition in the large-scale ocean circulation and the production of mid-ocean eddies. *21*(7), 499–528.

Griffies, S. M. (2004). Fundamentals of ocean climate models. *pup.princeton.edu*.

Haidvogel, D. B. and A. Beckmann (1999). *Numerical ocean circulation modeling*, Volume Series on. Imperial College Press.

Halo, I., B. Backeberg, P. Penven, I. Ansorge, C. Reason, and J. Ullgren (2014). Eddy properties in the mozambique channel: A comparison between observations and two numerical ocean circulation models. *Deep Sea Research Part II: Topical Studies in Oceanography 100*(0), 38 – 53. The Mozambique Channel: Mesoscale Dynamics and Ecosystem Responses.

Hansen, B. and J. Meincke (1979). Eddies and meanders in the Iceland-Faroe Ridge area.

Held, I. M. and V. D. Larichev (1996). A scaling theory for horizontally homogeneous, baroclinically unstable flow on a beta plane. *J. Atmos. Sci*, 946–952.

Holton, J. R. (1973). An Introduction to Dynamic Meteorology.

Horn, D. (1987). Winter MIZEX 87, Operations Overview. pp. 76,77,78,79,80,81,82.

Ikeda, M., J. a. Johannessen, K. Lygre, and S. Sandven (1989). A Process Study of Mesoscale Meanders and Eddies in the Norwegian Coastal Current.

Isachsen, P. E. (2015). Baroclinic instability and the mesoscale eddy field around the lofoten basin. *Journal of Geophysical Research: Oceans 120*(4), 2884–2903.

Isachsen, P. l. E. (2011). Baroclinic instability and eddy tracer transport across sloping bottom topography: How well does a modified Eady model do in primitive equation simulations? *Ocean Modelling 39*(1-2), 183–199.

Isachsen, P. l. E., C. Mauritzen, and H. Svendsen (2007). Dense water formation in the Nordic Seas diagnosed from sea surface buoyancy fluxes. *Deep-Sea Research Part I: Oceanographic Research Papers 54*(1), 22–41.

J. Isern-Fontanet, E. GarcÃa-Ladona, J. F. (2003). Identification of marine eddies from altimetric maps. *20*, 772–778.

Johannessen, O. M., J. A. Johannessen, E. Svendsen, R. A. Shuchman, W. J. Campbell, and E. Josberger (1987). Ice-edge eddies in the fram strait marginal ice zone. *Science (New York, N.Y.) 236*(4800), 427–429.

Koszalka, I., A. Bracco, J. C. McWilliams, and A. Provenzale (2009). Dynamics of wind-forced coherent anticyclones in the open ocean. *Journal of Geophysical Research: Oceans 114*(C8), n/a–n/a. C08011.

Lavender, K. L. (2000). Mid-depth recirculation observed in the interior Labrador and Irminger seas by direct velocity measurements. *Nature*.

Le Traon, P. Y. (2013). From satellite altimetry to Argo and operational oceanography: Three revolutions in oceanography. *Ocean Science 9*(5), 901–915.

Le Traon, P.-Y. and J.-F. Minster (1993). Sea level variability and semiannual rossby waves in the south atlantic subtropical gyre. *Journal of Geophysical Research: Oceans 98*(C7), 12315–12326.

Le Traon, P. Y., M. C. Rouquet, and C. Boissier (1990). Spatial scales of mesoscale variability in the north atlantic as deduced from geosat data. *Journal of Geophysical Research: Oceans 95*(C11), 20267–20285.

LeBlond, P. and L. Mysak (1978). Waves in the ocean, 602 pp.

Lilly, J. M., P. B. Rhines, F. Schott, K. Lavender, J. Lazier, U. Send, and E. DAsaro (2003). Observations of the Labrador Sea eddy field. *Progress in Oceanography 59*(1), 75–176.

Manley, T. O. and K. Hunkins (1985). Mesoscale eddies of the Arctic Ocean.

Marshall, J. and F. Schott (1999). Open-ocean convection: Observations, theory, and models. *Reviews of Geophysics 37*(1), 1–64.

Maslowski, W., J. C. Kinney, D. C. Marble, and J. Jakacki (2008). Towards eddy-resolving models of the arctic ocean. *Geophysical Monograph Series 177*, 350.

Mauritzen, C. (2012). Oceanography: Arctic freshwater.

McCartney, M. S. and C. Mauritzen (2001). On the origin of the warm inflow to the Nordic Seas.

Mcwilliams, J. C. (1990). The vortices of two-dimensional turbulence.

Mcwilliams, J. C. (2008). The Nature and Consequences of Oceanic Eddies. In *Ocean Modeling in an Eddying Regime*, pp. 5–15.

Nencioli, F., G. Chang, M. Twardowski, and T. D. Dickey (2010). Optical Characterization of an Eddy-induced Diatom Bloom West of the Island of Hawaii. *Biogeosciences 7*(1), 151–162.

Newton, J., K. Aagaard, and L. Coachman (1974). Baroclinic eddies in the Arctic Ocean.

Nø st, O. A. and P. l. E. Isachsen (2003). The large-scale time-mean ocean circulation in the Nordic Seas and Arctic Ocean estimated from simplified dynamics.

Nurser, a. J. G. and S. Bacon (2013). Eddy length scales and the Rossby radius in the Arctic Ocean. *Ocean Science Discussions 10*(5), 1807–1831.

Okubo, A. (1970). Horizontal dispersion of floatable particles in the vincinity of velocity singularities such as convergences. *Deep Sea Research 17*, 445–454.

Orvik, K. A., Ø. Skagseth, and M. Mork (2001). Atlantic inflow to the nordic seas: current structure and volume fluxes from moored current meters, vm-adcp and seasoar-ctd observations, 1995–1999. *Deep Sea Research Part I: Oceanographic Research Papers 48*(4), 937–957.

Pedlosky, J. (1964). The Stability of Currents in the Atmosphere and the Ocean: Part II.

Pedlosky, J. (1982). *Geophysical Fluid Dynamics*. New York: Springer-Verlag.

Pedlosky, J. (1987). *Geophysical Fluid Dynamics* (2nd ed.). New York: Springer-Verlag.

Penven, P., V. Echevin, J. Pasapera, F. Colas, and J. Tam (2005). Average circulation, seasonal cycle, and mesoscale dynamics of the Peru Current System: A modeling approach. *Journal of Geophysical Research C: Oceans 110*(10), 1–21.

Petersen, M. R., S. J. Williams, M. E. Maltrud, M. W. Hecht, and B. Hamann (2013). A three-dimensional eddy census of a high-resolution global ocean simulation. *Journal of Geophysical Research: Oceans 118*(4), 1759–1774.

PHILLIPS, N. A. (1954). Energy transformations and meridional circulations associated with simple baroclinic waves in a two-level, quasi-geostrophic model1. *Tellus 6*(3), 273–286.

Poulain, P.-M., A. Warn-Varnas, and P. P. Niiler (1996). Near-surface circulation of the nordic seas as measured by lagrangian drifters. *Journal of Geophysical Research: Oceans 101*(C8), 18237–18258.

Prater, M. D. (2002). Eddies in the Labrador Sea as Observed by Profiling RAFOS Floats and Remote Sensing. *Journal of Physical Oceanography 32*(2), 411–427.

Raj, R. P., L. Chafik, J. E. Ø. Nilsen, T. Eldevik, and I. Halo (2015, February). The Lofoten Vortex of the Nordic Seas. *Deep Sea Research Part I: Oceanographic Research 96*, 1–14.

Rø ed, L. P. (2014). Fundamentals of Atmospheres and Oceans on Computers. *Unpublished lecture notes (compendium)*.

Robinson, A. R., M. A. Spall, and N. Pinardi (1988). Gulf Stream simulations and the dynamics of ring and meander processes. *J.˜Phys.˜Oceanogr. 18*, 1811–1853.

Scott, R. B. and F. Wang (2005). Direct evidence of an oceanic inverse kinetic energy cascade from satellite altimetry. *J. Phys. Oceanogr. 35*, 1650–1666.

Seidov, D., J. I. Antonov, K. M. Arzayus, O. K. Baranova, M. Biddle, T. P. Boyer, D. R. Johnson, A. V. Mishonov, C. Paver, and M. M. Zweng (2014). Oceanography north of 60N from World Ocean Database.

Shchepetkin, A. F. and J. C. McWilliams (2005). The regional oceanic modeling system ({ROMS}): a split-explicit, free-surface, topography-following-coordinate oceanic model. *Ocean˜Model. 9*, 347–404.

Shi, Xiao Bing, Røed, L. P. (1999). Frontal Instabilities in a Two-Layer, Primitive Equation Ocean Model. *Journal of Physical Oceanography 29*(5), 948–968.

Smith, K. S. (2007). Eddy amplitude in baroclinic turbulence driven by nonzonal mean flow: shear dispersion of potential vorticity. *J. Phys. Oceanogr. 37*, 1037–1050.

Sø iland, H. and T. Rossby (2013). On the structure of the lofoten basin eddy. *Journal of Geophysical Research: Oceans 118*(9), 4201–4212.

Spall, M. A., R. S. Pickart, P. S. Fratantoni, and A. J. Plueddemann (2008). Western Arctic Shelfbreak Eddies: Formation and Transport.

Stammer, D., C. Wunsch, R. Giering, C. Eckert, P. Heimbach, J. Marotzke, A. Adcroft, C. N. Hill, and J. Marshall (2002). Global ocean circulation during 1992â1997, estimated from ocean observations and a general circulation model. *Journal of Geophysical Research: Oceans 107*(C9), 1–1–1–27. 3118.

Thompson, A. and S. D. University of California (2006). *Eddy Fluxes in Baroclinic Turbulence*. University of California, San Diego.

Thomsen, Soren. Eden, C. (2014). Stability Analysis of the Labrador Current. *Journal of Physical Oceanography 44*(2), 445–463.

Thorpe, S. (2005). *The Turbulent Ocean*. Cambridge University Press.

Timmermans, M. L.

Timmermans, M.-L., L. Rainville, L. Thomas, and a. Proshutinsky (2010). Moored observations of bottom-intensified motions in the deep Canada Basin, Arctic Ocean. *Journal of Marine Research 68*(3), 625–641.

Tulloch, R. (2009). *PHD thesis: Geostrophic dynamics at surfaces in the atmosphere and ocean*. Ph. D. thesis.

Tulloch, R., J. Marshall, C. Hill, and K. S. Smith (2011). Scales, Growth Rates, and Spectral Fluxes of Baroclinic Instability in the Ocean.

Tulloch, R., J. Marshall, and K. S. Smith (2009). Interpretation of the propagation of surface altimetric observations in terms of planetary waves and geostrophic turbulence. *Journal of Geophysical Research: Oceans 114*(C2), n/a–n/a. C02005.

Vallis, G. K. (2006). *Atmospheric and oceanic fluid dynamics: fundamentals and large-scale circulation*.

Venaille, A., G. K. Vallis, and K. S. Smith (2011). Baroclinic Turbulence in the Ocean: Analysis with Primitive Equation and Quasigeostrophic Simulations.

Weiss, J. (1991, mar). The dynamics of enstrophy transfer in two-dimensional hydrodynamics. *Physica D Nonlinear Phenomena 48*, 273–294.

Woodgate, R. A., K. Aagaard, R. D. Muench, J. Gunn, G. Bjork, B. Rudels, A. T. Roach and U. Schauer (2001). The Arctic Ocean boundary current along the Eurasian slope and the adjacent Lomonosov Ridge: Water mass properties, transports and transformations from moored instruments. *Deep-Sea Res. 48*, 1757–1792.

Wright, D. G. (1987). Baroclinic instability: Energy transfer and the role of potential vorticity conservation. *Atmosphere-Ocean 25*(3), 225–241.

Wunsch, C. (1999). A Summary of North Atlantic Baroclinic Variability.

Wunsch, C. and D. Stammer (1997). Atmospheric loading and the oceanic 'inverted barometer' effect. *Reviews of Geophysics 35*(1), 79–107.

Zhao, M., M.-L. Timmermans, S. Cole, R. Krishfield, A. Proshutinsky, and J. Toole (2014). Characterizing the eddy field in the arctic ocean halocline. *Journal of Geophysical Research: Oceans 119*(12), 8800–8817.